Autogenous and Drying Shrinkage of Wood Biomass Fly Ash and Municipal Solid Waste Incineration Bottom Ash Blended Cement Paste

By

Liangzhi Sun

TU Delft

Autogenous and Drying Shrinkage of Wood Biomass Fly Ash and Municipal Solid Waste Incineration Bottom Ash Blended Cement Paste

Liangzhi Sun

5917271

Instructor: Professor Guang Ye & Dr. Boyu Chen
Project Duration: February 2025 - December 2025
Faculty: Civil Engineering and Geosciences, Delft

TU Delft

Acknowledgements

As I am writing these lines, my master's journey is quietly coming to an end. It feels both unreal and very special to look back at the past two and a half years, and I would like to take this chance to say thank you to the many people who have walked this road with me.

First of all, I would like to thank my committee. I am very grateful to Prof. Guang Ye for his guidance and support. His comments were always to the point and helped me to see the bigger picture when I was lost in details. Many times, his suggestions made my thoughts more structured and clear, and gave me confidence that I was still moving in the right direction.

My heartfelt thanks go to my daily supervisor, Dr. Boyu Chen. She has been closely involved in every step of my work, from the design of the experiments to the interpretation of the results. Under her guidance I improved a lot, not only in technical skills but also in how I think, write and present as a young researcher. For me, she is not only a supervisor but also a friend. Her kindness, patience and encouragement have left a very deep and warm memory in my master's life. I would also like to thank Dr. Abraham Gebremariam for his sharp and thoughtful questions, which often forced me to think more deeply and to explain my ideas more clearly.

I am also very thankful to the Microlab technicians and staff — John, Maiko, Ton, Arjan and Paul. Without their help with casting, testing and all kinds of practical issues in the lab, I would not have been able to obtain reliable data and complete this thesis. I especially want to thank Yu Zeng for his help during the summer. At a time when the schedule was very tight, his support made it possible for me to keep the experiments on track.

As a member of the CMMB group, I feel very honoured and lucky. Being part of this group has meant much more than just having a place to sit and do experiments. It has given me a community to grow in: inspiring discussions during group meetings, casual conversations over coffee, and the quiet support of knowing that everyone around me is also trying to push a little bit further in their own research. The atmosphere in CMMB has taught me what it means to do science seriously, while still caring for the people behind the work.

These two and a half years in Delft would not have been the same without my friends: Zhihui Fang, Pengran Lu, Hang Gao, Jun Lin, Chen Liang, Luyuan Long, Joris, Rajat, Yanchen He, Nuoyao Feng, Raoul, Brie, Mike and Lars. Thank you for the coffee breaks, late-night talks, shared stress before deadlines, and all the laughter and small moments in between. Because of you, this period of my life has been colourful, exciting and truly unforgettable.

Finally, I want to say thank you from the bottom of my heart to my parents. Thank you for your endless care, support and understanding, even when I was far away from home. Without your trust and all the dedication you made for me, I would never have had the chance to experience this chapter of my life. As my master's study comes to a close, I know that the memories, lessons and support from these years will continue to accompany me and give me strength on the many roads ahead.

Looking back, I still remember the nights when I felt stuck in experiments, confused by results or worried about the future. Somehow, with the help of all the people mentioned above, each of those moments turned into a step forward. This thesis may only mark the end of my time as a master's student, but it also feels like the starting point of a new journey. No matter where I go next, a part of me will always stay here — in the lab, in the lecture halls, and in the ordinary days in Delft that have quietly shaped who I am today.

Liangzhi Sun

Den Haag, November 2025

Summary

This thesis investigates the autogenous and drying shrinkage of cement pastes incorporating wood biomass fly ash (BFA) and municipal solid waste incineration bottom ash (MSWI BA) as supplementary cementitious materials. Nine paste mixtures were produced at a water-to-binder ratio = 0.35, with total ash replacement levels between 0 and 30 wt% and different BFA–MSWI BA combinations. The experimental programme comprised tests on fresh properties (workability and setting time) to ensure comparable casting conditions, mechanical properties (compressive and flexural strength, elastic modulus) to place the deformation in the context of load-bearing performance, and direct measurements of autogenous shrinkage under sealed conditions up to 7 days and drying shrinkage after 28 days of curing as the main indicators of volume stability. Microstructural characterization at selected ages was carried out in parallel to support the interpretation of the observed shrinkage behavior.

On this basis, the key results on workability, setting time, mechanical properties and shrinkage behavior are summarized in the following paragraphs.

Replacing cement with BFA or MSWI BA reduced slump and flowability in all mixtures. At the same total replacement level, mixtures containing only BFA show larger losses of workability than mixtures with only MSWI BA. Both ashes extended initial and final setting times, and the extension increased with replacement level. For equal total ash content, BFA blended mixes generally exhibited longer setting times than MSWI BA blended mixes. Compressive and flexural strength decreased with increasing BFA and MSWI BA content at all tested ages, and the elastic modulus followed the same trend.

For autogenous shrinkage over the first 7 days, all mixtures displayed a sequence of an initial deformation stage, a swelling peak and a subsequent shrinkage phase. The final 7-day autogenous shrinkage increased with total ash content and depended on ash type—BFA blended mixtures showed larger autogenous shrinkage (130%-171% of CEM I paste's autogenous shrinkage), MSWI BA blended mixtures showed smaller autogenous shrinkage (10%-33% of CEM I paste's autogenous shrinkage). The paste with 20% MSWI BA and 10% BFA (30% total replacement level) shows the highest 7-day autogenous shrinkage. Combining BFA with MSWI BA does not reduce autogenous shrinkage; shrinkage increases with BFA dosage, and the lowest 7-day autogenous shrinkage is obtained for mixtures containing only MSWI BA (20% MSWI BA).

For drying shrinkage after 28 days of curing, all ash-bearing mixtures showed higher shrinkage than the reference. Drying shrinkage increased with the total ash replacement level. Among the mixtures with the same total replacement, BFA blended pastes generally exhibited higher drying shrinkage, while MSWI BA blended pastes showed smaller increases compared to cement paste. Mixtures with same BFA dosage blended with MSWI BA could lower drying shrinkage values from 21% to 33%, indicating that the presence of MSWI BA mitigated the drying shrinkage observed in BFA blended systems.

Within the research scope, mixtures with more MSWI BA and less BFA achieved lower autogenous and drying shrinkage than CEM I paste.

Contents

1.Introduction

1.1.Motivation

As the seeking for sustainable alternatives to reduce the environmental impact of cement production developing, industrial by-products and waste ashes have gained attention as supplementary cementitious materials (SCMs)[1]. Among them, Biomass Fly Ash (BFA) and Municipal Solid Waste Incineration Bottom Ash (MSWI BA) are two promising candidates due to their abundance and potential reactivity. MSWI BA is defined as the mineral-rich residue discharged from the grate at the end of municipal solid waste combustion, typically comprising 80–85% mineral fraction with recoverable metals[2], [3]. The biomass fly ash (BFA) considered in this study refers to the fine particulate ash collected from wood-biomass combustion flue gas[4]. In terms of availability, Europe alone generates ~19 $Mt \cdot yr^{-1}$ of MSWI bottom ash (2018 data) [2], while biomass-combustion ashes amount to several-tens to hundreds of $Mt \cdot yr^{-1}$ globally, with European BFA ≈ 5.5 Mt in 2020[4]. For context, conventional SCM streams are of similar or larger order of magnitude—coal fly ash ≥ 300 $Mt \cdot yr^{-1}$ (≈2020) [5] and blast-furnace slag ~330–375 $Mt \cdot yr^{-1}$[6], [7]—underscoring that MSWI BA and wood-BFA are sufficiently available to merit valorization as SCMs. Leveraging these ashes aligns with circular-economy strategies by diverting residues from landfill, recovering metals, and reducing demand for clinker-intensive binders[8].” Their use supports circular economy strategies and reduces dependency on traditional clinker-based systems.

To put MSWI BA and BFA in the practical SCM landscape introduced above, it is useful to contrast them with the conventional SCMs that have historically dominated practice.Traditionally, coal fly ash (CFA) and ground granulate blast furnace slag (GGBS) became prevalent because they combine wide availability, established performance, and clear standards (EN 450-1 for fly ash; EN 15167 for GGBS; ASTM C618 and ASTM C989 in the U.S.)[9], [10], [11]. GGBS exhibits high reactivity, allowing it to form a dense and durable geopolymer matrix with relatively mild activation conditions. CFA, while generally exhibiting lower reactivity, is still highly valued due to its ability to reduce heat of hydration and enhance long-term strength development when used in alkali-activated systems[12], [13]. Additionally, CFA and GGBS have been extensively studied and standardized for use in concrete, leading to their widespread adoption in both research and practical applications. However, with the ongoing phase-out of coal-fired power plants and the steel industry’s transition to low-carbon production, the availability of these materials is expected to decline over the next few decades[14], [15], [16]. This has driven research into alternative precursors, such as BFA and MSWI BA, which offer significant sustainability advantages by repurposing industrial by-products and reducing reliance on conventional raw materials[17].

CFA and GGBS have been successfully incorporated into binder systems over the past few decades. CFA has been extensively used in both alkali-activated binders and Ordinary Portland Cement (OPC) concrete[18], primarily as a partial cement replacement to enhance long-term strength and workability. GGBS, known for its high reactivity, has been particularly effective in alkali-activated concrete, where it promotes early strength development and improves durability[19]. In contrast, MSWI BA and BFA have not yet been widely adopted in cement applications due to their variable composition and lower reactivity compared to FA and GGBS[17], [20], [21]. But this problem can be solved by preprocessing, such as grinding or calcination, to enhance their contribution to strength development[22]. Therefore, the use of BFA and MSWI BA as alternatives is promising.

However, one of the key concerns with valorising these ashes is their influence on the volume stability of cement-based materials. In particular, shrinkage-related deformations—autogenous shrinkage driven by self-desiccation and capillary stresses, and drying shrinkage governed by capillary tension and disjoining pressures—are central to early cracking risk and long-term durability[23], [24]. The incorporation of BFA can modify hydration kinetics and pore structure and thereby alter autogenous and drying shrinkage responses[25], [26]. For MSWI BA, studies have reported volume changes in cementitious systems (e.g., gas-evolution-related swelling at early age) and increased drying shrinkage when used to replace conventional aggregates or powders, highlighting the need to control mixture design and curing [27], [28]. These deformation can translate into cracking and durability issues in practice, making a deeper, mechanism-based understanding of how BFA and MSWI BA affect shrinkage at both macro and micro levels, which are essential for safe and sustainable implementation.

1.2.Research gaps

Despite the promising sustainability benefits of using BFA and MSWI BA as SCMs, one of the most critical challenges is their influence on the volume stability of cement-based materials. Volume changes such as autogenous shrinkage and drying shrinkage are closely linked to early-age cracking and durability. The incorporation of ashes can alter hydration kinetics and pore structure, thereby modifying these shrinkage responses[29]. However, for BFA and MSWI BA, the mechanisms and boundary conditions remain insufficiently resolved for robust implementation.

Currently, limited studies have systematically compared BFA and MSWI BA side-by-side with respect to both autogenous and drying shrinkage. Existing reviews and experimental reports tend to emphasize strength, permeability, or leaching behavior, while shrinkage mechanisms are treated only briefly or indirectly [28], [30]. Important knowledge gaps include how ash incorporation affects pore refinement, reaction kinetics, and potential internal-curing, and how these translate to macroscopic deformation.

Furthermore, without sufficient control over shrinkage behaviours, the practical application of BFA and MSWI BA as sustainable alternatives may be

compromised, diminishing their environmental benefits due to potential service-life reduction and repair needs.

1.3.Research questions

Previous studies have shown that supplementary cementitious materials can significantly influence the volume stability of cement-based materials. However, the specific effects of BFA and MSWI BA on autogenous and drying shrinkage, as well as the underlying mechanisms, are still not fully understood. Based on this knowledge gap, the present work is guided by the following main research question:

Main research question

“How does the partial replacement of Portland cement by BFA and MSWI BA affect the autogenous and drying shrinkage of cement paste, and how can this understanding be used to design mixtures with reduced shrinkage?”

To address this main question, three sub-questions are formulated:

1. **Phenomenon – macroscopic behaviour**
   What is the impact of adding BFA and MSWI BA on cement paste’s performance?
2. **Reason – underlying mechanisms**
   How do ashes influence the Autogenous and Drying shrinkage?
3. **Application – mix-design implications**
   How to guide mix design to minimize Autogenous and Drying shrinkage?

1.4.Research goals

The primary goal of this research is to provide mix design guidance to improve volume stability in BFA and/or MSWI BA blended cement., with a particular focus on autogenous shrinkage and drying shrinkage. This study aims to identify the underlying mechanisms responsible for shrinkage behaviours and propose effective strategies to mitigate negative effects, thereby enabling the safe and durable use of these waste ashes as supplementary cementitious materials.

To achieve this goal, the following specific objectives are defined:

1. To evaluate the effects of BFA and MSWI BA on cement paste’s fresh, mechanical, autogenous and drying shrinkage performance.

2. To identify and analyze the mechanisms responsible for autogenous and drying shrinkage

3. To establish guidance in using BFA and MSWI BA on maintaining lower autogenous and drying shrinkage as sustainable SCM

1.5.Research scope

This research focuses on evaluating the volume stability of cement-based materials incorporating BFA and MSWI BA as partial replacements for cement. The study is divided into two main stages and is limited to laboratory-scale investigations.

The scope of the study is outlined as follows:

1. Two types of waste ashes are studied: (i) wood-biomass fly ash (BFA) and (ii) municipal solid-waste incineration bottom ash (MSWI BA), both from defined sources used in this study. No other SCMs are included, to isolate the effects of BFA and MSWI BA. Because MSWI BA and BFA exhibit substantial compositional and mineralogical variability across plants and processing routes, results here reflect these specific materials; transfer to other contexts should be preceded by local material characterization and, if needed, mix-specific calibration.

2. Both autogenous shrinkage and drying shrinkage are measured on paste specimens. No restrained shrinkage or creep-related deformation is considered. or durability aspects (e.g., carbonation, chloride penetration) are outside the scope of this work.

3. All tests are conducted at laboratory scale under controlled curing conditions (20°, 95% RH). The study focuses on early-age and 28-day to 60-day measurements. Long-term behavior is not covered.

1.6.Thesis outline

The thesis outline for this research is depicted in Figure 1.1. The outline entails a brief description of the chapter content.

Chapter 1 – Introduction
This chapter introduces the background and motivation of the study, defines the problem and research gap, outlines the research objectives and scope, and presents the structure of the thesis.

Chapter 2 – Literature Review
A comprehensive review of existing research on BFA and MSWI BA is provided, with a focus on their chemical and physical properties, shrinkage behavior, and their potential roles in autogenous and drying shrinkage. Existing knowledge on autogenous and drying shrinkage mechanisms is also discussed.

Chapter 3 – Materials and Experimental Methods
This chapter introduces the materials used in this study, including their physical, chemical, and mineralogical properties. It also presents the experimental set up applied to assess the fresh properties, mechanical performance, shrinkage behavior, and microstructural characteristics of the cement-based systems.

Finally, the methodological framework of the study is outlined, including how the experiments are structured to address the research questions and objectives.

Chapter 4 – Fresh and Mechanical Properties
This chapter presents the fresh and mechanical properties of cement-based systems incorporating BFA and MSWI BA as SCMs. The results are discussed in terms of 6 key aspects: slump, flowability, setting time, compressive strength, flexural strength, e-modulus. Together, these findings provide an overall assessment of how SCM incorporation affects performance at the macroscale.

Chapter 5 – Autogenous Shrinkage.
This chapter examines the early-age deformation of sealed pastes where autogenous shrinkage dominates. Comparing a reference with different mix, track deformation from final setting to 7 days. The chapter concludes with how and why MSWI BA and BFA can affect early-age deformation.

Chapter 6 – Drying Shrinkage.
This chapter reports drying-shrinkage as the volume change of pastes measured during exposure after 28-day curing. It compares the reference mix with MSWI BA and BFA blended pastes and explains the differences using pore-structure analysis.

Chapter 7 – Conclusions and Recommendations
The final chapter summarizes the main findings, addresses the research questions, and provides recommendations for further research. The feasibility of using BFA and MSWI BA in volume-stable and sustainable cement-based materials is discussed.

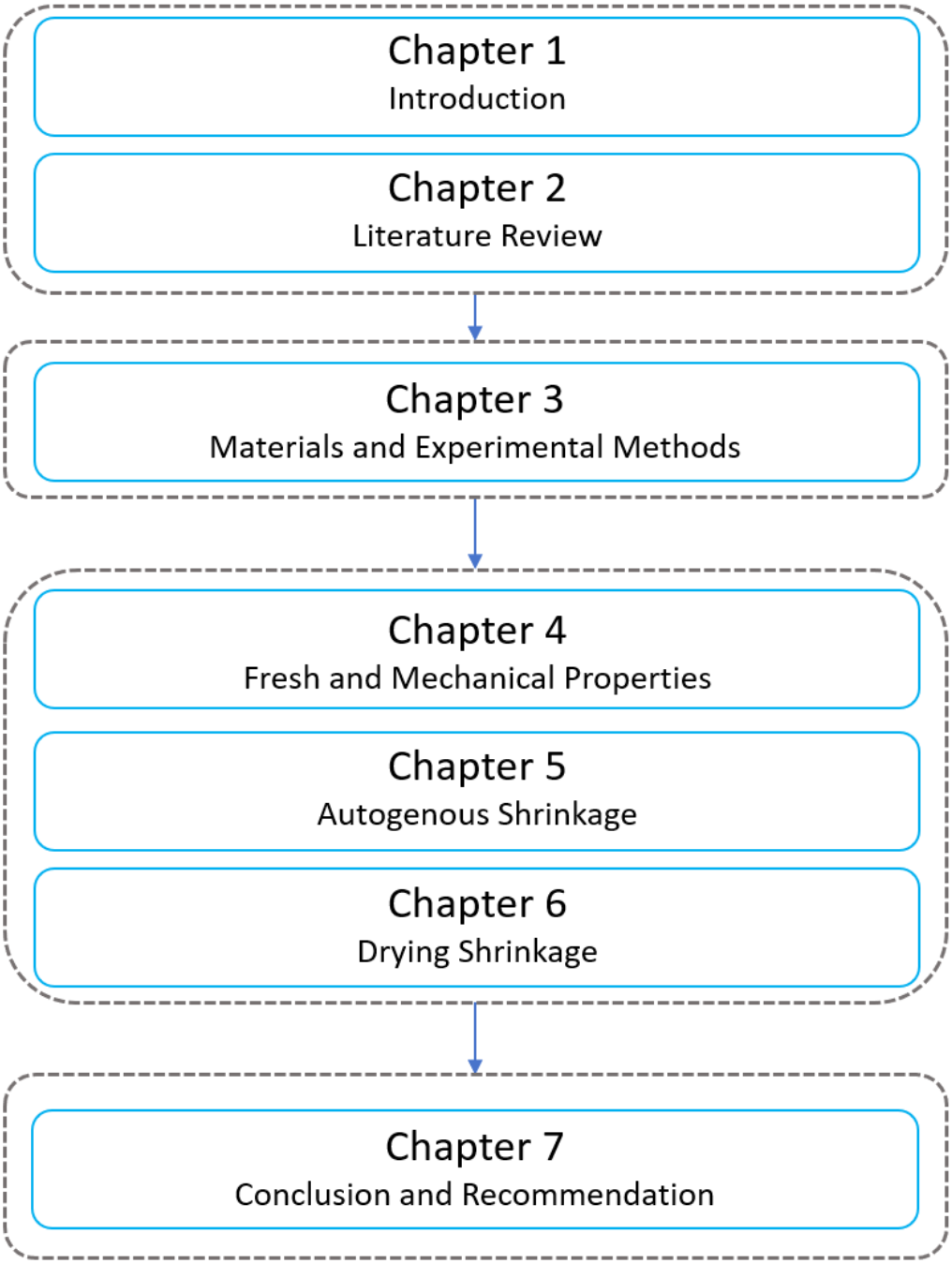

Figure 1.1 Thesis outline

2. Literature Review

2.1.Utilization of BFA and MSWI BA

BFA, particularly derived from agricultural and wood-based residues, has gained increasing attention as a promising SCM due to its potential for carbon footprint reduction and resource recovery. Owing to its high contents of reactive silica and alumina[31], [32], BFA has been explored for use in OPC replacement, geopolymer synthesis, and lightweight aggregate production [33], [34]. Recent studies have highlighted the considerable potential of BFA for broader applications in cementitious systems. Liang's work demonstrated that even at high replacement levels—up to 70% in binary pastes and 30% in GGBS-blended systems—wood-based BFA maintained satisfactory mechanical performance, with only marginal strength loss after 90 days[35]. Park et al. further showed that physical pretreatment of wood fly ash (WFA), including calcination and ball milling, significantly enhanced early-age reactivity by promoting hydration, reducing setting time, and improving strength[36]. Complementarily, Xu et al. investigated flotation as a method to improve the chemical and pozzolanic characteristics of BFA from diverse sources[37].

Several recent studies have reported on the technical performance and material characteristics of BFA in cementitious systems. In one study, WFA with a high CaO content was incorporated into concrete at 15% and 30% cement replacement levels. The 28-day compressive strength of concrete was reduced by up to 37%, while the 2-year strength remained low, indicating limited long-term pozzolanic reactivity[38]. Another study compared the mechanical performance of concrete containing different types of BFA, including co-fired biomass-coal ash, pure wood ash, and blended ash. At a 25% replacement ratio, compressive and flexural strengths of concrete with co-fired and blended BFA were reported to be statistically equivalent to those of coal fly ash concrete[39]. In terms of environmental performance, one investigation analyzed the leaching characteristics of wood biomass ash (WBA) in cement composites. Three WBA samples from different power plants were used to replace 15% of the cement, and leaching tests were conducted on monolithic and crushed samples. Elevated leaching values were detected in untreated WBA, whereas leaching was reduced after incorporation into the cement matrix[40].

2.2.Hydration process and formation of microstructure of cement paste

2.2.1.Hydration process of cement paste

The exothermic behavior of cement hydration provides valuable insights into the underlying chemical reactions occurring at various stages. By analyzing the rate of heat evolution, it becomes possible to identify the formation and transformation of hydration products that govern setting and early-age performance.

Figure 2.1 illustrates the typical heat evolution rate during the hydration of Portland cement under isothermal conditions, highlighting three distinct peaks corresponding to specific hydration reactions. The sharp initial peak corresponds to the wetting of cement particles and the rapid formation of ettringite (AFt) due to the reaction between tricalcium aluminate (C_3A) and sulfate[41], [42]. The first major peak, attributed to the hydration of tricalcium silicate (C_3S or alite), marks the acceleration period of hydration. This reaction forms calcium silicate hydrate (C-S-H) and calcium hydroxide (CH), contributing to early strength development[43]. A secondary peak is observed after the alite reaction, likely due to the delayed formation of ettringite[44]. This may result from continued sulfate availability and the sustained release of aluminates from clinkers or supplementary cementitious materials. At a later stage, a smaller heat evolution is associated with the conversion of ettringite into monosulfate (AFm), once sulfate is depleted[45], [46]. This reaction proceeds more slowly and represents the continued hydration of C_3A in a low-sulfate environment.

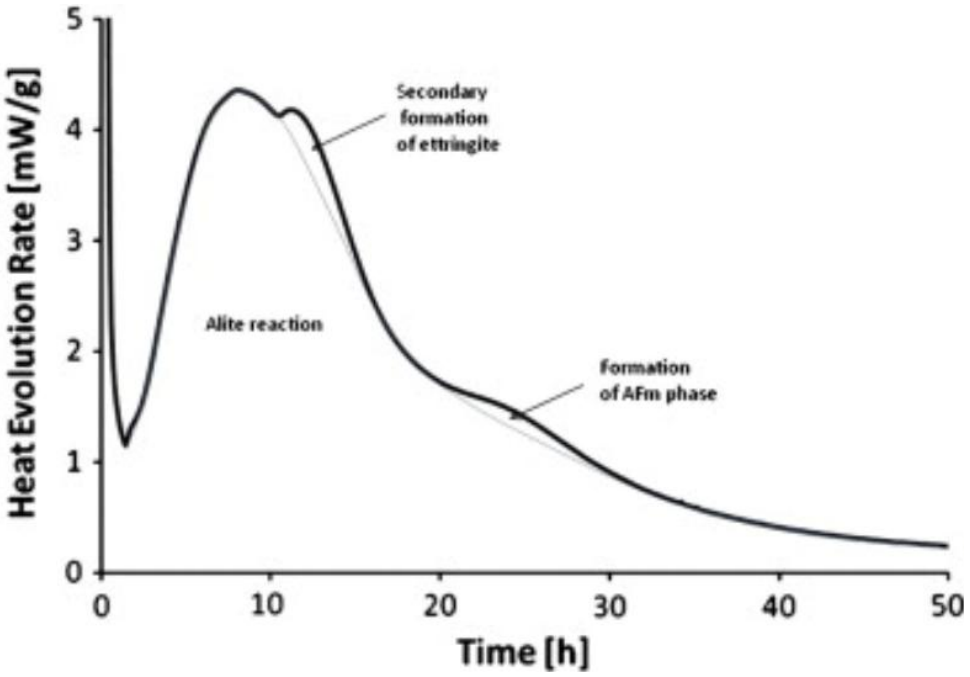

Figure 2.1. Calorimetry curve of ordinary Portland cement[42].

This sequence of thermal events not only reflects the chemical evolution of the system but also serves as a foundation for understanding how early-age hydration kinetics can be influenced by material composition, admixtures, or alternative binder systems.

2.2.2.Formation of microstructure of cement paste

The development of microstructure in hydrating Portland cement paste plays a critical role in determining its volume stability. As hydration progresses, the formation of hydration products leads to the progressive filling of pore space and the establishment of a rigid skeleton. Several researchers have noted that the pore structure evolves dynamically at early ages, with a reduction in total porosity and a shift towards finer pores[47]. This refinement enhances capillary stresses due to increased meniscus curvature in smaller pores, which

contributes to autogenous shrinkage[48]. Moreover, the pore connectivity and degree of saturation within the capillary network affect the magnitude and rate of internal water transport, further influencing the extent of deformation. Thus, pore structure not only reflects the degree of hydration but also governs early-age volume changes through its control on moisture movement and internal stresses.

A classification was made into capillary pores and gel pores as shown in Table 2.1.

Table 2.1: Classification of pores in hydrated cement paste[49].

Type of pores	Description	Diameter	Affected properties
Capillary pores	Large	50nm-10μm	Permeability, strength
	Medium	10nm-50nm	Permeability, strength, shrinkage
Gel pores	Small	2.5nm-10nm	Shrinkage
	Micro	0.5nm-2.5nm	Shrinkage, creep
Interlayer spaces	Structural	< 0.5nm	Shrinkage, creep

Figure 2.2. illustrates two-dimensional sections of C_3S particles before and after hydration under different boundary conditions. As shown, hydration leads to a denser matrix with increased formation of hydration products (C-S-H and CH), which progressively occupy the pore space and reduce the initial porosity. This structural transformation underlines the direct relationship between hydration progression and the reduction of free pore volume.

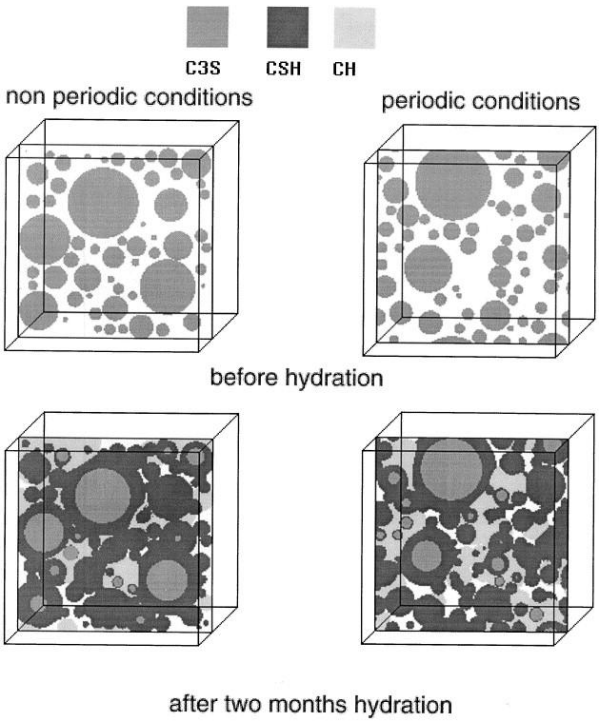

Figure 2.2 Two-dimensional section of hydrated C_3S particles situated 50 μm from the computational volume surface[50].

2.2.3.Early-age swelling

During the hydration process of OPC paste, the volume changes include shrinkage and swelling. The reaction during cement hydration causes chemical shrinkage of OPC concrete. Moreover, the consumption of capillary water during hydration could cause autogenous shrinkage of OPC concrete[51].

The formation of specific minerals (e.g. portlandite and ettringite) could cause expansion[52], [53]. This period of expansion, which initiates shortly after set, provides a considerable benefit in shrinkage mitigation even at longer time scales [54]. The impact of the expansion in mitigating autogenous shrinkage is considerable, as the expansion can amount to up to 60% of the reduction in unrestrained shrinkage under sealed conditions [55].

A hypothesis for early-age swelling in cement-based materials is based on crystallization-induced stress from the rapid formation of hydration products within confined pore spaces. As supersaturation of the pore solution increases during early hydration, minerals such as ettringite and portlandite begin to precipitate. In small capillary or gel pores, this precipitation can generate crystallization pressure due to volume expansion, pushing against the pore walls and leading to measurable expansion of the paste. This mechanism is independent of capillary pressure collapse and may be enhanced using finely divided SCMs, which promote localized nucleation and accelerate the buildup of internal stress[56]. Moreover, the type of SCM used can significantly influence the extent of early-age expansion. Variations in chemical composition, particle size, and reactivity lead to different rates of hydration product formation, which in turn affect crystallization pressure and expansion behavior. Wu et al. discovered the incorporation of Silica Fumes refined the pore size distribution, therefore enhances the crystallization stress and results in a large early-age expansion[57]

2.2.4.Presence of water

Water plays a multifaceted role in cementitious systems, influencing hydration, pore structure development, and volume stability. It is generally classified into chemically bound water, physically adsorbed water, and free or capillary water, each contributing differently to material performance[58]. Chemically bound water is integrated into hydration products such as C–S–H, ettringite, and portlandite, and represents an irreversible component of the solid phase. Physically adsorbed water, on the other hand, is held by surface forces within gel and small capillary pores, and its content is governed by relative humidity (RH). Studies have shown that adsorbed water forms multi-molecular layers, the thickness of which increases non-linearly with RH[59].

Capillary water refers to the water residing in the capillary pores of cementitious materials, held by surface tension forces but not chemically bound to hydration products. Unlike chemically or physically bound water, capillary water is mobile and plays a key role in fluid transport, hydration, and volume stability. As hydration progresses or as the material dries, the reduction of capillary water leads to the development of capillary pressure within the pore network[60]. This

pressure is the primary driving force behind autogenous shrinkage and drying shrinkage [61]. Therefore, capillary water strongly governs the shrinkage behavior of cement-based materials.

Figure 2.3 illustrates the nanostructure of C-A-S-H gel, showing how water is distributed as interlayer, adsorbed, and capillary water, with capillary water occupying larger pores and playing a key role in shrinkage.

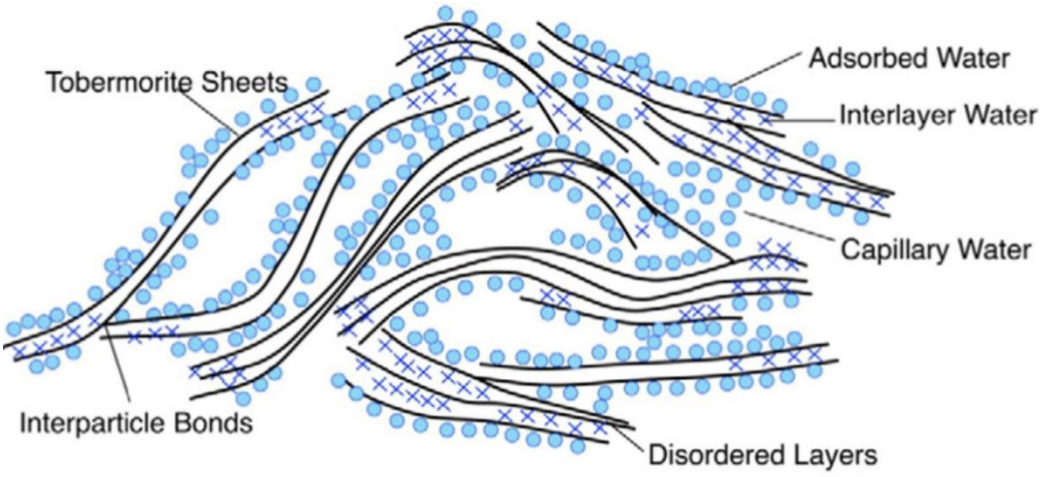

Figure 2.3 Illustration of nanostructure of C-A-S-H gel[62].

2.3.Mechanisms of autogenous and drying shrinkage of cement paste

2.3.1.Mechanism of autogenous shrinkage

Autogenous shrinkage refers to the volume shrinkage of cementitious materials under sealed and isothermal conditions, where no moisture exchange with the environment occurs. It is a specific form of autogenous shrinkage, which includes both shrinkage and possible expansion. Among the different causes of autogenous shrinkage, shrinkage due to hydration-induced volume loss is the most common and critical in modern low water-to-binder ratio systems.

The root cause of autogenous shrinkage is chemical shrinkage, a phenomenon in which the absolute volume of hydration products is less than the total volume of the original cement and mixing water[63]. During the hydration of Portland cement, this chemical shrinkage typically amounts to 6–7 mL per 100 g of cement consumed[64]. When the cement paste is still in its fluid state, this volume loss manifests as external shrinkage, since the system lacks mechanical resistance.

As hydration proceeds, a continuous network of solid hydration products begins to form, increasing the stiffness of the matrix and preventing further bulk collapse. However, the ongoing consumption of water leads to a progressive

emptying of the pore structure. This triggers the formation of water–air menisci within capillary pores (see Figure 2.4, which causes a drop in internal relative humidity (RH) according to Kelvin's law [65]. The emergence of curved menisci also generates tensile stresses in the pore liquid, as described by Laplace's law, accelerating self-desiccation shrinkage.

In addition, the reduction in RH affects the thickness of adsorbed water layers on the surfaces of solid particles [66]. This results in changes in both surface tension and disjoining pressure, which further destabilize the microstructure. At this early age, the mechanical stiffness of the paste remains low, and its viscous nature makes it highly sensitive to internal stresses—such that even slight internal tension may lead to substantial deformation.

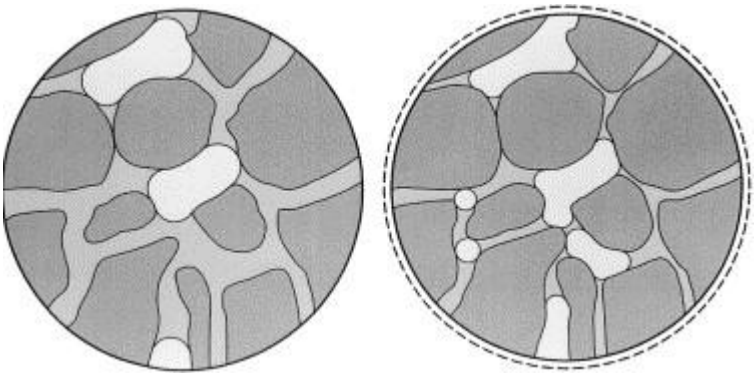

Figure 2.4. Schematic representation of a cross section of a hydrating cement paste. Left: low degree of hydration. Right: high degree of hydration[67].

2.3.2.Mechanism of drying shrinkage

The shrinkage of OPC concrete is governed by several different mechanisms, including capillary pressure, solid surface energy, disjoining pressure, and interlayer water movement. These mechanisms vary in dominance depending on the surrounding RH.

At RH levels above 40%–50%, shrinkage is primarily driven by capillary pressure, which arises due to the formation of menisci in mesopores as water evaporates during drying. This surface tension of pore water creates negative pressure within the pores, leading to volumetric shrinkage of the concrete. Studies have shown that this mechanism is particularly active within this RH range[68], [69]. Supporting evidence from Parrott and Jennings [70], [71] indicates that the BET surface area of OPC is minimized around 40%–50% RH, highlighting the prevalence of capillary-driven shrinkage in this range.

When drying occurs below 40% RH, capillary menisci become unstable due to the decrease in pore radius (Kelvin radius ~1–2 nm), altering the moisture loss behaviour and shifting the dominant shrinkage mechanism [32]. Research by Maruyama et al. [68] shows that shrinkage occurring at low RH is largely reversible upon rewetting and correlates linearly with BET surface area, suggesting a transition to shrinkage driven by solid surface energy. In this mechanism water molecules adsorbed on the surfaces of solid skeletons reduce surface tension[72], [73]. As these molecules evaporate, surface

tension increases, causing shrinkage.

Another explanation involves disjoining pressure[74], [75], which refers to the pressure resisting adsorption forces between adjacent solid surfaces in nanopores, mediated by van der Waals interactions. This pressure is balanced by spreading pressure from adsorbed water layers. As RH drops, adsorbed water layers thin, spreading pressure declines, and disjoining pressure is released—leading to shrinkage of the solid framework. However, the significance of this mechanism is still debated: some researchers [76]argue it plays a major role even across a broad RH range, while others [77] believe its impact is limited or negligible, especially above 40% RH.

Lastly, the interlayer water movement hypothesis posits that water transport within gel interlayers also contributes to volume changes in concrete[78], offering yet another dimension to the complex nature of OPC shrinkage.

2.4.Effect of BFA and MSWI BA on autogenous and drying shrinkage

2.4.1.Effect of BFA

Direct, systematic studies on BFA's influence are still limited, but adjacent evidence points to mitigation pathways via internal curing and/or mild expansive reactions. Mortar tests with wood biomass ash reported substantial reductions in autogenous shrinkage[79], highlighting the role of ash porosity and retained water; similar internal-curing benefits have been observed with other biomass-derived additions. Broader fly-ash literature (primarily coal fly ash) shows a decreasing trend of autogenous shrinkage with higher BFA replacement, reinforcing the plausibility that BFA—especially high-CaO, porous types—can partially offset autogenous strains, though targeted BFA studies resolving ash chemistry, fineness, and curing are still needed[80].

BFA with high CaO—can reduce drying shrinkage in a long-term behaviour compared with OPC. In a long-term concrete study, replacing 15–30% of cement with high-CaO BFA cut one-year drying shrinkage by up to 65%; the 30% mixture even showed slight early-age swelling attributed to portlandite and brucite formation, without cracking or loss of long-term strength[81]. In self-compacting concrete, replacing coal fly ash with biomass wood ash increased drying shrinkage during the first ~7–14 days, but the rate slowed thereafter, and the final shrinkage converged to the reference mix, plausibly due to an internal-curing effect from the porous ash; the authors recommend keeping the replacement ≤30% by mass[82].

2.4.2.Effect of MSWI BA

When MSWI BA is used as a pre-saturated fine aggregate, it functions as an internal-curing reservoir and consistently reduces autogenous shrinkage in low w/b systems—e.g., high-performance mortars showed autogenous strains nearly eliminated, and pervious/UHPC systems reported large reductions (≤~140 με at 28 d), attributed to sustained internal RH after setting[83]. In

contrast, grinding MSWI BA to a powder and using it as a SCM removes the internal-curing role; studies on milled MSWI BA document altered early-age volume change dominated by H_2 gas evolution from metallic Al, implying no mitigation of self-desiccation and autogenous shrinkage[84]. Moreover, fineness-driven evidence from ash-binder systems shows that finer ashes increase autogenous shrinkage at a given replacement—by pore refinement and higher capillary stresses—providing a clear case were using ash as a finely ground SCM raises autogenous shrinkage relative to coarser ash[85].

When MSWI BA is recycled as construction materials, most studies report higher drying shrinkage and a clear increase with MSWI BA content. A recent critical review concludes that MSWI BA replacement raises water absorption and air porosity and consequently increases drying shrinkage in both mortar and concrete[86]. Mechanistically, pretreated MSWI BA can release water before setting, effectively raising the paste's water-to-binder ratio rather than providing true internal curing—an effect observed to amplify drying-shrinkage strains. Experimental campaigns on self-compacting mortars similarly note a gradual rise in drying shrinkage as MSWI BA dosage increases[87]. When MSWI BA is finely ground and used as a SCM, mortar mixes also show increasing drying shrinkage with higher content, accompanied by higher porosity[88].

2.5.Conclusion

Early-age volume change in cementitious systems is the macroscopic outcome of two competing processes—expansion and shrinkage—measured from the moment of final setting. For expansion, crystallization pressure and early ettringite formation are most frequently cited. For autogenous and drying shrinkage, the prevailing explanations invoke the consumption of capillary water and attendant capillary tension and crystal pressure, changes in surface energy of the gel, and disjoining-pressure effects, each effective over different internal RH ranges. When alternative ashes are introduced, additional variables arise: BFA exhibits composition-dependent behaviour (e.g., CaO content, fineness), while MSWI BA shows strong "usage-mode" sensitivity (pre-saturated aggregate versus finely ground SCM). These factors complicate direct transfer of empirical expressions calibrated on ordinary Portland cement systems.

The present work is therefore designed to quantify how replacing cement with BFA and MSWI BA modifies both drying shrinkage and autogenous shrinkage from early to later ages. Drying shrinkage will be evaluated under well-defined RH by relating strain development to pore-structure evolution; autogenous shrinkage will be measured in sealed conditions alongside early-age stiffness. The outcome is a mechanism-informed basis for selecting ash type, dosage, and usage mode to minimize volume change while meeting performance targets

3. Materials and Methods

3.1.Introduction

This chapter presents the materials, methodology, and experimental setup adopted in the study to evaluate the volume stability of cementitious systems incorporating BFA and MSWI BA. The physical and chemical properties of the materials are described. The methodology section outlines a two-stage approach: testing to assess workability, mechanical performance, and shrinkage behaviour, followed by investigating pore structure and reaction products and kinetics. In addition, the experimental setup is presented in detail to ensure reproducibility and to clarify the procedures used for sample preparation and testing.

3.2.Experimental setup

3.2.1.Test on raw materials

- Chemical composition

  X-ray fluorescence spectroscopy (XRF) was used to analyze the chemical composition of each material in accordance with EN 196-2[89]. Samples were first oven-dried and ground to a fine powder before testing. The analysis was performed using a wavelength-dispersive XRF spectrometer to determine the major and minor oxides.

- Mineralogical composition

  X-ray diffraction (XRD) analysis was performed in accordance with EN 196-2 [89]. Finely ground samples were scanned using a Cu-Kα radiation source over a typical 2θ range of 5–90°. Phase identification was conducted using reference patterns from the COD database. For hydrated pastes, measurements were taken after predetermined curing ages to monitor the development of hydration.

- Particle size distribution

  Particle size distribution was measured using laser diffraction in accordance with ISO 13320[90]. Prior to testing, samples were oven-dried and dispersed in isopropanol to prevent agglomeration. The analysis provided cumulative particle size distribution curve to characterize the fineness and gradation of each material.

- Morphology

  The morphology of selected raw materials was examined using scanning electron microscopy (SEM) following the procedure in ISO 16700[91]. Samples were dried, finely ground, and coated with a thin layer of gold or carbon to ensure conductivity. Images were captured under high vacuum at various magnifications to assess particle size, shape, and surface texture.

3.2.2.Fresh properties

- **Workability**

  The workability of the paste was assessed using the mini-slump flow test, in accordance with EN 1015-3[92]. Freshly mixed paste was poured into a truncated conical mold placed on a smooth surface (Figure 3.1). Upon lifting the mold, the spread diameter of the paste was measured in two perpendicular directions, and the average was recorded as the flow value.

Figure 3.1. Vibration table for workability test.

- **Setting time**

  The setting time was measured using the Vicat method in accordance with NEN-EN 196-3[93]. An automatically recording Vicat apparatus (Controls VICATMATIC 2, CONTROLS Group, Milan, Italy) was used (Figure 3.2. Vicat apparatus.). Paste was cast into standard Vicat moulds and tested continuously until the final setting time was automatically recorded by the device.

Figure 3.2. Vicat apparatus.

3.2.3.Mechanical properties

- **E-modulus**

  Elastic modulus was measured according to EN 13412[94]. Paste samples were cast into prisms （40mm ×40mm×285mm） and cured for 7 days under sealed conditions at 20 ±1° C. The test was conducted using a compression testing machine, with axial deformation measured by two linear variable differential transformers （LVDTs） directly affixed to the specimen surface at the mid-span (Figure 3.3). A compressive load was applied incrementally up to 10% of the estimated maximum load, and corresponding deformation was recorded. The modulus of elasticity was calculated from the linear portion of the stress–strain curve.

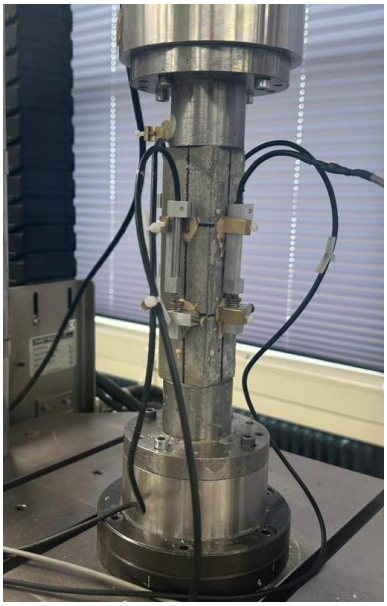

Figure 3.3. Setup for E-modulus test.

- **Compressive strength**

  Compressive strength tests were carried out in accordance with EN 196-1[95]. Paste samples were cast into 40mm ×40mm ×160mm prism moulds, demoulded after 24 hours, and cured under controlled conditions (20 ±1° C, >95% RH) for 1,7,28 days. At specified curing ages, specimens were broken into halves, and the compressive strength was measured on the broken sections using a universal testing machine. The average of three specimens was reported for each data point.

- **Flexural strength**

  Flexural strength was determined using a three-point bending test in accordance with EN 196-1[95]. Paste was cast into 40 mm × 40 mm × 285 mm prism moulds, demoulded after 24 hours, and cured under standard conditions (20 ±1° C, >95% RH) for 1,7,28 days. At the testing age, each prism was placed on two supports 100 mm apart and loaded at the centre until fracture (Figure 3.4). The average of three samples was recorded.

Figure 3.4. Setup for flexural strength test (three-point bending test).

3.2.4.Autogenous and drying shrinkage

- **Autogenous shrinkage**

  Freshly mixed paste was cast under vibration into corrugated plastic tubes (LDPE, Ø 29 mm, length ≈ 430 mm) to minimize restraint with ASTM C1608[96]. Measurement of autogenous shrinkage started after the final setting time, determined by Vicat testing. Prior to that, the specimens were placed on a self-manufactured rotation machine (10 rpm) to prevent bleeding (Figure 3.5 left). After setting, the specimens were held in a frame consisting of two steel plates rigidly joined by six solid invar rods (Figure 3.5 right). Each specimen was gripped at one end, while the other end remained free to move. Longitudinal deformation was recorded at the free end using a displacement transducer (TRANS-TEK 350-000, accuracy ±5 μm). Measurements were taken every 5 minutes, with three specimens tested simultaneously.

Figure 3.5. Rotation machine (left) and autogenous shrinkage test device (right).

- **Drying shrinkage**

  Drying shrinkage was tested in accordance with EN 12617-4[97]. Paste samples were cast into 40mm ×40mm ×285mm moulds and cured under standard conditions (20 ±1° C, >95% RH) for 28 days. After initial curing, the specimens were exposed to drying conditions (20 ±1° C,50±5%RH), and the length change was monitored periodically using a length

comparator(Figure 3.6). The reported shrinkage value corresponds to the difference between the initial and current lengths divided by the original length.

Figure 3.6. Setup for drying shrinkage measurement

3.2.5.Microstructure

- **Pore structure**

  Pore structure was analysed using mercury intrusion porosimetry (MIP) in accordance with ISO 15901-1[98]. Paste samples were cured for 28 days, then solvent-exchanged with isopropanol and vacuum-dried to preserve the pore structure. The MIP test was conducted using a porosimeter capable of measuring intrusion pressures up to 400 MPa, providing access to pore diameters ranging from approximately 7 nm to 100 µm. Cumulative pore volume and threshold pore diameter were obtained from the intrusion curves, and this pore-size window covers the medium and large capillary pores that predominantly govern moisture transport, capillary tension and thus the autogenous and drying shrinkage behaviour investigated in this study.

- **Reaction kinetics**

  Isothermal calorimetry was performed in accordance with ASTM C1679[99]. Freshly mixed paste （approximately 5g） was sealed in glass ampoules and placed in an isothermal calorimeter (TAM Air, TA Instruments) maintained at 20 $\pm 0.1^{\circ}$ C. Heat flow was recorded continuously for 168 hours. The cumulative heat release and heat flow rate curves were used to assess the hydration behaviour of the mixtures.

- **Hydration products**

  XRD and QXRD tests were conducted as mentioned in Test on raw materials at 3 days of curing.

3.3.Materials

This study utilized three primary materials: BFA, MSWI BA (the following text is collectively referred to as MSWI BA), and ordinary Portland cement (CEM I 42.5N). The chemical composition, particle size distribution, and morphology of these materials were characterized prior to use.

3.3.1.Chemical composition

The chemical composition of MSWI BA, BFA, and CEM I 42.5N was determined by X-ray fluorescence (XRF), and the results are presented in Table 3.1. All three materials contain significant amounts of silicon (SiO_2), calcium (CaO), and aluminium (Al_2O_3), which are relevant for their potential cementitious or pozzolanic reactivity.

MSWI BA exhibited a relatively high content of Fe_2O_3 (9.90%) and moderate CaO (14.67%), while BFA had high CaO (49.59%) and the highest SiO_2 content (17.62%) among the three. In contrast, CEM I 42.5N showed the highest CaO concentration (64.96%) and relatively low loss on ignition (LOI = 1.00%). BFA displayed a notably high LOI of 7.43%, suggesting the presence of unburnt carbon or other volatiles.

Minor oxides such as Na_2O, K_2O, MgO, and SO_3 were also detected, along with trace elements like Cr_2O_3, MnO, and CuO. These components may influence hydration behavior, durability, and environmental compliance.

Table 3.1 Chemical composition of raw materials.

	MSWI BA	BFA	CEM I
CaO	14.67	49.59	64.96
SiO_2	54.9	17.62	16.23
Al_2O_3	8.76	5.03	3.76
Fe_2O_3	9.9	3.45	4.18
K_2O	1	5.56	0.7
MgO	2.06	3.52	1.81
P_2O_5	0.55	4.41	—
Na_2O	4.93	1.04	0.31
TiO_2	1.03	1.86	0.5
MnO	0.15	0.49	0.08
SO_3	0.46	4.58	6.07

Cr_2O_3	0.11	0.04	0.03
V_2O_5	0.01	—	0.02
Cl	0.29	1.8	0.05
CuO	0.37	0.06	—
LOI	0.27	7.43	1

[a] LOI = Loss on ignition.

3.3.2.Mineralogical composition

The XRD patterns of BFA and MSWI BA (Figure 3.7 and Figure 3.8) reveal dominant crystalline phases such as quartz and calcite, along with various minor minerals, indicating the heterogeneous and partially crystalline nature of the ashes.

The mineralogical compositions of BFA and MSWI BA are summarized in Table 3.1 and Table 3.3. based on the internal standard method, the calculated amorphous contents are 38.34% or BFA and 69.2% for MSWI BA. These high amorphous proportions indicate that both ashes are highly heterogeneous.

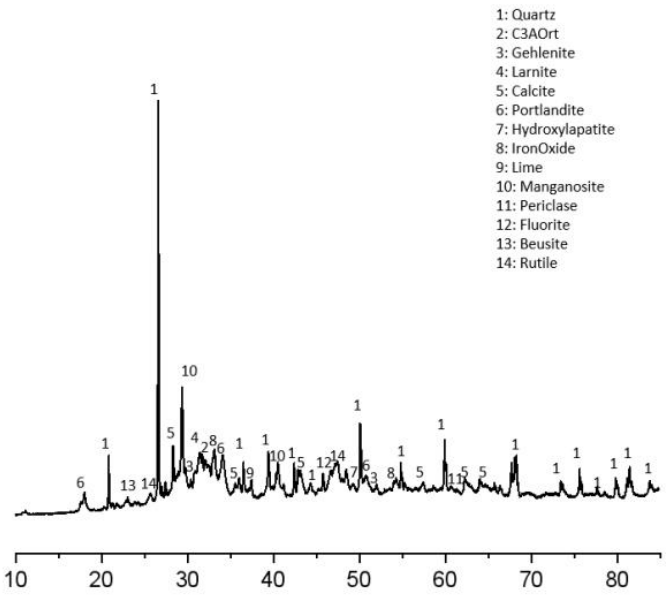

Figure 3.7.XRD result of BFA

Table 3.2. Mineralogical composition of BFA

No.	Mineral Name	Chemical Formula	Proportions (wt%)	ICSD Codes
1	Quartz	SiO_2	19.51	541929
2	Tricalcium aluminate (C_3A Orth.)	$Ca_3Al_2O_6$	2.51	1880
3	Gehlenite	$Ca_2Al(AlSi)O_7$	2.60	1411155
4	Larnite	Ca_2SiO_4	3.98	39006
5	Calcite	$CaCO_3$	13.42	11611066
6	Portlandite	$Ca(OH)_2$	3.67	191851
7	Hydroxylapatite	$Ca_5(PO_4)_3(OH)$	5.61	60521
8	IronOxide	Fe_3O_4 / Fe_2O_3	1.54	15840
9	Lime	CaO	0.41	60199
10	Manganosite	MnO	0.66	9864
11	Periclase	MgO	2.01	52026
12	Fluorite	CaF_2	1.85	44937
13	Beusite	$(Mn^{2+},Ca,Mg)_3(PO_4)_2$	2.51	71051
14	Rutile	TiO_2	1.35	9161
-	Amorphous	-	38.34	

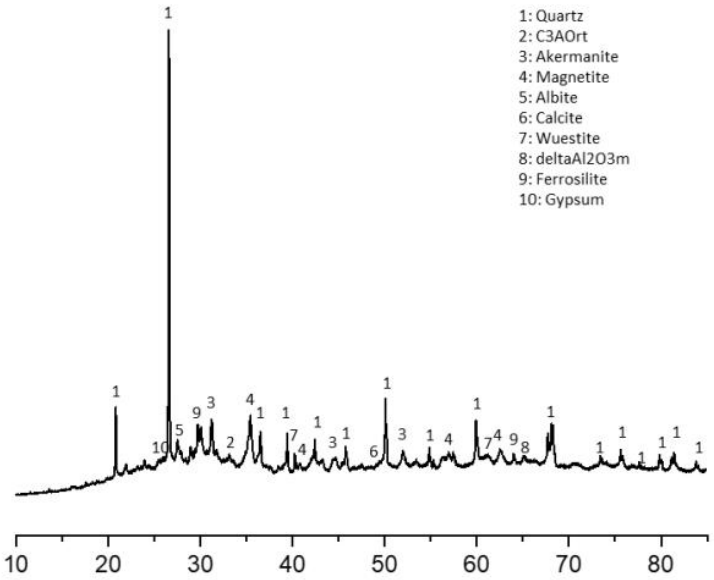

Figure 3.8. XRD result of MSWI BA

Table 3.3. Mineralogical composition of MSWI BA

No.	Mineral Name	Chemical Formula	Proportions (wt%)	ICSD codes
1	Quartz	SiO_2	12.85	541929
2	Tricalcium aluminate (C_3A Orth.)	$Ca_3Al_2O_6$	0.61	1880
3	Akermanite	$Ca_2MgSi_2O_7$	4.50	26683
4	Magnetite	Fe_3O_4	1.75	92356
5	Albite	$NaAlSi_3O_8$	3.08	1402109
6	Calcite	$CaCO_3$	0.52	1611066
7	Wuestite	FeO	0.55	309924
8	Delta-alumina (δ-Al_2O_3)	Al_2O_3	1.59	40200
9	Ferrosilite	$FeSiO_3$	4.88	36049
10	Gypsum	$CaSO_4 \cdot 2H_2O$	0.46	160977
-	Amorphous	-	69.2	

3.3.3.Morphology

The morphology of MSWI BA and BFA was examined using scanning electron microscopy (SEM) following ASTM C1723[100], as presented in . The two materials exhibit distinct particle characteristics, which are expected to influence their behaviour in paste mixtures.

MSWI BA particles (left image) are angular and relatively smooth, with a dense structure and minimal visible porosity. The particles vary in size but show compact shapes, which may contribute to efficient packing and moderate water absorption. The lack of significant surface roughness suggests a lower tendency for water retention compared to highly porous materials[101], [102].

BFA particles (right image) are highly porous and agglomerated, with rough surface texture. Such morphology implies a higher effective surface area and greater surface water uptake, leading to higher water demand and reduced flow [103].

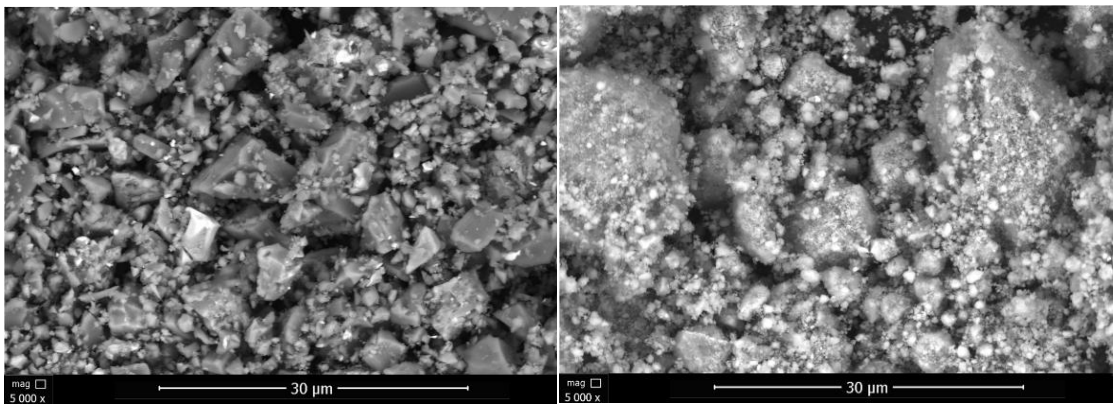

. Figure 3.9. SEM pictures of MSWI BA (left) and BFA (right)

3.3.4.Particle size distribution

The particle size distribution of MSWI BA, BFA, and CEM I 42.5N was measured using laser diffraction following ASTM B822[104] (Figure 3.10). Among the three materials, MSWI BA exhibited the finest particle size, followed by BFA and then cement. The finer particle size distribution of MSWI BA suggests higher specific surface area, which may increase water demand and influence its reactivity. In contrast, cement showed the coarsest distribution, with BFA displaying intermediate characteristics[105]. The variation in particle size among the materials is expected to affect both the fresh and hardened properties of the paste mixtures.

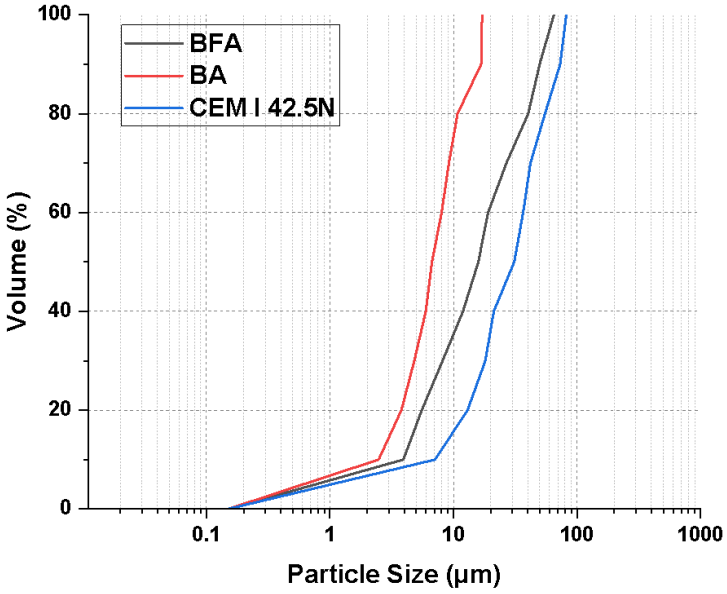

Figure 3.10. Particle size distribution test results.

3.3.5.Pretreatment

To minimize the negative effects of metallic aluminium in MSWI BA on early-age performance, a chemical pretreatment was applied. The MSWI BA was mixed with a 0.1 mol/L NaOH solution at a water-to-solid ratio of 0.3, forming a slurry. The slurry was stirred and maintained under ambient conditions for three weeks to promote the dissolution and removal of residual metallic aluminium. This pretreatment aims to reduce hydrogen gas evolution during hydration and to mitigate its potential impact on strength and shrinkage measurements[106], [107].

3.4.Mixture design

Nine paste mixtures were designed to investigate the influence of MSWI BA and BFA on shrinkage behaviour and mechanical performance. The control mix (B1) contained 100 wt% CEM I 42.5N, while the remaining mixes (B2–B9) included varying proportions of MSWI BA and BFA, as detailed in Table 3.4.

The maximum replacement level for MSWI BA was limited to 20 wt% due to concerns over potential leaching of heavy metals at higher dosages, as identified in preliminary testing[108], [109]. BFA in this study contains 1.8 wt% Cl^- (Table 3.1). To respect the total chloride limits for structural concrete in EN 206 / BS 8500 (0.10% for prestressed; 0.20–0.40% for reinforced, by mass of cement), the default BFA replacement is capped at 6%; at 10% replacement the chloride input approaches the 0.20% class and is considered only with mitigation (e.g., washing/blending and verification against the project chloride class)[110], [111]. Therefore, when MSWI BA and BFA were used together, the proportion of BFA was deliberately reduced to minimize negative effects while still utilizing both materials.

This mixture design allows for systematic evaluation of the individual and combined effects of MSWI BA and BFA at total ash replacement levels ranging

from 5% to 30%, with a focus on optimizing performance and ensuring environmental safety.

Table 3.4 Mix proportions of paste samples with varying ash replacement levels.

Paste Samples	Raw Materials(wt%)			Total Ash Replacement (wt%)
	CEM I 42.5N	MSWI BA	BFA	
B1	100	0	0	0
B2	95	0	5	5
B3	90	0	10	10
B4	90	10	0	10
B5	85	10	5	15
B6	80	10	10	20
B7	80	20	0	20
B8	75	20	5	25
B9	70	20	10	30

3.5.Methodology

The objective is to provide actionable mix-design guidance for using BFA, and MSWI BA, as SCMs. Fresh properties and mechanical properties are assessed first because they control applicability[112]. Volume stability is equally critical, since shrinkage-induced cracking and microstructural damage accelerate degradation, and reduce service life[113], [114]. Volume stability is examined in two regimes. Early age under sealed conditions is dominated by autogenous shrinkage[115]. Deformation under exposure is governed by drying shrinkage, consistent with ASTM C157/C157M practice for drying-shrinkage evaluation[116].

In Stage 1, each mixture at a defined replacement level is characterized consistently by key macroscopic behaviors. Fresh properties are measured to EN 196-3 and EN 1015-3[117], [118]. Autogenous shrinkage is determined on paste by the corrugated-tube method in ASTM C1698[119] under sealed curing. After 28 days of sealed curing, drying shrinkage is measured as length change following the environmental and procedural controls of ASTM C157[116]. These data establish the main trends and isolate mixes that warrant mechanistic analysis.

Stage 2 explains the reasons behind the phenomenon：

Early-age volume change is governed by autogenous shrinkage, chemical shrinkage, and any early swelling. Its magnitude results from the interaction between stiffness evolution and capillary tension induced by self-desiccation. To resolve the causes of early deformation, isothermal calorimetry (ASTM C1702[120]) is used to track reaction kinetics and degree of hydration, which indicate the timing and intensity of capillary-stress build-up; quantitative X-ray diffraction (ASTM C1365[121], internal-standard approach) identifies reaction products to explain sources of early swelling (e.g., ettringite/syngenite formation) and static elastic modulus is obtained following ASTM C469/C469M[122] (adapted to paste geometry) to capture stiffness that restrains or amplifies deformation.

Post-28-day exposed deformation is governed by drying shrinkage. Its magnitude depends on capillary tension and on stiffness. Characterisation therefore relies on mercury intrusion porosimetry (ASTM D4404[123]) to determine pore-size distribution and cumulative intrudable pore volume for interpreting capillary forces, together with elastic modulus (ASTM C469/C469M) to quantify the material's compliance. Drying is performed under a standardised exposure consistent with ASTM C157/C157M[124] (20 ± 2 °C, 50 ± 4 % RH) to ensure comparability among mixtures.

Finally, deformations and microstructural findings are integrated to build explicit links between ash dosage and the observed autogenous and drying shrinkage. The results provide a mechanistic basis for recommending practical ranges of BFA and MSWI BA contents and proportions that enhance volumetric stability while preserving fresh and mechanical performance.

4. Fresh and Mechanical Properties

4.1.Introduction

This chapter presents the fresh and mechanical properties of paste mixtures incorporating BFA and MSWI BA at a constant water-to-binder ratio. Nine mixes were designed to isolate the individual and combined effects of BFA and MSWI BA on fresh and mechanical properties over 0–30 wt% total replacement. The results are organized as follows: fresh properties (workability, setting time), and mechanical properties (compressive strength and elastic modulus). Fresh and mechanical properties are decisive for the practical applicability of mixes with BFA and MSWI BA: they determine whether a mix design can be applied. In particular, the elastic modulus is directly linked to shrinkage in both regimes—under sealed curing and under exposure.

4.2.Fresh properties of cement paste

4.2.1.Workability of paste

Figure 4.1 and Figure 4.2 are slump and flowability test results of 9 different mixes, showing that at a fixed water-to-binder ratio, replacing CEM I with ashes progressively reduced workability across B1–B9 Slump declined from 42 to 28 mm, around 33%, while flow decreased from ~280 to 220 mm around 21%. Because the mixing water was held constant (Table 3.4), these losses are attributed to particle's small size and porous morphology.

Particle size distribution result (Figure 3.10) shows that MSWI BA is the finest, BFA intermediate, and cement the largest. Finer particle size distribution raises specific surface and contact density, increasing yield stress and plastic viscosity[105], explains the trends that workability decreases with BFA and MSWI BA added. Morphology of raw materials (. Figure 3.9) further indicates MSWI BA is dense and angular, promoting interparticle friction, whereas BFA is porous, rough, and agglomerated, which demands more effective free water and increases internal friction[112], consolidate the negative effect about workability of BFA and MSWI BA. These results are in agreement with the findings of earlier research on ashes from other sources[125], [126].

Both BFA and MSWI BA reduce the workability of the blended mixtures. For the same total replacement level (10%, 20%), mixtures containing more MSWI BA exhibit a more pronounced loss of workability than those with BFA, indicating that MSWI BA has a stronger adverse effect on workability.

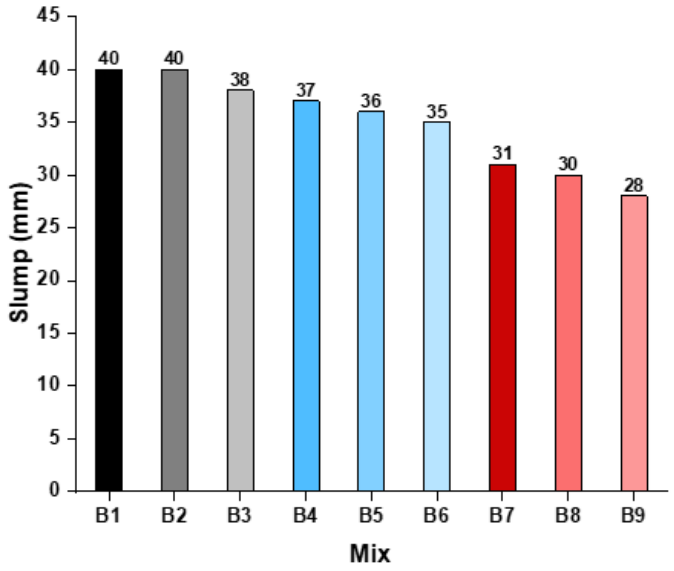

Figure 4.1. Slump test results (mix design refers to Table 3.4)

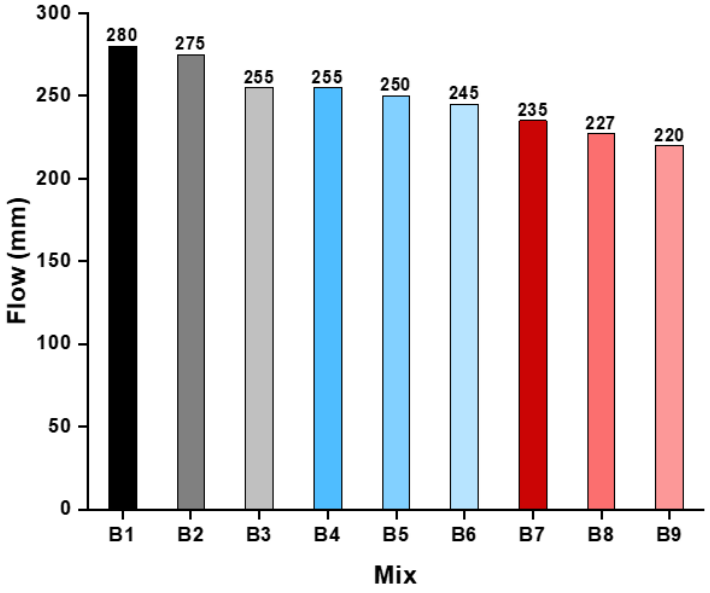

Figure 4.2. Flowability test results (mix design refers to Table 3.4)

4.2.2.Setting time of paste

Figure 4.3 is the final and initial setting time results of 9 different mixes, showing that the initial and final setting times increase progressively from B1 to B9. The phenomena can be attributed to the decrease proportion of reactive clinkers and the lower early reactivity of BFA and MSWI BA. Replacing part of the clinker with MSWI BA or BFA reduces the concentration of rapidly hydrating clinker phases such as C3S and C2S, and therefore postpones the formation of a rigid skeleton, delaying initial set[127], [128]. At the same total replacement level (10 % and 20 %), BFA generally causes a more pronounced increase in setting time than MSWI BA, which can be related to its finer particle size and higher contents of alkalis and sulphates. The binary mixture containing both BFA and MSWI BA at high replacement shows the largest retardation in setting. According to the chemical compositions in Table 3.1, this mixture combines the

lowest overall sulphate content with the strongest dilution of calcium from Portland cement. Such low sulphate and calcium content delays the formation of stable ettringite and the percolation of a continuous C–S–H skeleton, leading to the most pronounced extension of the dormant period and setting times. This observation is consistent with the reduced and delayed early heat release recorded by isothermal calorimetry (Figure 5.2 and Figure 5.3), which directly indicates slower early hydration.

Figure 4.3 shows that the increase in final setting time becomes much smaller than in initial setting time once setting approaches about 10 h. This reflects the transition to the later stages of hydration, where the solid C–S–H network has percolated and stiffness growth is increasingly controlled by space-filling and diffusion-limited reactions rather than by the initial ionic availability [129], [130]. In other words, once that continuous skeleton is established, subsequent hardening is dominated by slower, diffusion-controlled filling of remaining porosity and densification processes that proceed at similar rates across mixtures; consequently, the additional delay in final setting caused by slower early reactions tends to diminish and the final-set times converge[131]. MSWI BA and BFA mainly influence this stage by reducing the proportion of reactive clinker and slowing the initial dissolution of reactive phases of ashes such as gehlenite/akermanite, so that the formation of a continuous skeleton is delayed.

Both BFA and MSWI BA prolong the setting of the mixtures. At the same total replacement level (10%,20%), BFA causes a more pronounced increase in setting time than MSWI BA.

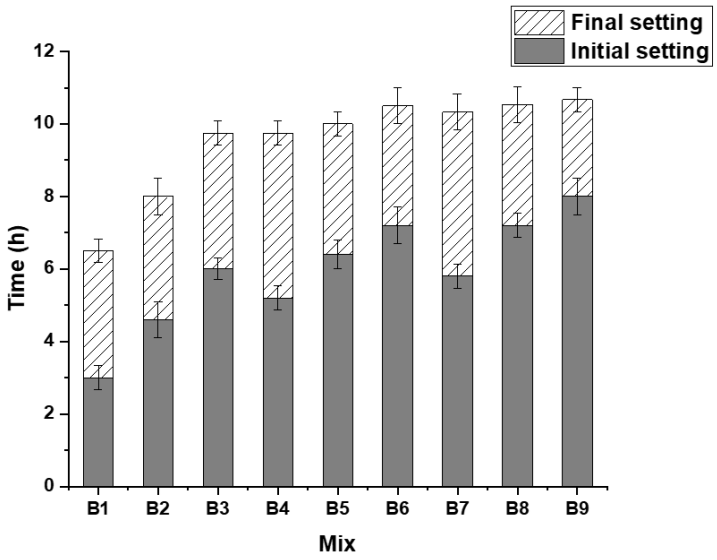

Figure 4.3 Setting time results (mix design refers to Table 3.4)

4.3.Mechanical properties of cement paste

4.3.1.Flexural and compressive strength of hardened paste

Figure 4.4 and Figure 4.5 are the results from flexural and compressive strength test of 9 different mixes. Across all curing ages, both flexural and compressive strengths increase with time, but at any given age the strength decreases as

the total ash replacement increases. The pure cement paste (B1) attains the highest strengths, low-replacement blends (B2–B3) are slightly lower, medium-replacement blends (B4–B6) are further reduced, and high-replacement blends (B7–B9) form the lowest cluster. The age-gain pattern is similar for all mixes—the dominant increase occurs from 1→7 d and the subsequent 7→28 d gain is modest—so ash replacement level primarily shifts the strength level downward without changing the late-age slope.

The strength loss with ash addition is primarily due to the low reactivity of BFA and MSWI BA. Mineralogical composition of raw materials (Table 3.2 and Table 3.3) shows both BFA and MSWI BA are dominated by quartz and calcite, with minor silicate phases such as gehlenite/akermanite and other accessory minerals. At 20 °C these crystalline phases are essentially inert in Portland systems over 1–28 d, while the amorphous fraction reacts only slowly and weakly[132], [133]. Replacing CEM I with BFA and MSWI BA decrease reactivity of binder, reducing early formation of C–S–H and AFt/AFm; the hydrates produced per unit paste volume decline, and the load-bearing skeleton develops more slowly, giving lower flexural and compressive strengths, hence the systematic, replacement-level-controlled drop in strength observed in Figure 4.4 and Figure 4.5. The overarching trend remains: more ash leads to lower strength due to reduced reactive binder content and slower hydrate formation, which is in line with earlier research[126], [134].

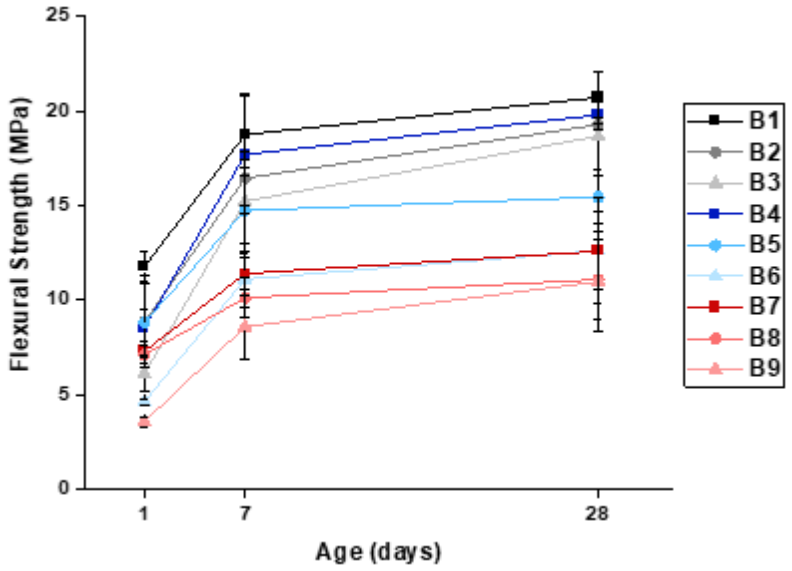

Figure 4.4. Flexural strength results (mix design refers to Table 3.4)

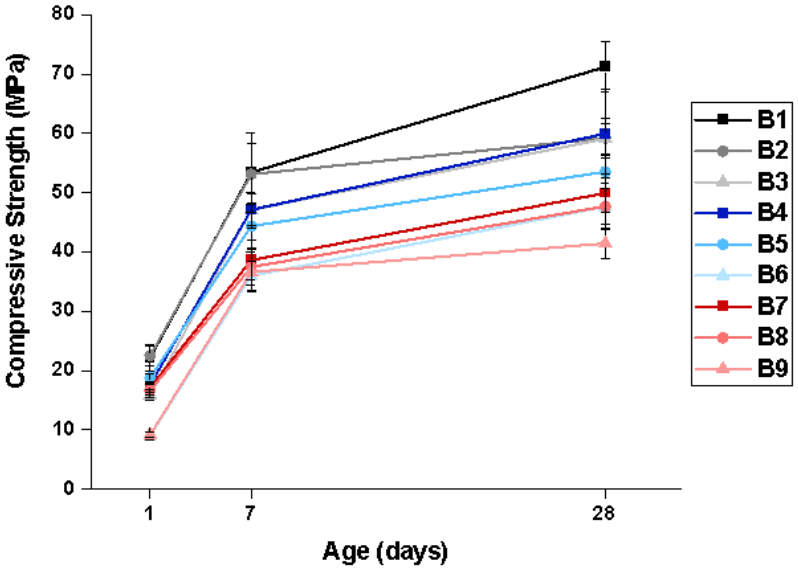

Figure 4.5 Compressive strength results (mix design refers to Table 3.4)

4.3.2.E-modulus of hardened paste

Figure 4.6 shows the evolution of E-modulus of 9 different mixes between casting and 28 days E-modulus increases rapidly to day 7 and then grows only marginally to day 28. At 7 days the spreads between mixes are still pronounced: B1 shows the highest stiffness, while ash-blended mixes are lower because the newly added BFA and MSWI BA exhibit lower early reactivity and contribute less to the formation of skeleton within the first week, when cement has already completed most of its hydration[132], [133]. By 28 days the curves converge, and differences become small, indicating gradual space-filling from the slower ash reactions that narrow the gap. The overall trend and ranking are consistent with the flexural and compressive strength results.

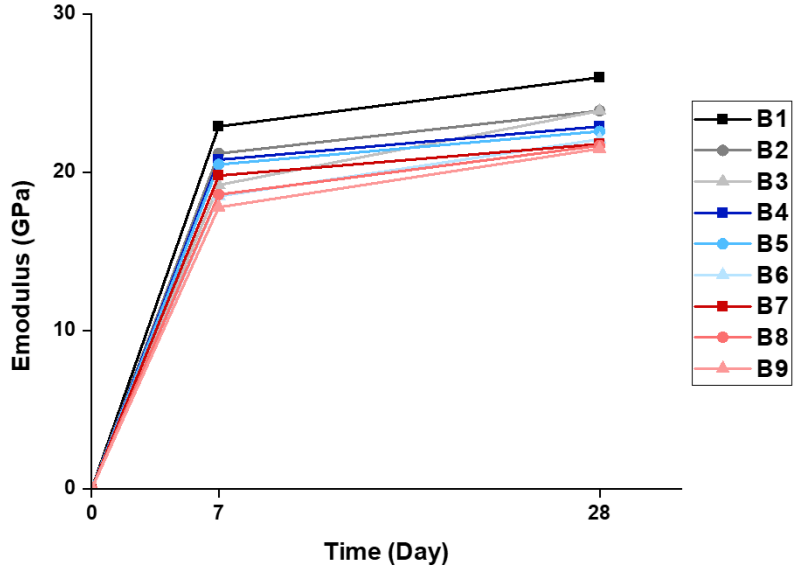

Figure 4.6 E-modulus test results (mix design refers to Table 3.4).

4.4.Conclusion

At a fixed water-to-binder ratio, replacing CEM I with BFA and MSWI BA systematically degrades fresh and mechanical performance.

- Increases in both BFA and MSWI BA replacement level consistently reduce workability; at the same replacement, MSWI BA decreases workability less than BFA.
- Both initial and final setting are delayed with replacement of both BFA and MSWI BA; the delay is stronger at initial set and generally larger for MSWI BA than BFA.
- Both compressive and flexural strength decrease monotonically with replacement level due to low reactivity of binder after BFA and MSWI BA are blended; most of the strength are established by 7 d, with slower growth of strength by 28 days from slower successive reactions.
- Elastic modulus rises rapidly to 7 d and only marginally thereafter; both BFA and MSWI BA blended mixes remain below CEM I paste at 7 days and 28 days.

5. Autogenous Shrinkage

5.1.Introduction

Autogenous shrinkage is the early-age volume reduction that occurs without external drying, driven by self-desiccation and the capillary stresses that develop as hydration consumes pore water. Under restraint it can cause microcracking, stiffness loss, and higher permeability—direct risks to durability and service life[63]. This chapter quantifies autogenous shrinkage of pastes with BFA and MSWI BA over 0–7 days, resolving the response into three successive parts—post-set deformation, transient swelling, and shrinkage after swelling [135], [136], [137]. The results provide mechanism-based guidance for mixture design and curing to control early-age shrinkage.

5.2.Results of autogenous shrinkage

Figure 5.1 shows the results of autogenous shrinkage of all mixes from final setting to 7 days and indicates a common response of magnitude of autogenous shrinkage across from B1 to B9: after an early swelling episode, autogenous shrinkage transitions to net shrinkage that proceeds approximately linearly over the 7-day. BA blended cement paste reduces the magnitude relative to B1, and BFA as well as BFA+ MSWI BA blended cement paste increase it. The rank order at day 7 is B7 < B4 < B1 < B2 < B8 < B5 < B6 < B3 < B9 (mix design refers to Table 3.4). For a fixed BA content (10%, 20%), increasing the BFA fraction leads to larger shrinkage; with 10% MSWI BA blended the order of autogenous shrinkage magnitude is B4 < B5 < B6, and with 20% BA blended the order is B7 < B8 < B9. Thus, MSWI BA mitigates autogenous shrinkage, most clearly in B7, whereas BFA and BFA+MSWI BA elevates it.

Autogenous shrinkage can be interpreted as the strain response of the material to internally generated stresses during hydration. Its magnitude is mainly governed by two aspects: (i) the stiffness of the material, and (ii) the internal driving forces. The driving forces in this context are primarily the crystallization pressure associated with the formation and growth of hydration products and the capillary tension arising from self-desiccation as water menisci retreat in the capillary pore network. As these internal driving forces evolve with the progress of hydration and dominate at different stages, they give rise to three characteristic patterns of autogenous shrinkage curves in this study.

The 7-day magnitude of early-age shrinkage can be divided into three components: the deformation after final setting, the amplitude of the ensuing swelling peak, and the post-swelling shrinkage[135], [136], [137]. For most mixes, final setting occurs during the chemical-shrinkage-dominated stage, so shrinkage has already accumulated at the start of measurement[63], [135]. B4 and B7 are exceptions: their final setting coincides with the onset of swelling, giving a higher initial baseline and a portion of swelling not captured within the record. After the swelling peak, the subsequent rate controls how fast shrinkage accrues; across mixes this rate aligns with the above ranking, reinforcing the mitigating role of MSWI BA and the amplifying role of BFA.

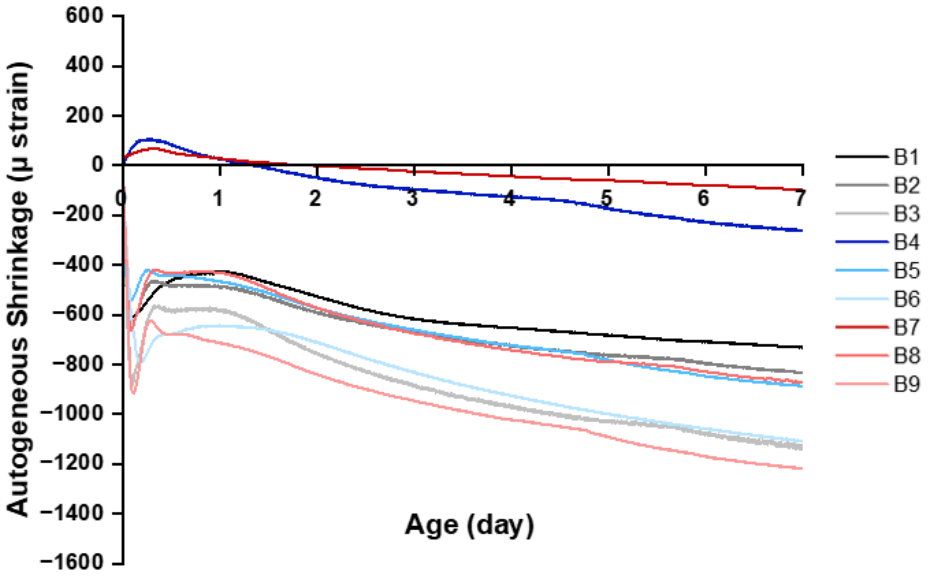

Figure 5.1. Autogenous shrinkage results (start from final setting, mix design refers to Table 3.4).

5.3.Deformation after final setting

From the Figure 5.1, except for B4 and B7, the final setting of all mixes occurs while the paste is already in the chemical-shrinkage–dominated period; therefore shrinkage begins to accumulate rapidly from the start of measurement, yielding higher magnitudes. By contrast, B4 and B7 reach final setting after chemical-shrinkage-dominant period, i.e., within the swelling period, so the measurement starts with a positive slope, and the initial accumulation is absent—which contributes to lower total shrinkage.

Figure 5.2 is the result of heat flow evolution considering dosage of BFA as variable over first 7 days, which indicate that across all groups, the curves follow a common evolution: after an initial induction period, the reaction enters a rapid heat-release stage with a main peak; the rate then declines and approaches a quasi-steady, slow-hydration regime by about day 3. Increasing BFA content systematically extends the dormant period and lowers the main-peak intensity, with the peak occurring later. This behavior is evident both in the BFA blended series (B1–B3) and in the mixes where MSWI BA is present (B4–B6, B7–B9). Quantitatively, 5% BFA extends the dormant period by about 3 h, and 10% BFA extends it by about 6.3 h, while concurrently reducing the main-peak heat flow, indicating suppressed early-age reactivity.

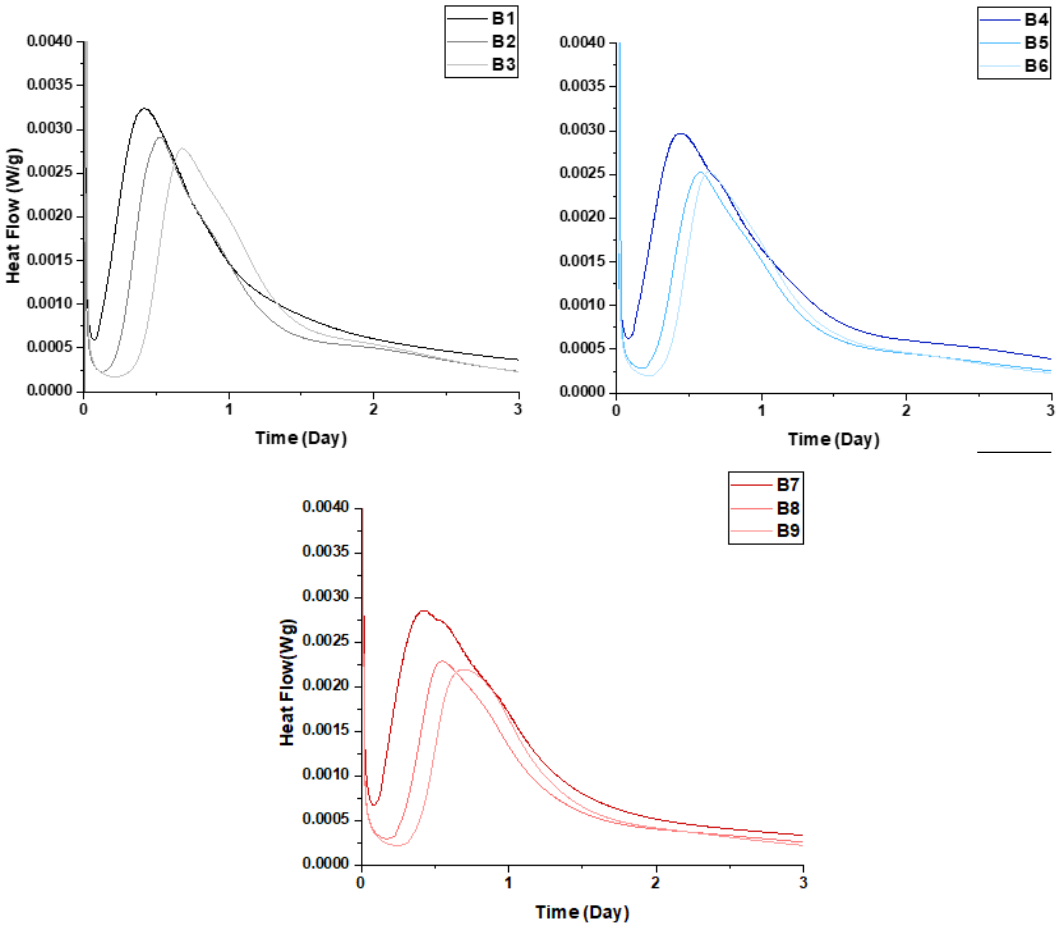

Figure 5.2. Heat Flow of 9 mixes (BFA dosage as variable, mix design refers to Table 3.4).

Figure 5.3 shows the results of heat flow evolution considering dosage of MSWI BA as variable over first 7 days and shows broadly the same evolution as Figure 5.2. Varying MSWI BA causes only a slight change in the induction period—dormant period is perturbed weakly compared with the effect of BFA. A clear effect appears in the acceleration region: increasing MSWI BA consistently lowers the main-peak heat flow. After the peak, the decay tails remain similar across MSWI BA levels, indicating that MSWI BA reacts continuously in early age. Overall, MSWI BA exerts a slight influence on dormant period and a pronounced reduction of the main peak, indicating reduced early reaction intensity while leaving the late, slow-hydration regime largely unchanged.

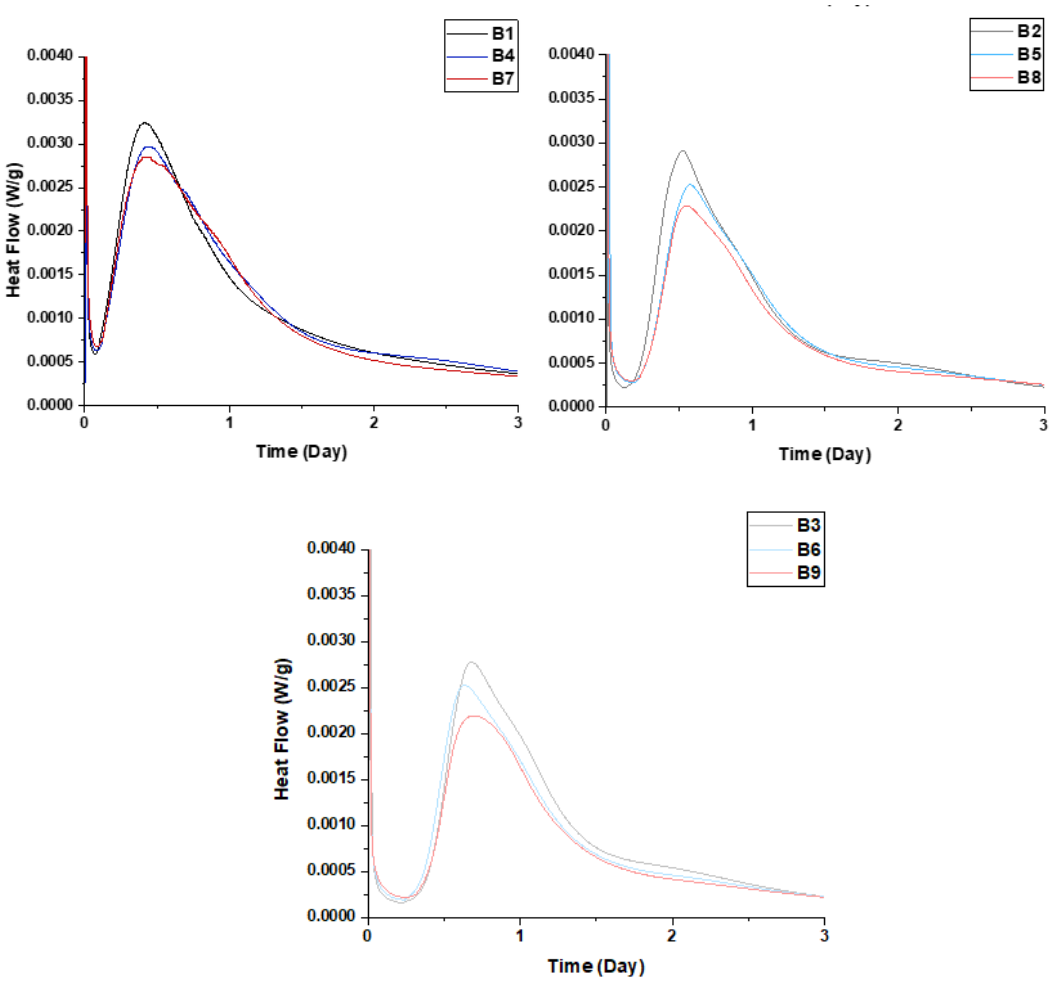

Figure 5.3 Heat Flow of 9 mixes (MSWI BA dosage as variable, mix design refers to Table 3.4).

From the calorimetry results, the chemical-shrinkage-dominant stage coincides with the first main peak and extends around appearance of the second peak. This interval corresponds to rapid hydration of alite and the build-up of chemical shrinkage[138]. The second peak reflects the aluminate–sulfate reactions that form ettringite and syngenite; once these crystallization reactions become active, the net deformation shifts from pronounced shrinkage to the onset of early-age swelling[139].

The timing of setting is critical. Calorimetry results show that chemical-shrinkage dominates from the silicate acceleration peak until just before the aluminate–sulfate peak, after which early-age swelling begins. Figure 5.4 indicates that MSWI BA extends the final setting time but does not extend the dormant period. As a result, mixtures with BA tend to reach final set closer to, or within, the swelling stage. Autogenous-shrinkage recording therefore starts without the initial burst of chemical-shrinkage accumulation, and the early positive deformation offsets part of the subsequent shrinkage. This timing effect explains the lower 7-day autogenous-shrinkage magnitudes in BA-only blends and supports the mitigating role of MSWI BA.

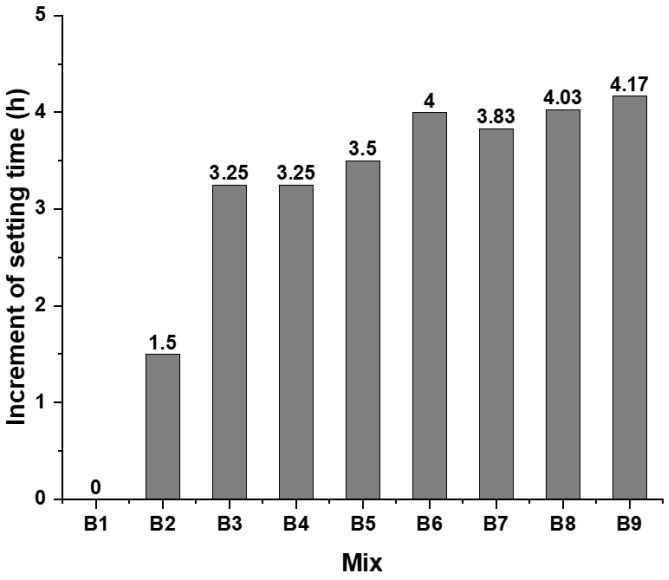

Figure 5.4. Increment of setting time (compared with B1, mix design refers to Table 3.4).

In contrast, BFA not only extends the final setting time but also prolongs the dormant period, and the dormancy extension can be comparable to or greater than the set delay. The stronger retardation observed in the BFA mixtures can be linked to the specific chemistry of BFA. As shown in Table 3.1, BFA contains a more Ca-rich amorphous phase than MSWI BA and much higher contents of alkalis, P_2O_5, SO_3, Cl and LOI than MSWI BA. When it replaces part of the clinker, these ions disturb the sulphate balance and modify the pore-solution chemistry, stabilizing the induction period and delaying the main hydration peak, so that both dormant period and setting are markedly extended. MSWI BA, in contrast, is mainly SiO_2-rich with low CaO, SO_3, P_2O_5 and LOI, so its effect is closer to a simple dilution of clinker; therefore, it causes less chemical retardation and a shorter extension of the dormant period compared with BFA at the same replacement level. Consequently, final set may still occur around the time of the first main peak, when chemical-shrinkage is dominant. The deformation record therefore begins with a rapid accumulation of autogenous shrinkage immediately after final set, leading to a larger 7-day magnitude. This timing effect is evident in the mixes rich in BFA (B3, B6, B9 in Figure 5.1), which show greater post-set shrinkage despite similar late-age decay rates.

5.4.Early-age swelling

Figure 5.5 presents the early-age swelling within the first two days after final setting. For B4 and B7, final setting occurs during the swelling stage; part of their swelling before time zero is not recorded, so their peaks are underestimated and excluded from comparison. Excluding these two mixes, all curves rise to a single peak within 24 h and decay toward zero by about two days. The peak magnitude ranks as B5 < B6 < B9 < B1 < B2 < B8 < B3 (mix design refers to Table 3.4). Relative to reference B1, the BFA-only mixes B2 and B3 show higher peaks, indicating that adding BFA increases early swelling. When BA and BFA are added together, the effect is not consistent: B5 and B6 are lower than the reference, B9 is slightly lower, while B8 is higher.

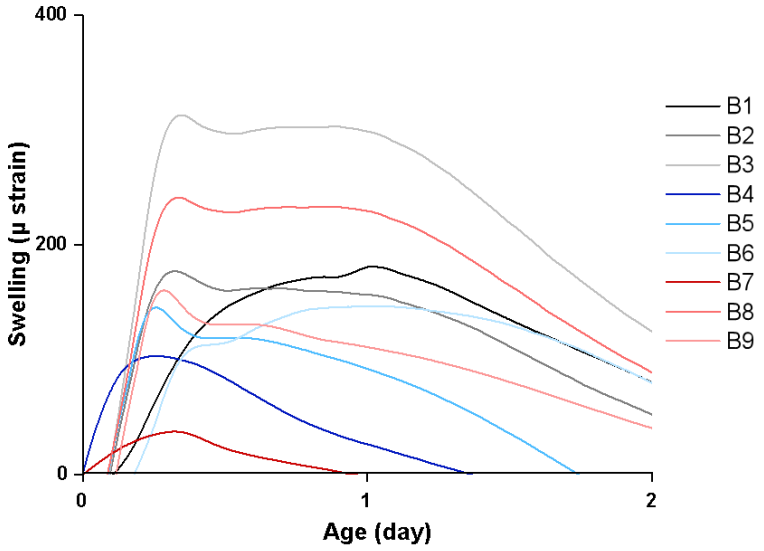

Figure 5.5 Early age swelling of 9 mixes (mix design refers to Table 3.4).

.

Figure 5.6 shows that adding BFA and MSWI BA changes the hydrate assemblage: mixes with either ash exhibit syngenite, and mixes with both ashes additionally show Friedel's salt. Syngenite ($K_2Ca(SO_4)_2 \cdot H_2O$) commonly forms at early ages in potassium/sulfate-rich pore solutions and its crystallization in confined pores has been linked to expansion of cement pastes[140], [141]. Friedel's salt ($Ca_2Al(OH)_6Cl \cdot 2H_2O$) forms by chloride binding in AFm; several studies report that its crystallization has slight effect on volume change in cement paste[142], [143].

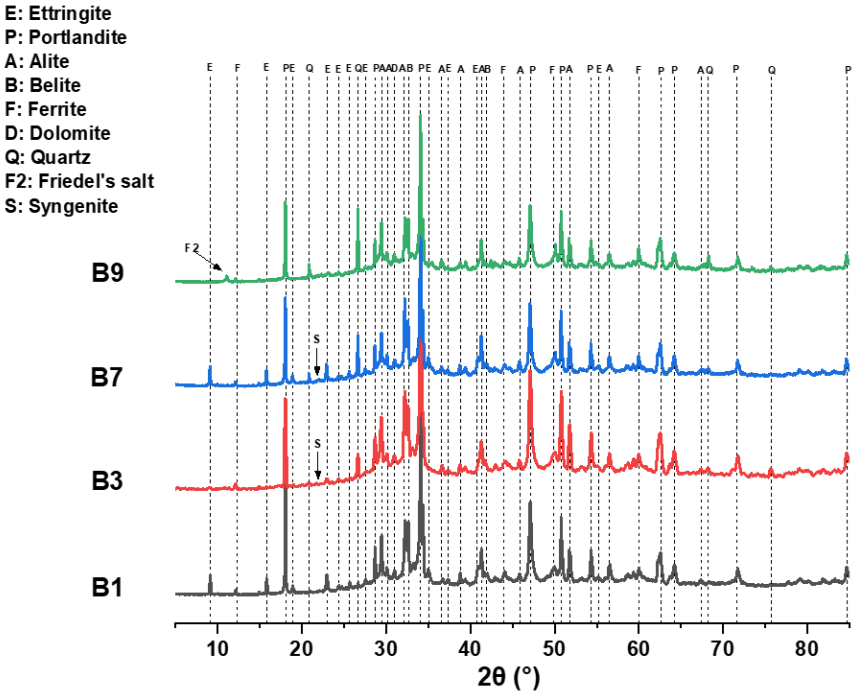

Figure 5.6. Mineralogical composition of 4 symbolic mixes (mix design refers to Table 3.4).

Based on the XRF results (see Table 3.1), both ashes supply the ionic precursors for syngenite. BFA is particularly rich in potassium and sulphate, while BA also contributes. Dissolution of these oxides raises K^+ and SO_4^{2-} in the pore solution in the presence of abundant Ca^{2+} from cement and ash CaO, so ash-bearing mixes readily precipitate Syngenite, consistent with the universal observation of syngenite when either ash is added. Formation of Friedel's salt requires chloride and AFm; the combined use of BA and BFA elevates the chloride supply and provides ample Al_2O_3 together with CaO, increasing both the chloride concentration and the availability of AFm hosts[144], [145]. In the blends containing both ashes, this chloride–AFm pathway is sufficient, and Friedel's salt appears in XRD. Because these phases draw on the same ionic pools as ettringite—calcium, Al-bearing species, sulfate and water—their formation is in competition with ettringite, and the balance among these competing precipitations governs the early expansion signature observed in the mixes[146], [147].

Table 5.1. hydration products of 9 mixes in 3 days (mix design refers to Table 3.4).

	B1	B2	B3	B4	B5	B6	B7	B8	B9
					(wt%)				
Alite	25.1	23.1	23.2	19.0	22.0	20.1	21.2	21.2	19.7
Belite	7.0	5.1	6.2	7.0	4.9	6.2	5.4	4.9	4.5
Ferrite	12.3	12.9	7.7	8.0	8.9	8.1	8.6	8.1	8.2
Portlandite	18.1	16.2	12.9	12.9	13.7	12.8	14.4	16.1	16.1
Quartz	-	2.3	3.3	5.4	7.3	7.7	7.7	9.8	11.3
Hematite	1.2	1.1	1.1	0.8	1.3	1.0	1.0	0.7	1.2
Dolomite	-	1.2	4.5	2.3	1.7	1.6	1.2	1.1	-
Akermanite	-	-	-	2.4	3.3	3.4	1.2	-	-
Ettringite	8.4	5.8	4.4	5.7	0.6	0.5	7.7	1.5	0.6
Syngenite	-	2.2	6.0	3.1	2.7	2.6	1.5	2.3	1.4
Friedel's salt	-	-	-	-	0.4	1.0	-	2.5	3.5
Amorphous	28.0	29.7	30.6	31.5	33.3	35.2	30.2	31.9	33.8

Calorimetry results (see Figure 5.2 and Figure 5.3) shows that reaction rates level off after day 3, indicating that the interval in which crystallization dominantly drives volumetric change is concentrated within the first three days. Consistent with this window, the 3-day QXRD result evidence the largest

amounts of ettringite and syngenite in B3, matching its highest early-age swelling. B2 forms amounts of ettringite and syngenite comparable to B1, and its swelling is likewise similar to the reference. When BA and BFA are combined, both ettringite and syngenite decrease markedly while Friedel's salt becomes the prevailing new phase; the volume change therefore remains close to B1 with only modest deviations around it. These observations reflect a redistribution among ettringite, syngenite, and Friedel's salt that compete for overlapping ionic reservoirs, shaping the magnitude of early expansion captured within the first three days.

5.5.Shrinkage after swelling

Figure 5.7 shows shrinkage after swelling of all mixes when consider BFA dosage as variable, mixtures containing BFA show consistently greater shrinkage after swelling: their curves lie distinctly below the non-BFA systems more dosage of BFA lead to more shrinkage.

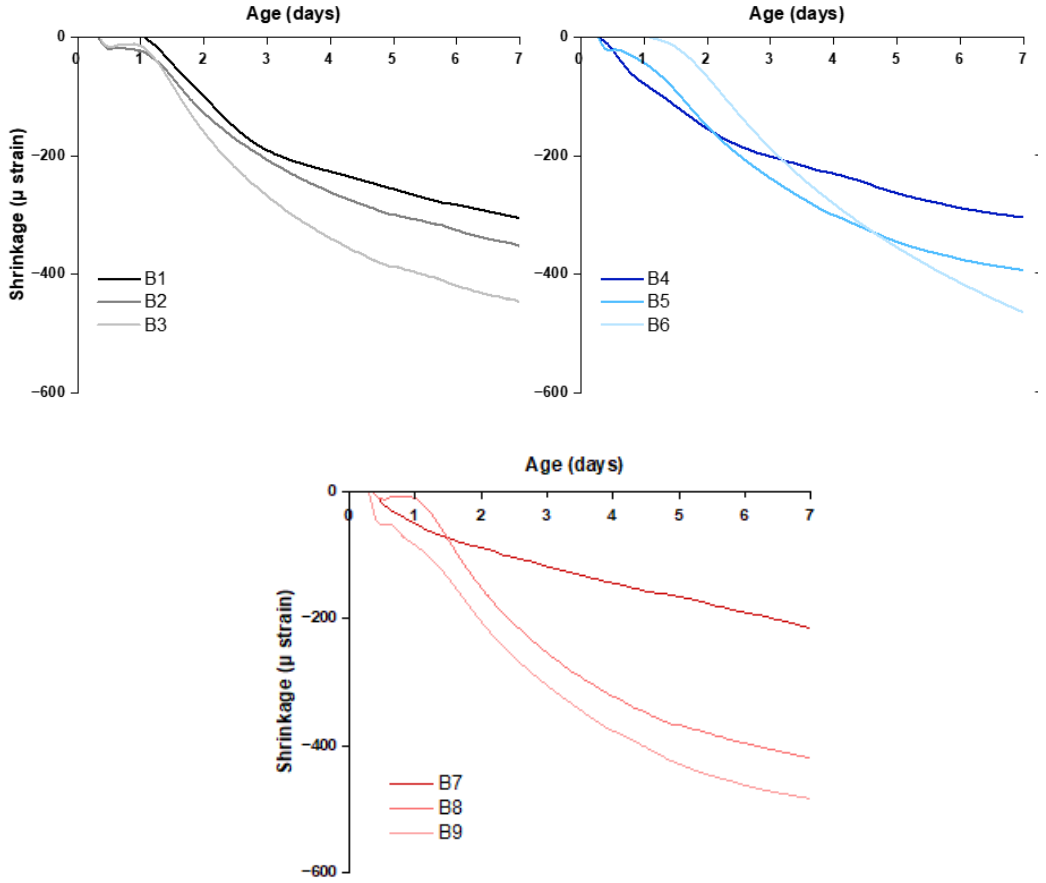

Figure 5.7 Shrinkage after swelling (BFA as variable, mix design refers to Table 3.4)

Figure 5.8 shows shrinkage after swelling of all mixes when consider MSWI BA dosage as variable, MSWI BA alone moderates the post-swelling shrinkage, with curves remaining close to or only slightly below B1. In blended BFA+MSWI BA systems, increasing the BA proportion shifts the response toward greater shrinkage; however, the increment due to additional MSWI BA is modest and remains smaller than the increase produced by adding BFA.

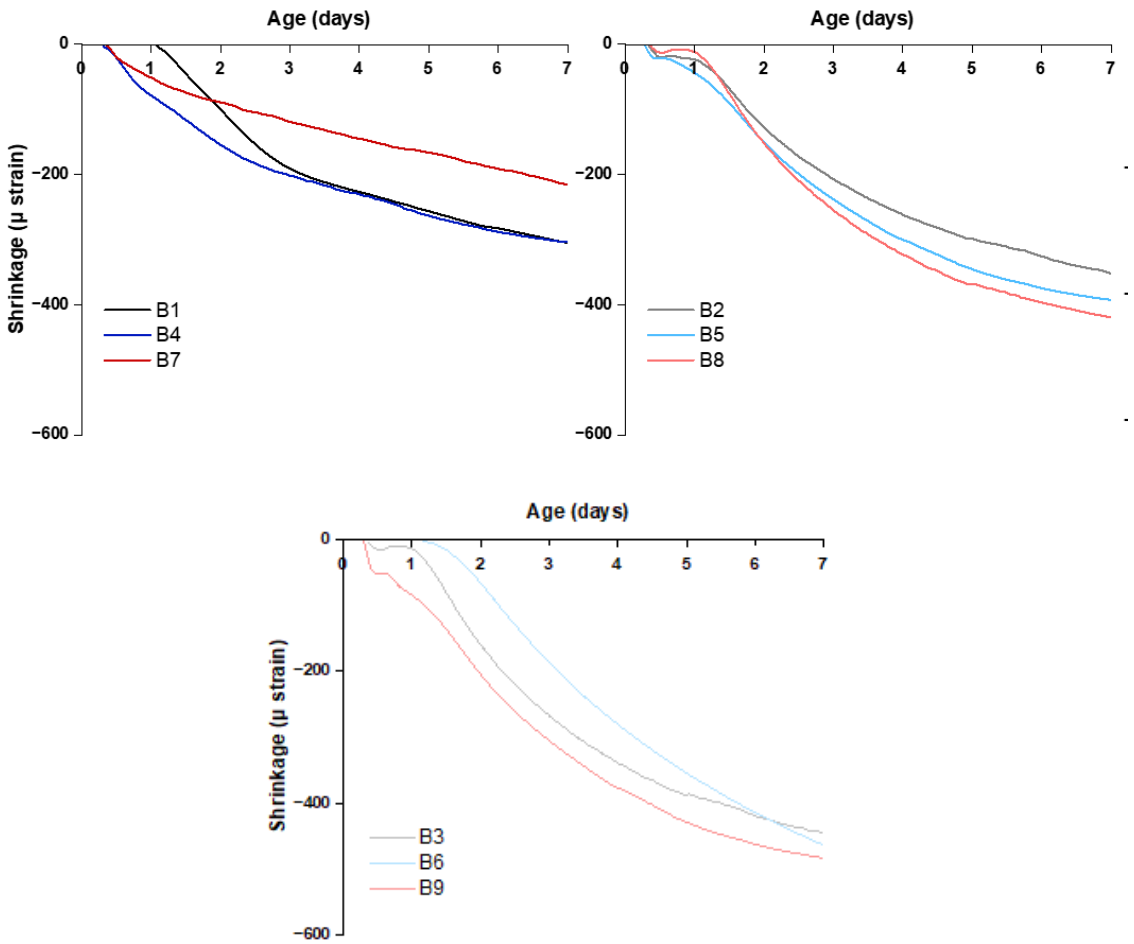

Figure 5.8 Shrinkage after swelling of 9 mixes (MSWI BA as variable, mix design refers to Table 3.4)

During this interval, hydration continues, the post-swelling trajectories are governed jointly by the elastic modulus, the capillary tension, and the swelling caused by reaction products formed during this period, which together control the magnitude of the observed shrinkage.

Figure 5.9 shows that at 7 days, all mixtures exhibit a reduced elastic modulus relative to B1. The decrease is most pronounced in BFA-blended mixes, whereas BA-blended mixes show a smaller reduction. This trend is consistent with the previously reported 7-day strength results (Figure 4.5) and aligns with calorimetry (Figure 5.2 and Figure 5.3), which indicated lower early reactivity for BFA than for MSWI BA.

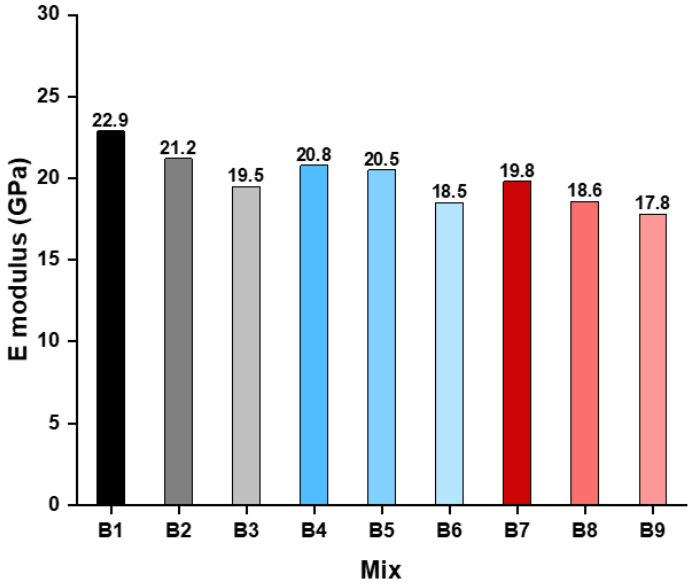

Figure 5.9 E-modulus results at 7 days（mix design refers to Table 3.4).

The degree of hydration was estimated from the cumulative heat curves obtained by isothermal calorimetry; the detailed calculation procedure is provided in Appendix A. Figure 5.10 shows that at 7 days all ash-blended mixtures reach a lower degree of hydration than the reference (B1), with the decrease being largest for BFA blended mixes and BFA+MSWI BA blended mixes (B2, B3, B5, B6, B8, B9) and smaller for only BA added mixes (B4, B7). Under identical w/b, a higher degree of hydration drives lower internal relative humidity and thus higher capillary tension; consequently, the reduced hydration in ash-bearing systems implies a higher internal RH and therefore lower capillary tension relative to the reference, with the strongest reduction occurring in the BFA mixes[148].

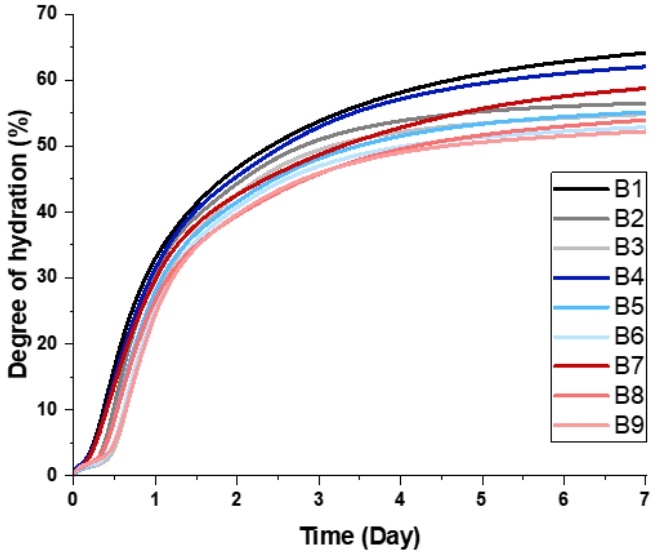

Figure 5.10. Degree of hydration at 7 days (mix design refers to Table 3.4).

Taken together, the results indicate three consistent patterns. First, BFA amplifies shrinkage after swelling because BFA-bearing mixes show the largest

7-day loss of elastic modulus; the pronounced stiffness reduction dominates the response and converts the internal stresses during this interval into greater shrinkage. In this study, the BFA-blended pastes exhibit the largest autogenous shrinkage among all mixtures. From a practical point of view, such an increase in autogenous shrinkage implies a higher risk of early-age cracking and loss of volume stability when BFA is used at high replacement levels, especially in restrained or low w/b structures. Second, MSWI BA also increases shrinkage after swelling but to a smaller extent than BFA (Figure 5.5): although degree of hydration at 7 days is higher than BFA-blended mixes, the accompanying decrease in E-modulus is lower, so the shrinkage is less amplified (Figure 5.2 and Figure 5.9); moreover, prior phase analysis shows that systems with only one type of ash tend to form more syngenite/ettringite in the early age (Table 5.1), which provides partial compensating expansion[146], [147]. Third, when BFA and MSWI BA are used together the shrinkage is amplified because its reduction on E-modulus is higher (Figure 5.9), and the concurrent formation of friedel's salt further supress the formation of ettringite/syngenite which can partially offset the shrinkage (Table 5.1); altogether, BFA-MSWI BA combined blended mixes remain higher shrinkage after swelling to B1 and clearly higher than the shrinkage induced by BFA.

5.6.Conclusion

- For BFA, when final setting occurs during the chemical-shrinkage-dominated stage, the paste immediately begins accumulating early contraction because of its and delayed dormant period. The ensuing swelling peak remains high, since the expansive hydrates such as ettringite and syngenite is formed. After the swelling, the system rapidly enters the post-swelling shrinkage phase, where the markedly reduced E-modulus amplifies the effect of capillary tension. As a result, BFA-rich mixes display the largest total autogenous shrinkage among all groups.
- For MSWI BA, the delay of final setting restricts the accumulation of shrinkage after final setting. A distinct swelling peak is typically observed, driven by the early precipitation of ettringite and syngenite that temporarily offset shrinkage. Once the swelling subsides, post-peak shrinkage remains moderate: although MSWI BA slightly lowers hydration degree, its E-modulus reduction is limited, which lessens the stiffness-related shrinkage amplification. Consequently, MSWI BA–only mixes exhibit the smallest overall autogenous shrinkage within the 0–7 day period.
- For blended BFA + MSWI BA systems, the shrinkage after final setting is because the presence of BFA delays dormant period. The swelling peak, however, becomes weaker than in single-ash systems, as the hydrate assemblage shifts from ettringite/syngenite toward Friedel's salt, which provides little volumetric compensation. During the post-swelling stage, the combined ashes lower stiffness and formation of expansive mineralogical component, yielding a larger shrinkage response.

6. Drying Shrinkage

6.1.Introduction

In this chapter, drying shrinkage after 28-day curing under controlled exposure is quantified, and its evolution across mixtures is analyzed in relation to microstructural parameters (MIP-based pore size distribution—especially the 10–50 nm range—and total porosity) and elastic modulus. Drying shrinkage is a critical durability concern because it can lead to surface cracking, loss of watertightness, and reduction of long-term stiffness, ultimately shortening the service life of cementitious materials[73], [149]. The roles of BFA and MSWI BA, individually and in combination, are evaluated to clarify how pore structure refinement and stiffness reduction influence capillary tension and deformation, and to provide guidance for designing more dimensionally stable blends.

6.2.Results of drying shrinkage

Figure 6.1 shows the drying-shrinkage evolution of the nine mixes after 28 days of curing and subsequent exposure. All curves exhibit an increase in shrinkage: a rapid initial stage over roughly the first 0–3 days, followed by a markedly slower phase that proceeds nearly linearly toward the end of the observation period (≈28–35 days), with no rebound. Early-age magnitudes are broadly similar across mixes, while differences gradually emerge after about 7–14 days.

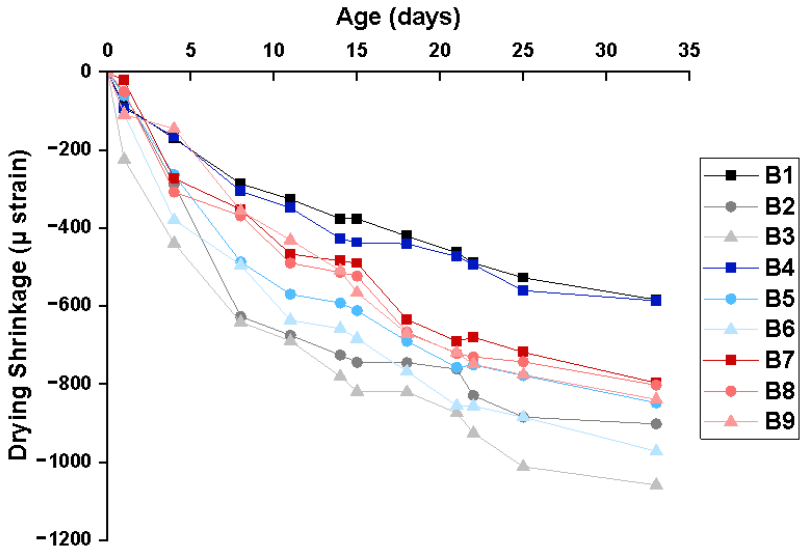

Figure 6.1 Drying shrinkage results(mix design refers to Table 3.4).

Figure 6.2 isolates the effect of BFA dosage under three MSWI BA backgrounds (0%, 10%, 20%). In all cases, increasing BFA from 0% to 5% and 10% produces a graded rise in drying-shrinkage magnitude, with separations that emerge after the early rapid stage and persist through the record. Raising the MSWI BA background shifts the entire set of curves downward—indicating lower shrinkage at a given age and simultaneously compresses the gap

between the 5% and 10% BFA lines. Thus, MSWI BA mitigates the BFA-induced increase: within each MSWI BA level the ordering remains 10% BFA > 5% BFA > 0% BFA, but the absolute differences are smaller at 20% MSWI BA than at 10% MSWI BA and smallest relative to the no- MSWI BA case. The relatively high standard deviations in Figures 6.2 and 6.3 are mainly related to the limited precision of the shrinkage measurement setup. Drying shrinkage involves very small length changes, so the finite resolution and stability of the displacement device (zeroing, alignment, drift) can introduce noticeable scatter between nominally identical specimens. Thus, the high STD indicates some uncertainty in the absolute values, but the consistent trends between mixtures suggest that the method is still reliable for comparative purposes in this study.

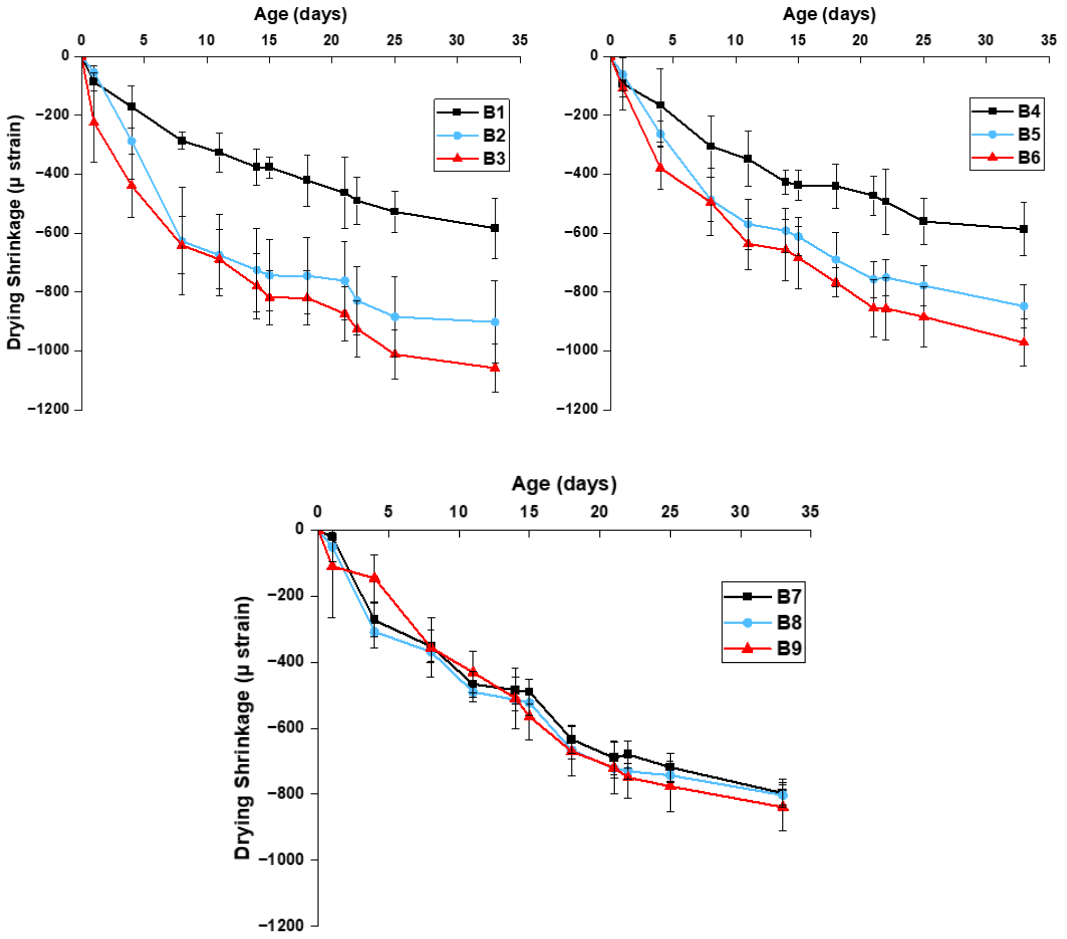

Figure 6.2. Drying shrinkage results (BFA dosage as variable, mix design refers to Table 3.4).

Figure 6.3 isolates the role of MSWI BA with the sign convention that more negative strain denotes larger shrinkage. When BA is added alone, the curves shift downward relative to B1, indicating greater drying shrinkage; the separation emerges after the initial rapid stage (≈7–14 d) and persists thereafter. In contrast, under a fixed BFA background, increasing BA from 0% → 10% → 20% shifts the curves upward, i.e., mitigates shrinkage and compresses the spread between the 5% and 10% BFA levels, indicating that MSWI BA could mitigate the drying shrinkage caused by BFA.

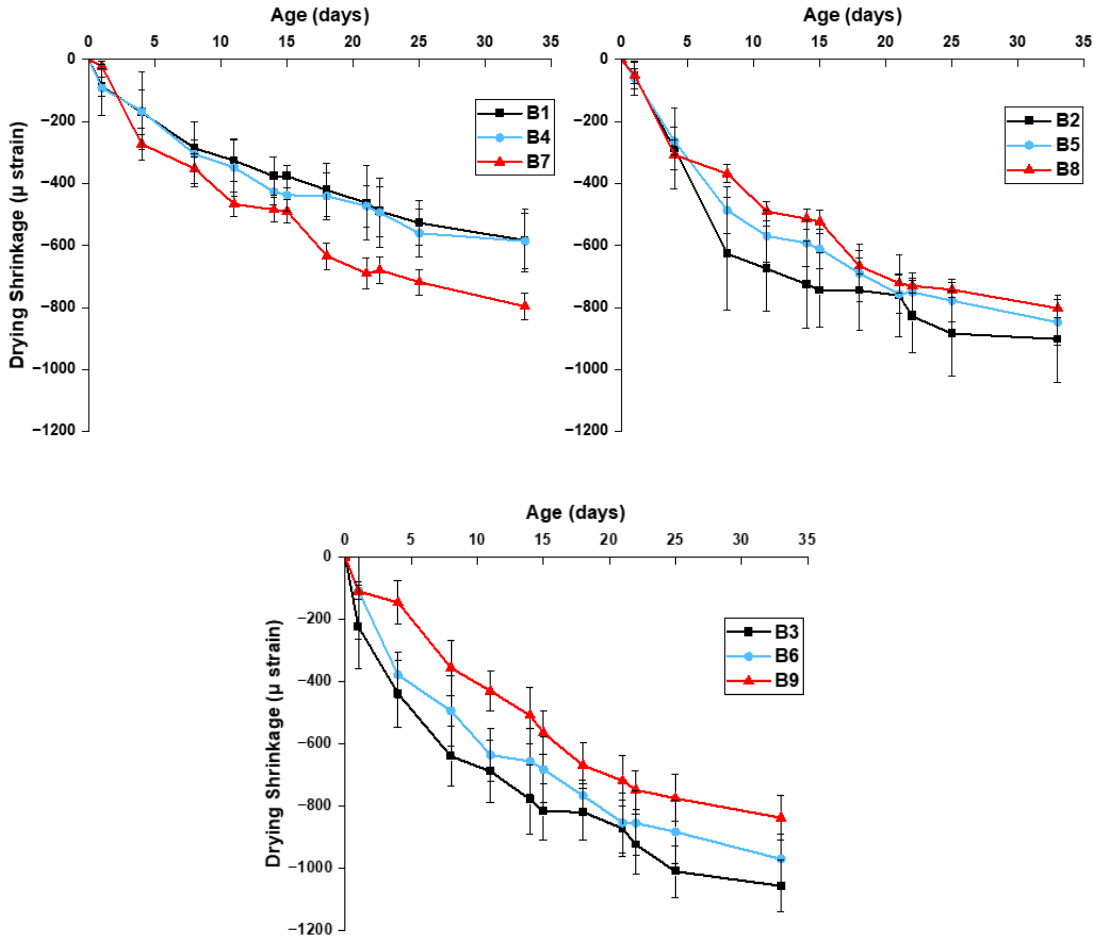

Figure 6.3. Drying shrinkage results (MSWI BA dosage as variable, mix design refers to Table 3.4).

Here the analysis proceeds along two coupled axes: stiffness and capillary-tension driving stress[149]. After 28 days of curing, mixes exhibit comparable degrees of reaction; hence the internal relative humidity (RH) during subsequent drying can be assumed similar across mixes. Under comparable RH, the Kelvin–Laplace framework links pore size to capillary pressure and thus to shrinkage. The Kelvin relation between RH and the meniscus (Kelvin) radius $r_K$is

$$r_K = -\frac{2\gamma V_m cos\theta}{RTln(RH)}$$

where $\gamma$is the surface tension of water, V_m is the molar volume, $\theta$is the contact angle, $R$is the gas constant, and $T$is absolute temperature. The associated capillary pressure is then

$$p_c = \frac{2\gamma cos\theta}{r_K}$$

Thus, for the same RH, mixtures with finer, more connected pores (smaller r_K) develop higher capillary pressure and a larger driving force for shrinkage. The effective drying strain subsequently depends on the elastic modulus: higher

emodulus reduces strain for a given p_c, whereas a more compliant skeleton amplifies it. In what follows, differences in shrinkage among mixes are interpreted by combining (i) stiffness contrasts from elastic modulus and (ii) pore-scale control of capillary tension inferred from MIP test

6.3.E-modulus of paste at 28 days

Figure 6.4 shows that at 28 days, the elastic modulus remains lower when a greater proportion of ash is incorporated, consistent with the trend observed at early age; however, the between-mix separations are appreciably smaller than at 7 days. This attenuation of differences indicates ongoing, longer-term reactions of both BFA and MSWI BA that partially recover stiffness with time. Given the narrowed spread in E-modulus at 28 days, skeletal stiffness is unlikely to be the primary driver of the observed divergence in drying shrinkage among mixes. Instead, the results point to capillary-tension effects—governed by pore-structure characteristics—as the dominant contributor to the shrinkage differences.

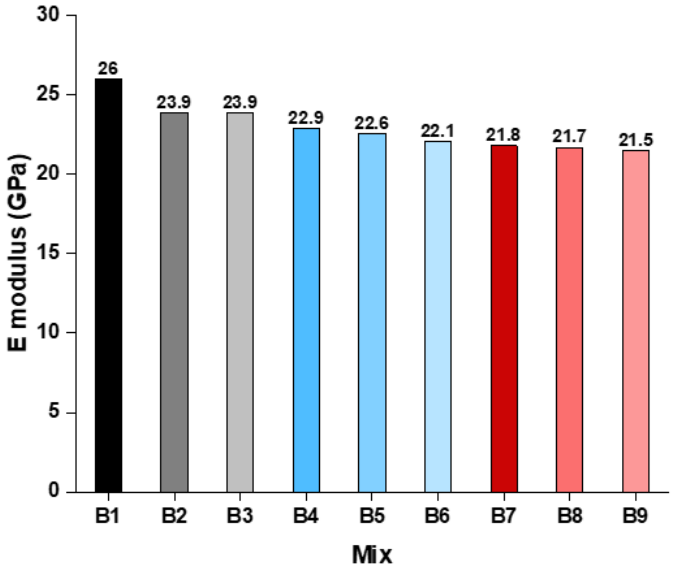

Figure 6.4. E-modulus results of 9 mixes at 28 days (mix design refers to Table 3.4).

6.4.Pore structure of paste at 28 days

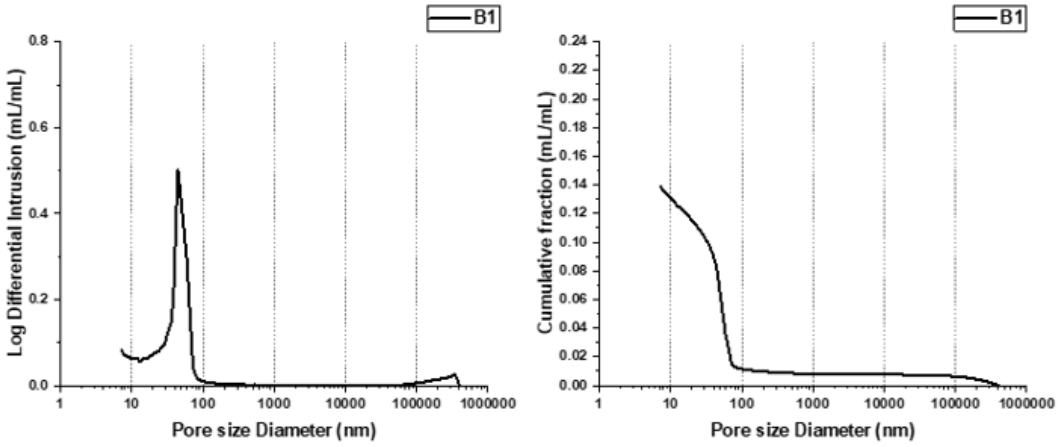

Figure 6.5-Figure 6.13 shows the differential and cumulative pore size distribution (PSD) curve of 9 different mixes. From the differential PSD curves, all mixes exhibit a single dominant peak within the 10–50 nm medium capillary pores band, defining a common critical pore width and indicating that pore sizes are largely concentrated in this range. The broadly similar peak shapes imply that, by 28 days, adding BFA or MSWI BA does not fundamentally alter the qualitative form of the pore-size distribution; rather, the main differences are incremental and will be detailed in the following sections. In contrast, the cumulative curves clearly shift upward with increasing total ash content, showing a higher total porosity at 28 days. This trend is consistent with a lower effective degree of hydration for both ashes and corroborates the calorimetry evidence of reduced reactivity.

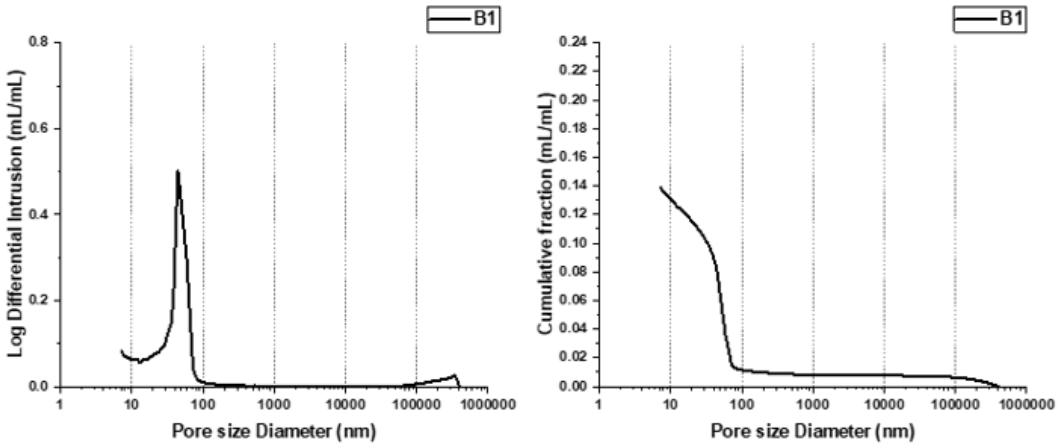

Figure 6.5 Differential and cumulative PSD curve of B1 (100% CEM I) at 28 days.

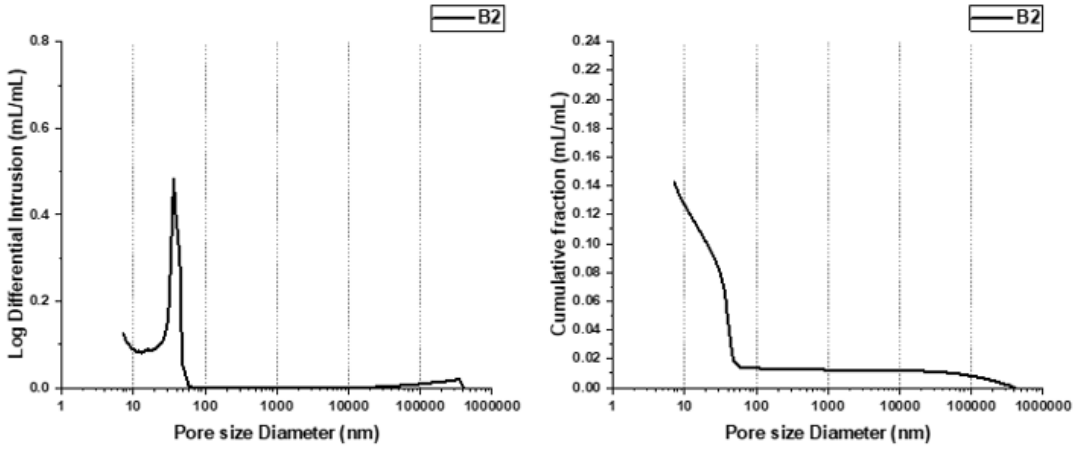

Figure 6.6 Differential and cumulative PSD curve of B2 (95% CEM I, 5% BFA) at 28 days.

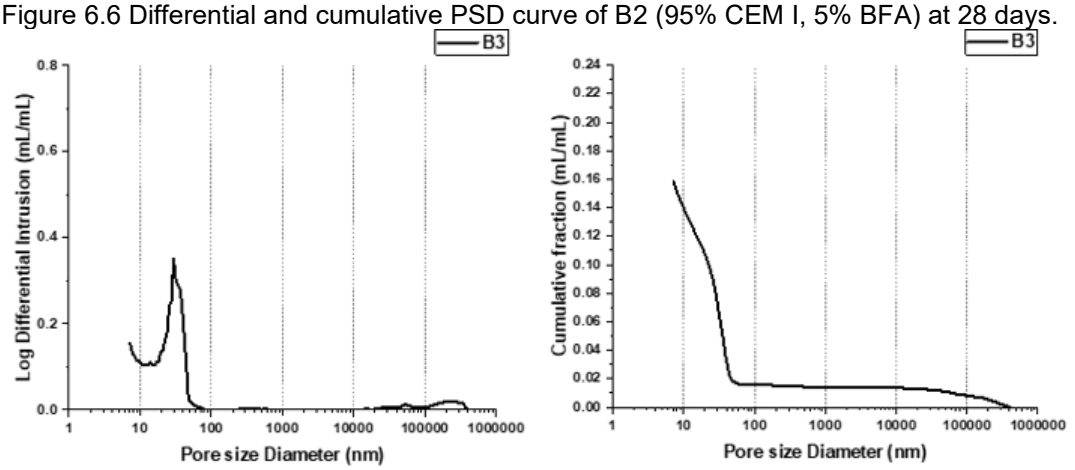

Figure 6.7Differential and cumulative PSD curve of B3 (90% CEM I, 10% BFA) at 28 days.

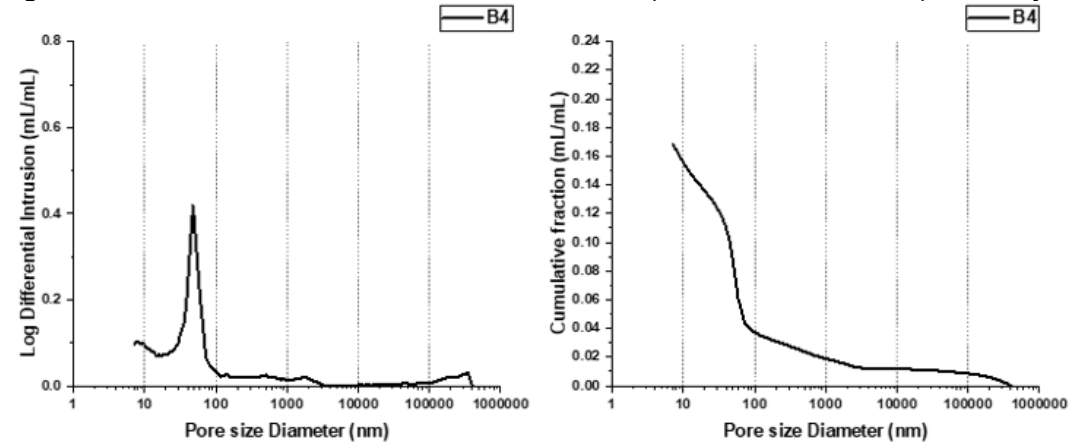

Figure 6.8 Differential and cumulative PSD curve of B4 (90% CEM I, 10% MSWI BA) at 28 days.

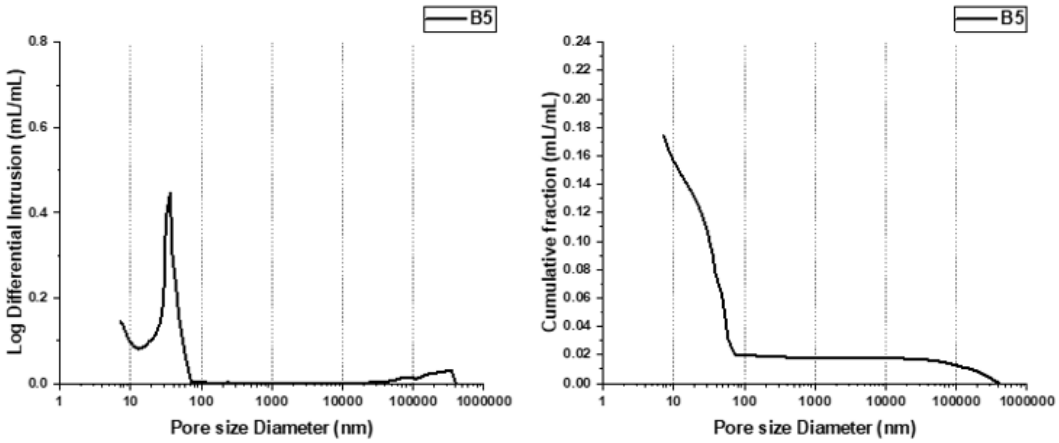

Figure 6.9 Differential and cumulative PSD curve of B5 (85% CEM I, 5% BFA, 10% MSWI BA) at 28 days.

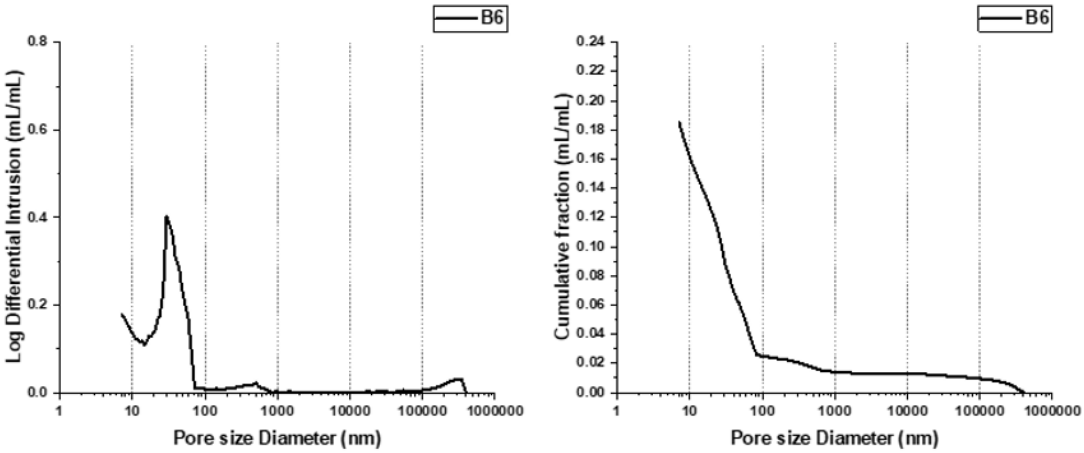

Figure 6.10 Differential and cumulative PSD curve of B6 (85% CEM I, 5% BFA, 10% MSWI BA) at 28 days.

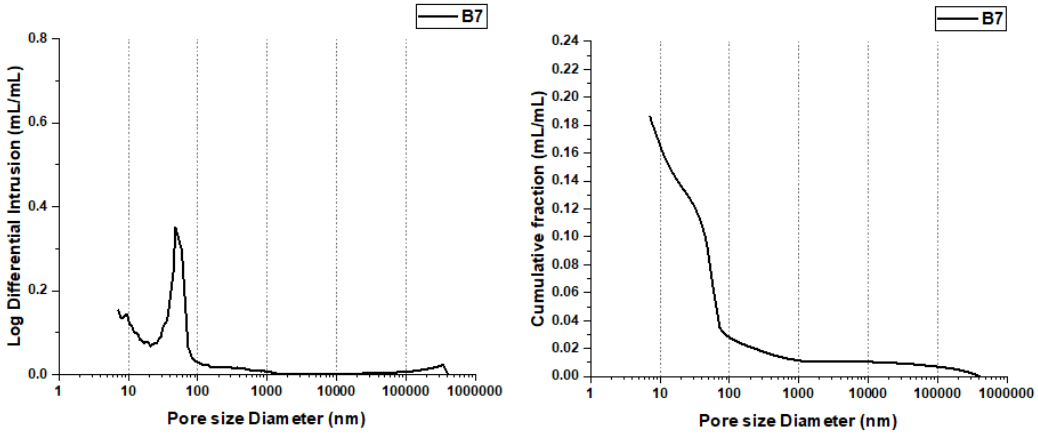

Figure 6.11 Differential and cumulative PSD curve of B7 (80% CEM I, 20% MSWI BA) at 28 days.

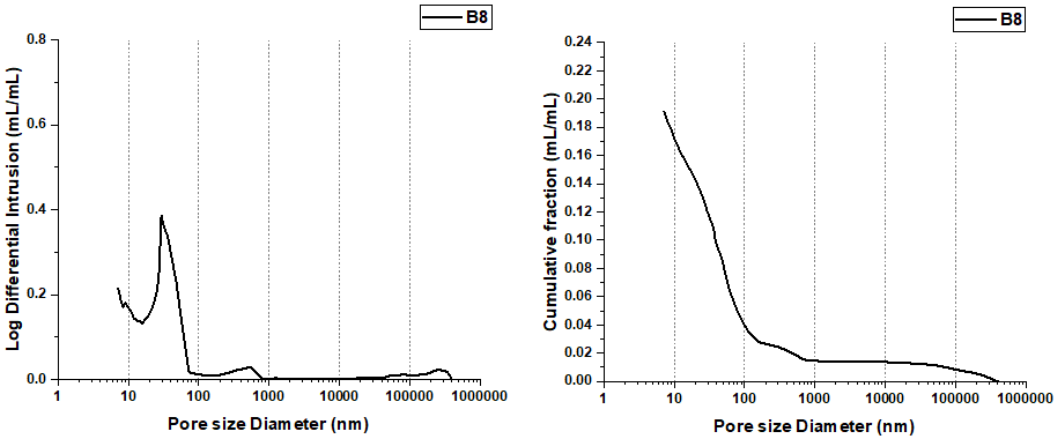

Figure 6.12 Differential and cumulative PSD curve of B8 (75% CEM I, 5% BFA, 20% MSWI BA) at 28 days.

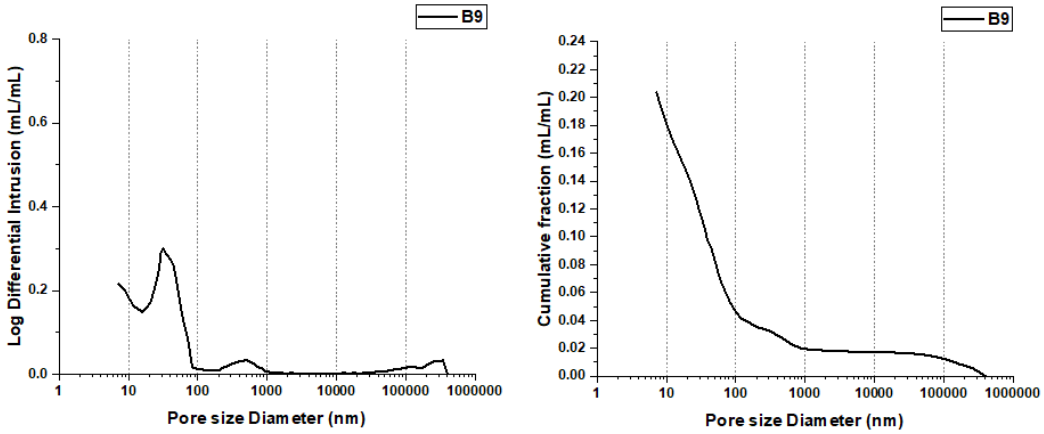

Figure 6.13 Differential and cumulative PSD curve of B9 (70% CEM I,10% BFA, 20% MSWI BA) at 28 days.

From the differential PSD, a critical pore width can be extracted for each mix (Figure 6.14). The critical pore width is defined as the pore size corresponding to the peak of the differential mercury-intrusion pore-size distribution curve, which represents the dominant, transport-governing capillary pores in the network[150]. A smaller critical width indicates a denser pore structure, whereas a larger value reflects coarser pores. The bar chart shows a clear trend: increasing BFA content markedly reduces the critical pore width, evidencing pore refinement. In contrast, adding MSWI BA increases the critical pore width, i.e., coarsens the pore system. In co-blended mixes, BA partially counteracts the BFA-induced refinement, shifting the critical width upward relative to the BFA-only case.

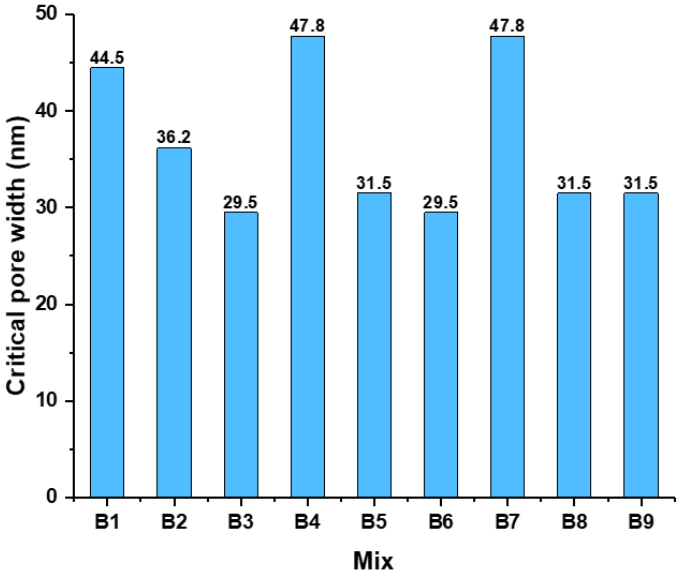

Figure 6.14 Critical pore width at 28 days (mix design refers to Table 3.4).

Figure 6.15 summarizes the 28-day total porosity for all mixes. A clear monotonic increase is observed from B1 to B9, indicating that higher ash contents yield higher porosity at 28 days. BA raises total porosity more strongly than BFA at comparable backgrounds, and the co-blended mixes (with both BFA and BA) reach the highest values. This trend is consistent with a lower effective degree of hydration and aligns with the larger drying-shrinkage magnitudes observed for mixes with greater ash replacement.

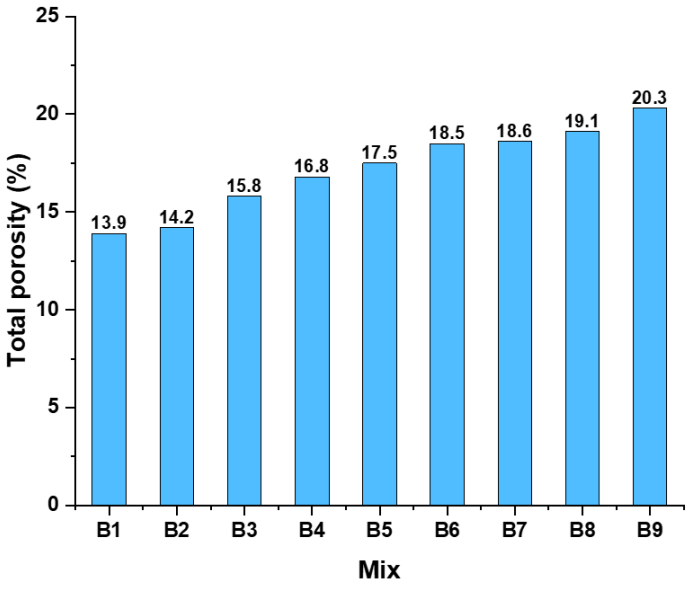

Figure 6.15. Total porosity at 28 days (mix design refers to Table 3.4).

Figure 6.16 partitions total porosity into gel, medium-capillary, and large-capillary fractions. Increasing the overall ash content systematically raises the gel-pore fraction, indicating greater very-fine porosity at 28 days. At a fixed BA background, adding BFA shifts capillary porosity toward the medium-capillary band and reduces the share of large-capillary pores, consistent with pore refinement (smaller critical width). Conversely, at a fixed BFA background,

increasing MSWI BA enlarges the proportion of large-capillary pores within the capillary domain, i.e., it coarsens the capillary network despite the concurrent rise in gel pores. These opposing trends align with earlier observations that BFA refine while BA coarsens the capillary pore system.

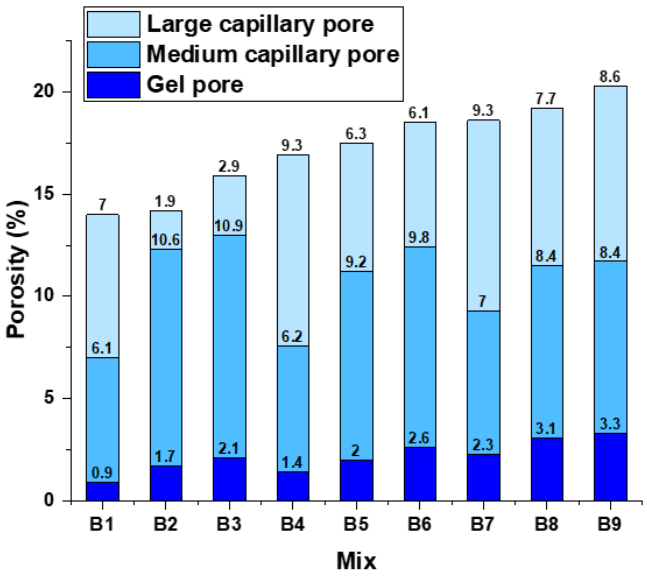

Figure 6.16 Composition of pores at 28 days (mix design refers to Table 3.4).

BFA leads to a denser pore structure primarily through filler–seeding and geometric effects. Its porous, rough, high–surface-area particles provide abundant heterogeneous nucleation sites for C–(A)–S–H, promoting finely dispersed hydrate precipitation within narrow interparticle gaps and around ash rims; this preferential deposition constricts pore throats and shifts the pore-size distribution toward smaller critical width[151]. In parallel, the fine BFA fractions act as fillers that occupy interstitial voids between cement grains, increasing packing density and thereby reducing characteristic capillary widths even before extensive later-age product growth. Studies demonstrate that other SCMs like fine limestone and silica additions provide extra surfaces that promote C-S-H formation [152], indicating that BFA could have same effect. The combined outcome is a refined capillary network—smaller throats and a higher fraction of mesopores—consistent with the observed decrease in critical pore width.

MSWI BA likely exerts a similar filler–seeding effect, as reflected by the higher gel-pore fraction—indicating some pore-scale densification at 28 days. However, even with pre-treatment, metallic Al in BA cannot be fully removed; during hydration in alkaline pore solution it reacts and releases H_2, perturbing the developing microstructure[153]. This gas evolution promotes coarsening within the capillary domain, which is consistent with the PSD evidence that BA addition markedly increases the share of large capillary pores[154]. The resulting dual action—more gel pores but a higher proportion of large capillaries—explains why BA alone can shift the capillary spectrum toward larger sizes.

The 10–50 nm medium-capillary pores are the most influential for capillary-

tension–driven drying shrinkage under typical service RH. By Kelvin–Laplace theory, at 40–70% RH these pores host curved menisci with large radius, generating high capillary pressures; larger capillary pores (>50 nm) empty earlier at higher RH and contribute less to stress thereafter, while gel pores (<10 nm) largely remain saturated down to ≈50% RH and thus play a minor direct role in capillary tension[155], [156]. Consequently, mixtures with a higher fraction of 10–50 nm pores exhibit greater shrinkage, and reducing the volume of pores in this band demonstrably lowers shrinkage.

Overall, BFA drives the paste toward a finer pore structure, which raises capillary tension. The combination of higher capillary stress and lower stiffness therefore amplifies drying shrinkage in BFA-only blended mixes. In contrast, when MSWI BA is used alone, the medium capillary pore fraction remains broadly comparable to the reference, but the elastic modulus decreases, yielding larger shrinkage primarily through reduced stiffness. When co-blended with BFA, MSWI BA reduces the proportion of medium capillary pores and shifts the capillary domain toward coarser pores, which lowers capillary tension; under these co-blend conditions, the stiffness differences are relatively small compared with the pore-size effect. Consequently, MSWI BA moderates the BFA-induced increase in drying shrinkage by offsetting capillary-tension build-up, even though its direct effect on stiffness is limited.

6.5.Conclusion

In this chapter, drying shrinkage after 28-day curing was quantified and linked to pore structure and stiffness using shrinkage curves, MIP-derived PSDs, and elastic modulus to identify the dominant mechanisms.

- All mixes exhibit monotonic drying shrinkage: a rapid early stage followed by a slower, near-linear stage; differences become clear after ~7–14 days.
- At 28 days, stiffness differences are modest; pore-structure–controlled capillary tension is the primary driver of between-mix shrinkage differences.
- BFA increases total porosity but refines the capillary network (smaller critical pore width; higher 10–50 nm share), raising capillary tension; together with a lower elastic modulus, this yields larger shrinkage.
- MSWI BA used alone keeps the medium-capillary fraction similar to the reference but lowers elastic modulus, leading to greater shrinkage mainly via increased compliance.
- In co-blends, MSWI BA shifts pores toward larger capillaries and reduces the medium-capillary fraction, lowering capillary tension; with similar stiffness across mixes, BA moderates the BFA-induced shrinkage increase.

7. Conclusion and Recommendations

7.1. Result overview

The main findings of the research are summarized in Table 7.1

Table 7.1. Summary of results.

Fresh Properties	
Workability(flowability/slump)	At constant $w/c = 0.35$, replacing cement with BFA and MSWI BA reduced slump and flowability. The loss followed BFA > MSWI BA. Compared to BFA, MSWI BA-blends preserved workability best at the same total replacement level.
Setting time	Both MSWI BA and BFA delayed initial and final set, with BFA causing the longer delay. MSWI BA produced shorter delays than BFA.
Mechanical Properties	
Compressive and flexural strength	Relative to CEM I paste, both strengths decreased with ash replacement, the loss ranked BFA > BFA+MSWI BA > MSWI BA at all ages. Flexural strength followed the same order as compressive strength. The low reactivity drives the loss; MSWI BA is low-reactive but offers a filler effect that limits the penalty, whereas BFA is even less reactive and more porous, increasing water demand and gel-porosity and thus reducing matrix stiffness and strength.
E-modulus	The overall trend mirrors strength: at equal replacement and age, MSWI BA ≥ BA+BFA > BFA. At 7 d, BA-only mixes show the closest to the reference, indicating higher early reactivity than BFA. MSWI BA is more reactive than BFA at 7 d, while BFA partially catches up by 28 d but remains below BA.
Shrinkage	

Autogenous Shrinkage	Across all mixes the net autogenous strain ranked BFA > BFA+BA > MSWI BA. BA-only pastes show the lowest 0–7 d shrinkage, whereas BFA-only pastes exhibited the highest shrinkage; BFA-MSWI BA combined blended mixes were intermediate. Hydrate assemblage explains the compensation: BA promotes ettringite/syngenite formation that offsets part of the strain, while BFA+MSIW BA shifts toward Friedel's salt, offering less offset than ettringite and syngenite. After the peak, shrinkage scales with stiffness loss—mixes with a lower E-modulus exhibits more shrinkage. Although ash addition causes higher 7-day internal RH, this effect is outweighed by the stiffness penalty: BFA causes the largest modulus to drop and thus the largest post-peak shrinkage; MSWI BA causes only a modest modulus decrease and therefore the smallest post-peak shrinkage; BFA+MSWI BA blended mixes lie between these bounds.
Drying shrinkage	All mixes show drying shrinkage with a rapid early stage followed by a slower near-linear stage; differences become evident after ~7–14 days. By 28 d, stiffness differences are modest, capillary tension is the main driver of between-mix differences. BFA increases total porosity and refines the capillary network, which raises capillary tension; combined with its lower elastic modulus this yields the largest shrinkage. MSWI BA blended mixes keep the critical pore width close to CEM I paste but lowers stiffness, so its shrinkage increase arises mainly from higher compliance. In BFA+MSWI BA blended mixes, MSWI BA shifts pores toward larger capillaries and reduces the medium-capillary fraction, lowering capillary tension; with similar stiffness across mixes, BA moderates the BFA-induced increase in drying shrinkage.

7.2.Conclusion of the research

In this research, the research questions below can be answered:

What is the impact of adding BFA and MSWI BA on cement paste's performance?

Adding BFA or MSWI BA reduces flowability and delays both initial and final set, with the magnitude BFA > BFA+MSWI BA > MSWI BA; at 5% the change is small, and at 15–25% it is pronounced. Mechanical properties follow a consistent order: compressive/flexural strength and E-modulus decrease with replacement, ranking MSWI BA ≥ BFA+MSWI BA > BFA at comparable dosages; from 7→28 d the gain is largest for BFA, co-blends are intermediate, and MSWI BA remains highest. Regarding shrinkage, autogenous shrinkage increases when BFA is used and also increases for BFA+MSWI BA co-blends, while mixes with MSWI BA alone show a reduction relative to the reference; for

drying shrinkage, both BFA alone and MSWI BA alone increase shrinkage, whereas in co-blended mixes the presence of MSWI BA moderates the BFA-induced increase, giving intermediate levels.

How do ashes influence the Autogenous and Drying shrinkage?

Autogenous Shrinkage:

Over 0–7 days the strain history comprises three stages: deformation after final set, an early swelling window, and the post-peak shrinkage. Crucially, the timing of final set vs. the rate of chemical shrinkage controls how much early shrinkage accumulates. If final setting occurs while chemical shrinkage is still rapid, early shrinkage accumulates quickly; if final setting occurs after that rapid phase, the initial accumulation is largely avoided. Both BFA and MSWI BA delay final set, but in different ways: BFA notably extends the dormant period, so final set tends to fall during the rapid chemical-shrinkage phase → large early accumulation; MSWI BA shifts final set to after the rapid phase → little or no initial accumulation. In single-ash systems, mixes with BFA and MSWI BA show partial compensation by early formation of ettringite/syngenite, whereas BFA-MSWI BA combined mixes exhibit little effective swelling due to the formation of friedel's salt. After the peak, the shrinkage scales with stiffness loss—mixtures with a lower E-modulus shrink more. Although adding ashes lowers the 7-day DoH relative to the reference (which would raise internal RH and reduce capillary tension), this is outweighed by the stiffness effect: BFA causes the largest E-modulus drop and therefore the largest post-peak shrinkage; MSWI BA causes only a modest modulus decrease and, together with its partial swelling compensation, yields the smallest 0–7 d autogenous shrinkage. In BFA+MSWI BA co-blends, the hydrate assemblage shifts toward Friedel's salt, removing much of the swelling offset while stiffness decreases remain moderate—so totals are intermediate. Consequently, the overall ranking of 0–7 d autogenous shrinkage across mixtures is BFA > BFA+MSWI BA > MSWI BA.

Drying shrinkage:

After curing, differences are governed mainly by capillary tension vs. stiffness during moisture loss. BFA increases total porosity and the 10–50 nm pore fraction (higher capillary pressure) and reduces E-modulus, so drying shrinkage is largest when BFA is used alone. MSWI BA used alone shifts pores toward larger capillaries and keeps the medium-capillary fraction closer to the reference, so drying shrinkage is smaller than with BFA at equal dosage. In BFA+MSWI BA mixes, the presence of metallic aluminum in MSWI BA moderates the BFA-induced pore refinement, yielding intermediate drying-shrinkage levels.

How to guide mix design to minimize shrinkage?

To minimize shrinkage, use MSWI BA preferentially; if co-blending with BFA, keep MSWI BA dominant. Limit total ash ≤ 15% of binder; if 20–25% is required, cap BFA ≤ 10% of binder and supply the remainder with MSWI BA. For shrinkage-sensitive work, use 20% MSWI BA alone; if BFA must be included, keep it at 5% and pair with enough MSWI BA so that cement remains ≥ 85% of the binder.

7.3.Future Recommendations

The present study clarified how incorporating BFA and MSWI BA (alone and co-blended) influences fresh behaviour, strength and stiffness, and both autogenous and drying shrinkage of cement pastes at laboratory scale. As with any research, there remain avenues to deepen understanding and address limitations, particularly the short monitoring window, paste-level focus, and controlled curing environment. Building on these findings, future work should refine early-age characterization (chemical-shrinkage/setting window), verify cracking risk under restraint, scale the binders to mortar/concrete, and broaden environmental/age ranges. These efforts will extend the applicability of the results and provide sharper guidance for shrinkage-optimized mix design using MSWI BA and BFA.

1. **Instrument the first-week chemical shrinkage–setting interplay.**
   Track chemical shrinkage together with isothermal calorimetry, autogenous strain and in-situ setting (Vicat/ultrasound). For each MSWI BA:BFA ratio, map when the rapid chemical-shrinkage phase occurs and place final set after that phase. This window control is critical to avoid early strain accumulation and helps safeguard durability.

2. **Add restrained-shrinkage verification (cracking risk).**
   Complement paste free-shrinkage with restrained ring tests and basic creep blocks to translate the observed autogenous/drying strains into cracking propensity; use the same binder proportions to keep results comparable.

3. **Scale up from paste to mortar/concrete.**
   Validate the recommended MSWI BA–dominant blends at mortar/concrete scale (same binder fractions) and quantify how aggregates modify shrinkage, modulus and setting windows; this checks lab findings for field relevance.

4. **Broaden the lab envelope beyond 20 °C/95% RH and short ages.**
   Run parametrics in RH (30–80%) and temperature (10–35 °C) and extend monitoring to 90–180 d. Pair shrinkage with pore-structure (MIP/NMR) and dynamic modulus to create simple prediction charts linking 10–50 nm pores + composite E to autogenous and drying shrinkage.

5. **Broaden the pore structure analysis beyond 7 nm.**

   In future studies, the finer gel-pore range that cannot be reliably captured by mercury intrusion porosimetry could be characterised using low-temperature nitrogen adsorption (e.g. BET/BJH analysis), which would provide a more detailed description of pores below about 10 nm and allow a better linkage between microstructure refinement and shrinkage behaviour.

Appendix

A: Calculation of degree of hydration

The degree of hydration (DoH) at age t is obtained from calorimetry as the fraction of the potential (ultimate) heat that has been released:

$$\alpha(t) = \frac{Q(t)}{Q^{\infty}} \quad (1)$$

where $Q(t)$ is the cumulative heat of hydration measured up to t, and Q^{∞} is the ultimate heat available from the material under the test conditions. This definition is standard in hydration analyses that use isothermal calorimetry, where the cumulative heat is directly proportional to reaction progress and the ultimate heat acts as the normalization constant[157].

For blended binders (cement + ash), energy additivity gives

$$Q_{mix}(t) = \alpha_{mix}(t) Q^{\infty}_{mix} \quad (2)$$

with Q^{∞}_{mix} the ultimate heats of blended cement, and α_{mix} the corresponding DoH values. In practice, $Q(t)$ is measured by isothermal conduction calorimetry, and α follows from the ratio above.

The ultimate heat of the blended binder is the sum of the cement and ash contributions,

$$Q^{\infty}_{\text{mix}} = x_c \, Q^{\infty}_c + x_a \, Q^{\infty}_{\text{ash}} \quad (3)$$

where x_c and x_a are the cement and ash mass fractions in the binder.

To obtain the cement ultimate heat Q^{∞}_c, we estimate the cement's potential phase composition (C_3S, C_2S, C_3A, C_4AF) from bulk oxide chemistry using the Bogue method, then apply a phase-heat weighting:

$$Q^{\infty}_c = \sum_{i \in \{C_3S, C_2S, C_3A, C_4AF\}} \phi_i H_i \quad (4)$$

where ϕ_i are the Bogue-derived phase mass fractions and H_i are the heats of complete hydration for each phase. Bogue's calculation of compounds from oxide analysis is the classical basis for "potential phase composition"[158].

The ash ultimate heat is estimated by summing heats over potentially reactive phases identified by QXRD

$$Q^{\infty}_{\text{ash}} = \sum_{p \in \mathcal{R}} w_p \, H_p \quad (5)$$

where w_p is the mass fraction of phase p (including the amorphous fraction) and H_p is the heat of complete reaction of that phase (J/g of phase).
When R³ data are available, the 7-day R³ cumulative heat per kilogram of ash is used as the upper bound for ash heat at the same age in OPC. R³ places the ash in a reaction-favorable environment: (i) excess $Ca(OH)_2$ and fixed high alkalinity (pH $\gtrsim$ 13) sustain glass dissolution and pozzolanic reactions; (ii) high water availability and minimal self-desiccation limits; (iii) no competition from cement clinker for ions or nucleation sites; (iv) optional sulfate supply avoids Al-phase starvation[159], [160], [161]. Consequently, at a given temperature and

age,

$$Q_{\text{ash}}^{\text{OPC}}(t) \leq Q_{\text{ash}}^{R^3}(t)$$

Table 5.1. hydration products of 9 mixes in 3 days (mix design refers to Table 3.4).able A shows the potential heat of phases in binder. After assigning per-phase heats $H_p$and phase fractions $w_p$from QXRD, the ultimate reaction heat of each ash is obtained by Eq. (5), yielding $Q_{\text{BFA}}^{\infty}$and $Q_{\text{MSWI BA}}^{\infty}$. For each of the nine binders, the ultimate heat of the blend is then computed by Eq. (3), reported per kg binder. Once the 7-day cumulative heat curve $Q_{\text{mix}}(t)$ is measured, the degree of hydration at 7 d follows directly from Eq. (2).

Table A. Potential heat release of mineralogical composition.

#	Phase	Formula	H (J/g)	Note
1	Alite (C_3S)	$3CaO{\cdot}SiO_2$	502	Lerch & Bogue[162]
2	Belite (C_2S)	$2CaO{\cdot}SiO_2$	260	Lerch & Bogue [162]
3	Tricalcium aluminate (C_3A)	$3CaO{\cdot}Al_2O_3$	867	Lerch & Bogue [162]
4	Tetracalcium aluminoferrite (C_4AF)	$4CaO{\cdot}Al_2O_3 \cdot Fe_2O_3$	419	Lerch & Bogue [162]
5	Quartz	SiO_2	0	Stable[163]
6	Tricalcium aluminate	$Ca_3Al_2O_6$	900–1100	Taylor, Kurdowski [164]
7	Gehlenite (melilite)	$Ca_2Al(AlSi)O_7$	250–350	RILEM TRM[165]
8	Larnite	Ca_2SiO_4	250–270	Taylor, Kurdowski[164]
9	Calcite	$CaCO_3$	0	Stable [166]
10	Portlandite	$Ca(OH)_2$	0	Product phase;
11	Hydroxylapatite	$Ca_5(PO_4)_3(OH)$	0	Inert [167]
12	Iron oxide	Fe_3O_4 / Fe_2O_3	0	Inert [167]
13	Lime (free CaO)	CaO	1160	Hydration enthalpy[168]
14	Manganosite	MnO	0	inert at test scale [167]
15	Periclase	MgO	1600–2100	Hydration enthalpy[169]
16	Fluorite	CaF_2	0	Stable [167]
17	Beusite	$(Mn^{2+},Ca,Mg)_3(PO_4)_2$	0	Stable [167]
18	Rutile	TiO_2	0	Inert [167]

19	Akermanite (melilite)	$Ca_2MgSi_2O_7$	250–350	RILEM TRM [164]
20	Magnetite	Fe_3O_4	0	Inert[167]
21	Albite	$NaAlSi_3O_8$	0	Inert [167]
22	Wüstite	FeO	0	Inert [167]
23	Delta-alumina	Al_2O_3	0–300	Need to be activated [170]
24	Ferrosilite	$FeSiO_3$	0	Inert [167]
25	Gypsum	$CaSO_4 \cdot 2H_2O$	0	[162]

References

[1] M. C. G. Juenger and R. Siddique, “Recent advances in understanding the role of supplementary cementitious materials in concrete,” *Cem Concr Res*, vol. 78, pp. 71–80, Dec. 2015, doi: 10.1016/J.CEMCONRES.2015.03.018.

[2] “BOTTOM ASH FACT SHEET”, Accessed: Oct. 21, 2025. [Online]. Available: www.apeal.org

[3] E. Allegrini, A. Maresca, M. E. Olsson, M. S. Holtze, A. Boldrin, and T. F. Astrup, “Quantification of the resource recovery potential of municipal solid waste incineration bottom ashes,” *Waste Management*, vol. 34, no. 9, pp. 1627–1636, Sep. 2014, doi: 10.1016/J.WASMAN.2014.05.003.

[4] J. Hubert, S. Grigoletto, F. Michel, Z. Zhao, and L. Courard, “Development and Properties of Recycled Biomass Fly Ashes Modified Mortars,” *Recycling 2024, Vol. 9, Page 46*, vol. 9, no. 3, p. 46, May 2024, doi: 10.3390/RECYCLING9030046.

[5] C. Heidrich and J. Feuerborn, “Global opportunities and challenges for coal combustion products with a Circular Economy”.

[6] U. Geological Survey, “Mineral Commodity Summaries 2024,” 2024.

[7] “2023 World Steel in Figures”.

[8] D. Roberts, “Material and Energy Valorisation of Waste in a Circular Economy,” 2022.

[9] “Specification for Slag Cement for Use in Concrete and Mortars,” Dec. 2018, doi: 10.1520/C0989_C0989M-18A.

[10] “Specification for Coal Fly Ash and Raw or Calcined Natural Pozzolan for Use in Concrete,” Aug. 2022, doi: 10.1520/C0618-22.

[11] “Elektrofiltrski pepel-1. del: Definicije, specifikacije in merila skladnosti,” 2012, Accessed: Oct. 21, 2025. [Online]. Available: https://standards.iteh.ai/catalog/standards/sist/1cc224b8-35b6-4f43-a161-

[12] Z. T. Yao *et al.*, “A comprehensive review on the applications of coal fly ash,” *Earth Sci Rev*, vol. 141, pp. 105–121, Feb. 2015, doi: 10.1016/J.EARSCIREV.2014.11.016.

[13] X. Y. Zhuang *et al.*, “Fly ash-based geopolymer: clean production, properties and applications,” *J Clean Prod*, vol. 125, pp. 253–267, Jul. 2016, doi: 10.1016/J.JCLEPRO.2016.03.019.

[14] “Could the end of UK coal inspire a faster global phase-out? | Dialogue Earth.” Accessed: Mar. 05, 2025. [Online]. Available: https://dialogue.earth/en/energy/could-the-end-of-uk-coal-inspire-a-faster-global-phase-out/

[15] “BHP, Rio Tinto to build low-carbon iron pilot plant in Western Australia | Reuters.” Accessed: Mar. 05, 2025. [Online]. Available: https://www.reuters.com/markets/commodities/bhp-rio-tinto-build-low-carbon-iron-pilot-plant-western-australia-2024-12-17/

[16] “Barriers To Net-Zero Concrete – Fly Ash And GGBS Shortage | Concrete4Change.” Accessed: Mar. 05, 2025. [Online]. Available: https://www.concrete4change.com/post/barriers-to-net-zero-concrete-fly-ash-and-ggbs-shortage

[17] M. Ahmaruzzaman, “A review on the utilization of fly ash,” *Prog Energy Combust Sci*, vol. 36, no. 3, pp. 327–363, Jun. 2010, doi: 10.1016/J.PECS.2009.11.003.

[18] D. Suresh and K. Nagaraju, “‘Ground Granulated Blast Slag (GGBS) In Concrete-A Review,’” *IOSR Journal of Mechanical and Civil Engineering (IOSR-JMCE) e-ISSN*, vol. 12, no. 4, pp. 76–82, doi: 10.9790/1684-12467682.

[19] H. El-Hassan and N. Ismail, “Effect of process parameters on the performance of fly ash/GGBS blended geopolymer composites,” *J Sustain Cem Based Mater*, vol. 7, no. 2, pp. 122–140, Mar. 2018, doi: 10.1080/21650373.2017.1411296.

[20] K. K. Jurić, I. Carević, A. Marijana Serdar, N. Štirmer, and M. Serdar, “Feasibility of using pozzolanicity tests to assess reactivity of wood biomass fly ashes,” *Authors: GRAĐEVINAR*, vol. 72, pp. 1145–1153, 2020, doi: 10.14256/JCE.2950.2020.
[21] B. Chen *et al.*, “Reactivity and leaching potential of municipal solid waste incineration (MSWI) bottom ash as supplementary cementitious material and precursor for alkali-activated materials,” *Constr Build Mater*, vol. 409, p. 133890, Dec. 2023, doi: 10.1016/J.CONBUILDMAT.2023.133890.
[22] B. Chen, P. Perumal, M. Illikainen, and G. Ye, “A review on the utilization of municipal solid waste incineration (MSWI) bottom ash as a mineral resource for construction materials,” *Journal of Building Engineering*, vol. 71, p. 106386, Jul. 2023, doi: 10.1016/J.JOBE.2023.106386.
[23] Z. P. Bažant, “Prediction of concrete creep and shrinkage: past, present and future,” *Nuclear Engineering and Design*, vol. 203, no. 1, pp. 27–38, Jan. 2001, doi: 10.1016/S0029-5493(00)00299-5.
[24] O. M. Jensen and F. Hansen, “Autogenous deformation and RH-change in perspective,” *Cem Concr Res*, vol. 31, no. 12, pp. 1859–1865, 2001.
[25] Y. Zhang *et al.*, “Early-Age Cracking of Fly Ash and GGBFS Concrete Due to Shrinkage, Creep, and Thermal Effects: A Review,” *Materials*, vol. 17, no. 10, p. 2288, May 2024, doi: 10.3390/MA17102288.
[26] T. Lu, Z. Li, and H. Huang, “Effect of Supplementary Materials on the Autogenous Shrinkage of Cement Paste,” *Materials*, vol. 13, no. 15, p. 3367, Aug. 2020, doi: 10.3390/MA13153367.
[27] Z. Nasser Eddine, F. Barraj, J. Khatib, and A. Elkordi, “Volume Stability of Pervious Concrete Pavement Containing Municipal Solid Waste Incineration Bottom Ash,” *International Journal of Pavement Research and Technology*, vol. 18, no. 3, pp. 759–772, May 2025, doi: 10.1007/S42947-023-00379-8.
[28] J. Malaiškienė, E. Spudulis, and R. Stonys, “The Effect of Milled Municipal Solid Waste Incineration Bottom Ash on Cement Hydration and Mortar Properties,” *Materials*, vol. 16, no. 6, p. 2528, Mar. 2023, doi: 10.3390/MA16062528.
[29] J. Hubert, S. Grigoletto, F. Michel, Z. Zhao, and L. Courard, “Development and Properties of Recycled Biomass Fly Ashes Modified Mortars,” *Recycling 2024, Vol. 9, Page 46*, vol. 9, no. 3, p. 46, May 2024, doi: 10.3390/RECYCLING9030046.
[30] T. Lu, Z. Li, and H. Huang, “Effect of Supplementary Materials on the Autogenous Shrinkage of Cement Paste,” *Materials*, vol. 13, no. 15, p. 3367, Aug. 2020, doi: 10.3390/MA13153367.
[31] K. K. Jurić, I. Carević, A. Marijana Serdar, N. Štirmer, and M. Serdar, “Feasibility of using pozzolanicity tests to assess reactivity of wood biomass fly ashes,” *Authors: GRAĐEVINAR*, vol. 72, pp. 1145–1153, 2020, doi: 10.14256/JCE.2950.2020.
[32] X. Liang, Z. Li, H. Dong, and G. Ye, “A review on the characteristics of wood biomass fly ash and their influences on the valorization in cementitious materials,” *Journal of Building Engineering*, vol. 97, p. 110927, Nov. 2024, doi: 10.1016/J.JOBE.2024.110927.
[33] A. Tesovnik, L. M. Ottosen, and V. Ducman, “Carbonation of lightweight alkali-activated aggregates based on biomass fly ash: Effect on microstructure and leaching behavior,” *Case Studies in Construction Materials*, vol. 23, p. e05014, Dec. 2025, doi: 10.1016/J.CSCM.2025.E05014.
[34] P. Wattanachai, K. Kochchapong, S. Chaiwithee, T. Keereemasthong, and K. Pimraksa, “Development of non-OPC binder using fly ash, limestone powder, gibbsite powder, and biomass ash for workability, strength, and CO2 capture,” *Sci Rep*, vol. 15, no. 1, pp. 1–11, Dec. 2025, doi: 10.1038/S41598-025-95482-0;SUBJMETA=1023,1025,166,301,4057,4077,639,986;KWRD=CARBON+CAPTURE+AN

D+STORAGE,CIVIL+ENGINEERING,COMPOSITES.
[35] X. Liang, “Valorization of Wood Biomass Fly Ash for the Development of Sustainable Low-carbon Cementitious Materials,” 2024, doi: 10.4233/UUID:B17DDA4D-A804-447C-9278-7B85026DA167.
[36] K. T. Park, J.-S. Ryou, B.-H. Woo, J.-S. Choi, and H. G. Kim, “Quick Hardening Properties of the Cement Paste Partially Replaced by the Calcined-Milled Wood Fly Ash,” *Journal of Materials in Civil Engineering*, vol. 36, no. 10, p. 04024309, Oct. 2024, doi: 10.1061/JMCEE7.MTENG-18014/ASSET/41E4E581-EC1C-4AF6-852E-FF141981F58B/ASSETS/IMAGES/LARGE/FIGURE13.JPG.
[37] M. Xu, K. Takasu, Z. Liu, and H. Suyama, “Study on the modification effect by flotation method of wood biomass fly ash and the applicability to cement-based composites,” *Case Studies in Construction Materials*, vol. 22, p. e04478, Jul. 2025, doi: 10.1016/J.CSCM.2025.E04478.
[38] I. Gabrijel, M. Skazlić, and N. Štirmer, “Long-Term Behavior of Concrete Containing Wood Biomass Fly Ash,” *Applied Sciences 2022, Vol. 12, Page 12859*, vol. 12, no. 24, p. 12859, Dec. 2022, doi: 10.3390/APP122412859.
[39] S. Wang, A. Miller, E. Llamazos, F. Fonseca, and L. Baxter, “Biomass fly ash in concrete: Mixture proportioning and mechanical properties,” *Fuel*, vol. 87, no. 3, pp. 365–371, Mar. 2008, doi: 10.1016/J.FUEL.2007.05.026.
[40] I. Carević, N. Štirmer, M. Trkmić, and K. K. Jurić, “Leaching Characteristics of Wood Biomass Fly Ash Cement Composites,” *Applied Sciences 2020, Vol. 10, Page 8704*, vol. 10, no. 23, p. 8704, Dec. 2020, doi: 10.3390/APP10238704.
[41] D. Marchon and R. J. Flatt, “Mechanisms of cement hydration,” *Science and Technology of Concrete Admixtures*, pp. 129–145, Jan. 2016, doi: 10.1016/B978-0-08-100693-1.00008-4.
[42] J. W. Bullard *et al.*, “Mechanisms of cement hydration,” *Cem Concr Res*, vol. 41, no. 12, pp. 1208–1223, Dec. 2011, doi: 10.1016/J.CEMCONRES.2010.09.011.
[43] H. F. W. Taylor, “Cement chemistry 2nd edition ThomasTelford”.
[44] H. Minard, S. Garrault, L. Regnaud, and A. Nonat, “Mechanisms and parameters controlling the tricalcium aluminate reactivity in the presence of gypsum,” *Cem Concr Res*, vol. 37, no. 10, pp. 1418–1426, Oct. 2007, doi: 10.1016/J.CEMCONRES.2007.06.001.
[45] R. Holly, H. Peemoeller, M. Zhang, E. Reardon, and C. M. Hansson, “Magnetic resonance in situ study of tricalcium aluminate hydration in the presence of gypsum,” *Journal of the American Ceramic Society*, vol. 89, no. 3, pp. 1022–1027, Mar. 2006, doi: 10.1111/J.1551-2916.2005.00770.X;JOURNAL:JOURNAL:15512916;WGROUP:STRING:PUBLICATION.
[46] R. F. Feldman and V. S. Ramachandran, “The influence of CaSO4.2H2O upon the hydration character of 3CaO.Al2O3,” *https://doi.org/10.1680/macr.1966.18.57.185*, vol. 18, no. 57, pp. 185–196, May 2015, doi: 10.1680/MACR.1966.18.57.185.
[47] T. C. Powers and T. L. Brownyard, “Studies of the Physical Properties of Hardened Portland Cement Paste,” *Journal Proceedings*, vol. 43, no. 9, pp. 669–712, Feb. 1947, doi: 10.14359/15304.
[48] D. Gawin, F. Pesavento, and B. A. Schrefler, “Hygro-thermo-chemo-mechanical modelling of concrete at early ages and beyond. Part II: Shrinkage and creep of concrete,” *Int J Numer Methods Eng*, vol. 67, no. 3, pp. 332–363, Jul. 2006, doi: 10.1002/NME.1636;WGROUP:STRING:PUBLICATION.
[49] M. S., “Concrete,” *Prentice Hall, New Jersey*, 1981, Accessed: Oct. 10, 2025. [Online]. Available: https://cir.nii.ac.jp/crid/1570291224970678656
[50] P. Navi and C. Pignat, “Three-dimensional characterization of the pore structure of a simulated cement paste,” *Cem Concr Res*, vol. 29, no. 4, pp. 507–514, Apr. 1999, doi:

10.1016/S0008-8846(98)00199-9.
[51] C. Hua, P. Acker, and A. Ehrlacher, “Analyses and models of the autogenous shrinkage of hardening cement paste: I. Modelling at macroscopic scale,” *Cem Concr Res*, vol. 25, no. 7, pp. 1457–1468, Oct. 1995, doi: 10.1016/0008-8846(95)00140-8.
[52] J. Carette, S. Joseph, Ö. Cizer, and S. Staquet, “Decoupling the autogenous swelling from the self-desiccation deformation in early age concrete with mineral additions: Micro-macro observations and unified modelling,” *Cem Concr Compos*, vol. 85, pp. 122–132, Jan. 2018, doi: 10.1016/J.CEMCONCOMP.2017.10.008.
[53] I. Odler and J. Colán-Subauste, “Investigations on cement expansion associated with ettringite formation,” *Cem Concr Res*, vol. 29, no. 5, pp. 731–735, May 1999, doi: 10.1016/S0008-8846(99)00048-4.
[54] “Scopus - Document Details.” Accessed: Jul. 20, 2025. [Online]. Available: https://www.scopus.com/pages/publications/52649164617?inward=
[55] G. Sant, “Examining time-zero and early age expansion in pastes containing shrinkage reducing admixtures (SRA’ s),” Nov. 2006, doi: 10.1617/2351580028.076.
[56] Y. Wang, Q. Tian, H. Li, Y. Wang, M. Li, and J. Liu, “A new hypothesis for early age expansion of cement-based materials: Cavitation in ink-bottle pores,” *Constr Build Mater*, vol. 326, p. 126884, Apr. 2022, doi: 10.1016/J.CONBUILDMAT.2022.126884.
[57] S. Wu and K. Wan, “The early age expansion in cement pastes with silica fume and SAP induced by crystallization stress,” *Constr Build Mater*, vol. 490, p. 142440, Sep. 2025, doi: 10.1016/J.CONBUILDMAT.2025.142440.
[58] M. Diaferio, F. B. Varona Moya, L. Lavagna, and R. Nisticò, “An Insight into the Chemistry of Cement—A Review,” *Applied Sciences 2023, Vol. 13, Page 203*, vol. 13, no. 1, p. 203, Dec. 2022, doi: 10.3390/APP13010203.
[59] R. M. Espinosa and L. Franke, “Influence of the age and drying process on pore structure and sorption isotherms of hardened cement paste,” *Cem Concr Res*, vol. 36, no. 10, pp. 1969–1984, Oct. 2006, doi: 10.1016/J.CEMCONRES.2006.06.010.
[60] H. Zhao, J. Ding, Y. Huang, Y. Tang, W. Xu, and D. Huang, “Experimental analysis on the relationship between pore structure and capillary water absorption characteristics of cement-based materials,” *Structural Concrete*, vol. 20, no. 5, pp. 1750–1762, Oct. 2019, doi: 10.1002/SUCO.201900184;PAGEGROUP:STRING:PUBLICATION.
[61] Z. P. Bažant and S. Baweja, “Creep and Shrinkage Prediction Model for Analysis and Design of Concrete Structures: Model B3,” pp. 1–83, 2000, Accessed: Aug. 04, 2025. [Online]. Available: www.fsv.cvut.cz/kristek,
[62] H. Ye and A. Radlińska, “Shrinkage mechanisms of alkali-activated slag,” *Cem Concr Res*, vol. 88, pp. 126–135, Oct. 2016, doi: 10.1016/J.CEMCONRES.2016.07.001.
[63] “Autogenous Shrinkage of Concrete,” *Autogenous Shrinkage of Concrete*, Jan. 1999, doi: 10.1201/9781482272123.
[64] T. C. Powers and T. L. Brownyard, “Studies of the Physical Properties of Hardened Portland Cement Paste,” *Journal Proceedings*, vol. 43, no. 9, pp. 669–712, Feb. 1947, doi: 10.14359/15304.
[65] C. F. Ferraris and F. H. Wittmann, “Shrinkage mechanisms of hardened cement paste,” *Cem Concr Res*, vol. 17, no. 3, pp. 453–464, May 1987, doi: 10.1016/0008-8846(87)90009-3.
[66] J. Hagymassy, S. Brunauer, and R. S. Mikhail, “Pore structure analysis by water vapor adsorption: I. t-Curves for water vapor,” *J Colloid Interface Sci*, vol. 29, no. 3, pp. 485–491, Mar. 1969, doi: 10.1016/0021-9797(69)90132-5.
[67] O. M. Jensen and P. F. Hansen, “Autogenous deformation and RH-change in perspective,” *Cem Concr Res*, vol. 31, no. 12, pp. 1859–1865, Dec. 2001, doi: 10.1016/S0008-8846(01)00501-4.

[68] D. Gawin, F. Pesavento, and B. A. Schrefler, “Hygro-thermo-chemo-mechanical modelling of concrete at early ages and beyond. Part II: Shrinkage and creep of concrete,” *Int J Numer Methods Eng*, vol. 67, no. 3, pp. 332–363, Jul. 2006, doi: 10.1002/NME.1636;WGROUP:STRING:PUBLICATION.
[69] O. Coussy, P. Dangla, T. Lassabatère, and V. Baroghel-Bouny, “The equivalent pore pressure and the swelling and shrinkage of cement-based materials,” *Materials and Structures/Materiaux et Constructions*, vol. 37, no. 1, pp. 15–20, 2004, doi: 10.1007/BF02481623/METRICS.
[70] H. M. Jennings, “Refinements to colloid model of C-S-H in cement: CM-II,” *Cem Concr Res*, vol. 38, no. 3, pp. 275–289, Mar. 2008, doi: 10.1016/J.CEMCONRES.2007.10.006.
[71] L. J. Parrott, W. Hansen, and R. L. Berger, “Effect of first drying upon the pore structure of hydrated alite paste,” *Cem Concr Res*, vol. 10, no. 5, pp. 647–655, Sep. 1980, doi: 10.1016/0008-8846(80)90028-9.
[72] I. Maruyama, Y. Nishioka, G. Igarashi, and K. Matsui, “Microstructural and bulk property changes in hardened cement paste during the first drying process,” *Cem Concr Res*, vol. 58, pp. 20–34, Apr. 2014, doi: 10.1016/J.CEMCONRES.2014.01.007.
[73] W. HANSEN, “Drying Shrinkage Mechanisms in Portland Cement Paste,” *Journal of the American Ceramic Society*, vol. 70, no. 5, pp. 323–328, May 1987, doi: 10.1111/J.1151-2916.1987.TB05002.X;SUBPAGE:STRING:ABSTRACT;JOURNAL:JOURNAL:15512916;WGROUP:STRING:PUBLICATION.
[74] Z. P. Bažant, “Prediction of concrete creep and shrinkage: past, present and future,” *Nuclear Engineering and Design*, vol. 203, no. 1, pp. 27–38, Jan. 2001, doi: 10.1016/S0029-5493(00)00299-5.
[75] I. Maruyama, “Origin of Drying Shrinkage of Hardened Cement Paste: Hydration Pressure,” *Journal of Advanced Concrete Technology*, vol. 8, no. 2, pp. 187–200, Jun. 2010, doi: 10.3151/JACT.8.187.
[76] Z. P. Bažant, “Thermodynamics of interacting continua with surfaces and creep analysis of concrete structures,” *Nuclear Engineering and Design*, vol. 20, no. 2, pp. 477–505, Jul. 1972, doi: 10.1016/0029-5493(72)90124-0.
[77] K. Maekawa, T. Ishida, and T. Kishi, “Multi-scale Modeling of Concrete Performance Integrated Material and Structural Mechanics,” *Journal of Advanced Concrete Technology*, vol. 1, no. 2, pp. 91–126, 2003, doi: 10.3151/JACT.1.91.
[78] W. A. Gutteridge and L. J. Parrott, “A study of the changes in weight, length and interplanar spacing induced by drying and rewetting synthetic CSH (I),” *Cem Concr Res*, vol. 6, no. 3, pp. 357–366, May 1976, doi: 10.1016/0008-8846(76)90098-3.
[79] M. Grubor, I. Carević, M. Serdar, N. Š.- polymer, and undefined 2023, “Shrinkage of mortar with the addition of wood biomass ash and recycled tyre polymer fibres,” *researchgate.net*, Accessed: Aug. 14, 2025. [Online]. Available: https://www.researchgate.net/profile/Ivana-Carevic/publication/374373275_Shrinkage_of_mortar_with_the_addition_of_wood_biomass_ash_and_recycled_tyre_polymer_fibres/links/651aa1531e2386049df049cb/Shrinkage-of-mortar-with-the-addition-of-wood-biomass-ash-and-recycled-tyre-polymer-fibres.pdf
[80] Y. Zhang *et al.*, “Early-Age Cracking of Fly Ash and GGBFS Concrete Due to Shrinkage, Creep, and Thermal Effects: A Review,” *Materials*, vol. 17, no. 10, p. 2288, May 2024, doi: 10.3390/MA17102288.
[81] I. Gabrijel, M. Skazlić, and N. Štirmer, “Long-Term Behavior of Concrete Containing Wood Biomass Fly Ash,” *Applied Sciences 2022, Vol. 12, Page 12859*, vol. 12, no. 24, p. 12859, Dec. 2022, doi: 10.3390/APP122412859.
[82] N. Ristić, Z. Grdić, G. Topličić-Ćurčić, D. Grdić, and V. Dodevski, “Properties of Self-

compacting Concrete Produced with Biomass Wood Ash," *Tehnički vjesnik*, vol. 28, pp. 495–502, 2021, doi: 10.17559/TV-20200214103332.
[83] M. Wyrzykowski, S. Ghourchian, S. Sinthupinyo, N. Chitvoranund, T. Chintana, and P. Lura, "Internal curing of high performance mortars with bottom ash," *Cem Concr Compos*, vol. 71, pp. 1–9, Aug. 2016, doi: 10.1016/J.CEMCONCOMP.2016.04.009.
[84] J. Malaiškienė, E. Spudulis, and R. Stonys, "The Effect of Milled Municipal Solid Waste Incineration Bottom Ash on Cement Hydration and Mortar Properties," *Materials*, vol. 16, no. 6, p. 2528, Mar. 2023, doi: 10.3390/MA16062528.
[85] V. Vimonsatit, P. Chindaprasirt, S. Ruangsiriyakul, and V. Sata, "Influence of fly ash fineness on water requirement and shrinkage of blended cement mortars," *KKU Engineering Journal*, vol. 42, no. 4, pp. 311–316, 2015, doi: 10.14456/kkuenj.2015.37.
[86] J. Bawab, J. Khatib, S. Kenai, and M. Sonebi, "A Review on Cementitious Materials Including Municipal Solid Waste Incineration Bottom Ash (MSWI-BA) as Aggregates," *Buildings 2021, Vol. 11, Page 179*, vol. 11, no. 5, p. 179, Apr. 2021, doi: 10.3390/BUILDINGS11050179.
[87] H. Li, H. Chu, Q. Wang, and J. Tang, "Feasibility of producing eco-friendly self-compacting mortar with municipal solid waste incineration bottom ash: A preliminary study," *Case Studies in Construction Materials*, vol. 19, p. e02309, Dec. 2023, doi: 10.1016/J.CSCM.2023.E02309.
[88] C. J. Lynn, G. S. Ghataora, and R. K. Dhir, "Municipal incinerated bottom ash use as a cement component in concrete," *Magazine of Concrete Research*, vol. 69, no. 10, pp. 512–525, May 2017, doi: 10.1680/JMACR.16.00432.
[89] T. AMMAR, "BS EN 196-2 2013." Accessed: Oct. 25, 2025. [Online]. Available: https://www.academia.edu/125736795/BS_EN_196_2_2013
[90] "Particle size analysis. Laser diffraction methods," p. 68, 2020, Accessed: Oct. 25, 2025. [Online]. Available: https://www.en-standard.eu/bs-iso-13320-2020-particle-size-analysis-laser-diffraction-methods/
[91] "Microbeam analysis-Scanning electron microscopy-Guidelines for calibrating image magnification COPYRIGHT PROTECTED DOCUMENT," 2016, Accessed: Oct. 25, 2025. [Online]. Available: www.iso.orgiTehSTANDARDPREVIEW
[92] "Methods of test for mortar for masonry", doi: 10.3403/BSEN1015.
[93] "EN 196-3-2016 ." Accessed: Oct. 25, 2025. [Online]. Available: https://www.doc88.com/p-0478665873048.html
[94] "Products and systems for the protection and repair of concrete structures. Test methods. Determination of modulus of elasticity in compression," Nov. 2006, doi: 10.3403/30149055.
[95] "Methods of testing cement," Jan. 2008, doi: 10.3403/00269357U.
[96] "Test Method for Chemical Shrinkage of Hydraulic Cement Paste," Dec. 2023, doi: 10.1520/C1608-23.
[97] "EN 12617-4:2002 - Products and systems for the protection and repair of concrete structures - Test." Accessed: Oct. 25, 2025. [Online]. Available: https://standards.iteh.ai/catalog/standards/cen/dc994f7b-b2ff-496d-9a3d-b8beede52589/en-12617-4-2002?srsltid=AfmBOor_UMYFy3r3stXdQk5m4CmlFMh-UoFJcPOsoBLNIEhB36C-lJMD&utm_source=chatgpt.com
[98] "ISO 15901-1:2016(en), Evaluation of pore size distribution and porosity of solid materials by mercury porosimetry and gas adsorption — Part 1: Mercury porosimetry." Accessed: Oct. 25, 2025. [Online]. Available: https://www.iso.org/obp/ui/en/#iso:std:iso:15901:-1:ed-2:v1:en
[99] "Practice for Measuring Hydration Kinetics of Hydraulic Cementitious Mixtures Using Isothermal Calorimetry," Dec. 2017, doi: 10.1520/C1679-17.
[100] "Guide for Examination of Hardened Concrete Using Scanning Electron Microscopy,"

Oct. 2022, doi: 10.1520/C1723-16R22.
[101] B. H. Cho, B. H. Nam, J. An, and H. Youn, “Municipal Solid Waste Incineration (MSWI) Ashes as Construction Materials—A Review,” *Materials 2020, Vol. 13, Page 3143*, vol. 13, no. 14, p. 3143, Jul. 2020, doi: 10.3390/MA13143143.
[102] P. Tang, M. V. A. Florea, P. Spiesz, and H. J. H. Brouwers, “Characteristics and application potential of municipal solid waste incineration (MSWI) bottom ashes from two waste-to-energy plants,” 2015, doi: 10.1016/j.conbuildmat.2015.02.033.
[103] J. Hubert, S. Grigoletto, F. Michel, Z. Zhao, and L. Courard, “Development and Properties of Recycled Biomass Fly Ashes Modified Mortars,” *Recycling 2024, Vol. 9, Page 46*, vol. 9, no. 3, p. 46, May 2024, doi: 10.3390/RECYCLING9030046.
[104] “Test Method for Particle Size Distribution of Metal Powders and Related Compounds by Light Scattering,” Oct. 2020, doi: 10.1520/B0822-20.
[105] S. R. Rajagopalan, B. Y. Lee, and S. T. Kang, “Prediction of the Rheological Properties of Fresh Cementitious Suspensions Considering Microstructural Parameters,” *Materials*, vol. 15, no. 20, p. 7044, Oct. 2022, doi: 10.3390/MA15207044.
[106] Y. Sun, B. Chen, S. Zhang, K. Blom, M. Luković, and G. Ye, “Characterization, pre-treatment, and potential applications of fine MSWI bottom ash as a supplementary cementitious material,” *Constr Build Mater*, vol. 421, p. 135769, Mar. 2024, doi: 10.1016/J.CONBUILDMAT.2024.135769.
[107] G. Huang *et al.*, “Use of pretreatment to prevent expansion and foaming in high-performance MSWI bottom ash alkali-activated mortars,” *Constr Build Mater*, vol. 245, p. 118471, Jun. 2020, doi: 10.1016/J.CONBUILDMAT.2020.118471.
[108] A. Maldonado-Alameda *et al.*, “Environmental potential assessment of MSWI bottom ash-based alkali-activated binders,” *J Hazard Mater*, vol. 416, p. 125828, Aug. 2021, doi: 10.1016/J.JHAZMAT.2021.125828.
[109] F. G. Simon and P. Scholz, “Assessment of the Long-Term Leaching Behavior of Incineration Bottom Ash: A Study of Two Waste Incinerators in Germany,” *Applied Sciences (Switzerland)*, vol. 13, no. 24, p. 13228, Dec. 2023, doi: 10.3390/APP132413228/S1.
[110] “EN 206:2013+A2:2021 - Concrete - Specification, performance, production and conformity.” Accessed: Oct. 21, 2025. [Online]. Available: https://standards.iteh.ai/catalog/standards/cen/4f3d2008-978a-47ec-bc12-5660aa40e04d/en-206-2013a2-2021?srsltid=AfmBOor4-KbaWL-wf8oXCP4vTSZRlY4lb2A0G62rytRIQ89JTRfdo5vP&utm_source=chatgpt.com
[111] “EN 450-1:2012 - Fly ash for concrete - Part 1: Definition, specifications and conformity criteria.” Accessed: Oct. 21, 2025. [Online]. Available: https://standards.iteh.ai/catalog/standards/cen/cc9c0d2c-6d67-4290-82ea-e5e99eb8abf0/en-450-1-2012?srsltid=AfmBOoqLiqZ376VuBlXzUXUM1F8OMwFGdTTw0Oz-3wrR8aIdwVHk2ANQ&utm_source=chatgpt.com
[112] P. C. Aïtcin, “High-Performance Concrete,” *High-Performance Concrete*, pp. 1–591, Jan. 2011, doi: 10.4324/9780203475034/HIGH-PERFORMANCE-CONCRETE-PIERRE-CLAUDE-A.
[113] P. K. Mehta and P. J. M. Monteiro, “CONCRETE Microstructure, Properties, and Materials,” *Concrete: Microstructure, Properties, and Materials*, pp. 10–14, 2006, Accessed: Oct. 21, 2025. [Online]. Available: https://repositori.mypolycc.edu.my/jspui/handle/123456789/4614
[114] “Control of Cracking in Concrete Structures,” 2001.
[115] P. Lura, O. M. Jensen, and K. Van Breugel, “Autogenous shrinkage in high-performance cement paste: An evaluation of basic mechanisms,” *Cem Concr Res*, vol. 33, no. 2, pp. 223–232, Feb. 2003, doi: 10.1016/S0008-8846(02)00890-6.

[116] “Test Method for Length Change of Hardened Hydraulic-Cement Mortar and Concrete,” Jul. 2024, doi: 10.1520/C0157_C0157M-24E01.
[117] “EN 196-3:2016 - Methods of testing cement - Part 3: Determination of setting times and soundness.” Accessed: Oct. 21, 2025. [Online]. Available: https://standards.iteh.ai/catalog/standards/cen/e4921eca-8101-4261-b066-25d19b9b8e8a/en-196-3-2016?srsltid=AfmBOoqSFTH4UlOzEIjHLDJ_DYkLtU8tEnJoOEgL8JgPT1NelbpszPU6&utm_source=chatgpt.com
[118] “EN 1015-3:1999 - Methods of test for mortar for masonry - Part 3: Determination of consistence of.” Accessed: Oct. 21, 2025. [Online]. Available: https://standards.iteh.ai/catalog/standards/cen/f427f20a-2746-4ab7-bd55-d1c455b1f009/en-1015-3-1999?srsltid=AfmBOoqLuDGvRxJjJjdnMYWl-QNFqcOZdEJSaQpMuIXLDu6xuAnCl83I&utm_source=chatgpt.com
[119] “Test Method for Autogenous Strain of Cement Paste and Mortar,” Oct. 2019, doi: 10.1520/C1698-19.
[120] “Test Method for Measurement of Heat of Hydration of Hydraulic Cementitious Materials Using Isothermal Conduction Calorimetry,” Feb. 2017, doi: 10.1520/C1702-17.
[121] “Test Method for Determination of the Proportion of Phases in Portland Cement and Portland-Cement Clinker Using X-Ray Powder Diffraction Analysis,” Mar. 2018, doi: 10.1520/C1365-18.
[122] “Test Method for Static Modulus of Elasticity and Poissons Ratio of Concrete in Compression,” Apr. 2022, doi: 10.1520/C0469_C0469M-22.
[123] “Test Method for Determination of Pore Volume and Pore Volume Distribution of Soil and Rock by Mercury Intrusion Porosimetry,” Feb. 2018, doi: 10.1520/D4404-18.
[124] “Test Method for Length Change of Hardened Hydraulic-Cement Mortar and Concrete,” Aug. 2017, doi: 10.1520/C0157_C0157M-17.
[125] R. Rajamma *et al.*, “Biomass fly ash effect on fresh and hardened state properties of cement based materials,” *Compos B Eng*, vol. 77, pp. 1–9, Aug. 2015, doi: 10.1016/J.COMPOSITESB.2015.03.019.
[126] J. Bawab, J. Khatib, S. Kenai, and M. Sonebi, “A Review on Cementitious Materials Including Municipal Solid Waste Incineration Bottom Ash (MSWI-BA) as Aggregates,” *Buildings 2021, Vol. 11, Page 179*, vol. 11, no. 5, p. 179, Apr. 2021, doi: 10.3390/BUILDINGS11050179.
[127] M. Thomas, “Supplementary cementing materials in concrete,” *Supplementary Cementing Materials in Concrete*, pp. 1–181, Jan. 2013, doi: 10.1201/B14493/SUPPLEMENTARY-CEMENTING-MATERIALS-CONCRETE-MICHAEL-THOMAS/RIGHTS-AND-PERMISSIONS.
[128] S. Mindess, F. J. Young, and D. Darwin, “Concrete / S. Mindess, J.F. Young, D. Darwin,” *Hoboken: Prentice Hall. 2nd ed.*, p. 644, 2003, Accessed: Oct. 24, 2025. [Online]. Available: https://books.google.com/books/about/Concrete.html?hl=zh-CN&id=38VoQgAACAAJ
[129] H. M. Jennings, “A model for the microstructure of calcium silicate hydrate in cement paste,” *Cem Concr Res*, vol. 30, no. 1, pp. 101–116, Dec. 1999, doi: 10.1016/S0008-8846(99)00209-4.
[130] D. P. Bentz and O. M. Jensen, “Mitigation Strategies for Autogenous Shrinkage Cracking,” 2004. Accessed: Oct. 24, 2025. [Online]. Available: https://www.nist.gov/publications/mitigation-strategies-autogenous-shrinkage-cracking-0
[131] H. M. Jennings, “A model for the microstructure of calcium silicate hydrate in cement paste,” *Cem Concr Res*, vol. 30, no. 1, pp. 101–116, Dec. 1999, doi: 10.1016/S0008-

8846(99)00209-4.
[132] S. Wang and L. Baxter, “Comprehensive study of biomass fly ash in concrete: Strength, microscopy, kinetics and durability,” *Fuel Processing Technology*, vol. 88, no. 11–12, pp. 1165–1170, Dec. 2007, doi: 10.1016/J.FUPROC.2007.06.016.
[133] de Lima Junior *et al.*, “Reactivity and leaching potential of municipal solid waste incineration (MSWI) bottom ash as supplementary cementitious material and precursor for alkali-activated materials,” 2023, doi: 10.1016/j.conbuildmat.2023.133890.
[134] I. Gabrijel, M. Skazlić, and N. Štirmer, “Long-Term Behavior of Concrete Containing Wood Biomass Fly Ash,” *Applied Sciences 2022, Vol. 12, Page 12859*, vol. 12, no. 24, p. 12859, Dec. 2022, doi: 10.3390/APP122412859.
[135] “(PDF) Early Age Autogenouts Shrinkage of Concrete.” Accessed: Oct. 25, 2025. [Online]. Available: https://www.researchgate.net/publication/33520608_Early_Age_Autogenouts_Shrinkage_of_Concrete
[136] J. J. Beaudoin, H. Dramé, L. Raki, and R. Alizadeh, “Formation and properties of C-S-H-PEG nano-structures,” *Materials and Structures/Materiaux et Constructions*, vol. 42, no. 7, pp. 1003–1014, Aug. 2009, doi: 10.1617/S11527-008-9439-X.
[137] G. Sant, B. Lothenbach, P. Juilland, G. Le Saout, J. Weiss, and K. Scrivener, “The origin of early age expansions induced in cementitious materials containing shrinkage reducing admixtures,” *Cem Concr Res*, vol. 41, no. 3, pp. 218–229, Mar. 2011, doi: 10.1016/J.CEMCONRES.2010.12.004.
[138] “The Study of Cement Hydration by Isothermal Calorimetry”, Accessed: Oct. 25, 2025. [Online]. Available: http://www.tainstruments.com/
[139] W. Nocuń-Wczelik, A. Stok, and Z. Konik, “Heat evolution in hydrating expansive cement systems,” *J Therm Anal Calorim*, vol. 101, no. 2, pp. 527–532, May 2010, doi: 10.1007/S10973-010-0846-1.
[140] M. Sanytsky, T. Kropyvnytska, and O. Shyiko, “EFFECT OF POTASSIUM SULFATE ON THE PORTLAND CEMENT PASTES SETTING BEHAVIOR,” *CHEMISTRY & CHEMICAL TECHNOLOGY Chem. Chem. Technol*, vol. 17, no. 1, pp. 170–178, 2023, doi: 10.23939/chcht17.01.170.
[141] M. Sanytsky, T. Kropyvnytska, and O. Shyiko, “EFFECT OF POTASSIUM SULFATE ON THE PORTLAND CEMENT PASTES SETTING BEHAVIOR,” *CHEMISTRY & CHEMICAL TECHNOLOGY Chem. Chem. Technol*, vol. 17, no. 1, pp. 170–178, 2023, doi: 10.23939/chcht17.01.170.
[142] C. Qiao, P. Suraneni, and J. Weiss, “Damage in cement pastes exposed to NaCl solutions,” *Constr Build Mater*, vol. 171, pp. 120–127, May 2018, doi: 10.1016/J.CONBUILDMAT.2018.03.123.
[143] Y. Cai, Y. Tao, D. Xuan, X. Zhu, and C. S. Poon, “Effects of seawater on the formation and mechanical properties of Friedel’s salt associated with tricalcium aluminate,” *Cem Concr Res*, vol. 174, p. 107340, Dec. 2023, doi: 10.1016/J.CEMCONRES.2023.107340.
[144] U. A. Birnin-Yauri and F. P. Glasser, “Friedel’s salt, Ca2Al(OH)6(Cl,OH)·2H2O: its solid solutions and their role in chloride binding,” *Cem Concr Res*, vol. 28, no. 12, pp. 1713–1723, Dec. 1998, doi: 10.1016/S0008-8846(98)00162-8.
[145] A. K. Suryavanshi, J. D. Scantlebury, and S. B. Lyon, “Mechanism of Friedel’s salt formation in cements rich in tri-calcium aluminate,” *Cem Concr Res*, vol. 26, no. 5, pp. 717–727, May 1996, doi: 10.1016/S0008-8846(96)85009-5.
[146] S. Smillie, E. Moulin, D. E. Macphee, F. P. Glasser, and J. Bensted, “Freshness of cement: conditions for syngenite CaK 2 (S04)2. H 2 0 formation,” *Advances in Cement Research*, vol. 6, no. 23, pp. 93–96, 1994, Accessed: Oct. 25, 2025. [Online]. Available:

http://www.emerald.com/jadcr/article-pdf/6/23/135/2432685/adcr_1994_6_23_135.pdf
[147] P. K. Mehta, “Mechanism of expansion associated with ettringite formation,” *Cem Concr Res*, vol. 3, no. 1, pp. 1–6, Jan. 1973, doi: 10.1016/0008-8846(73)90056-2.
[148] Lu, “Autogenous shrinkage of early age cement paste and mortar,” 2019, doi: 10.4233/uuid:e06bd615-7fc4-481b-a334-37627f142e3d.
[149] “Chapter 3 DRYING SHRINKAGE AND CREEP IN CONCRETE: A SUMMARY”.
[150] M. K. Mohan, A. V Rahul, J. F. Van Stappen, V. Cnudde, G. De Schutter, and K. Van Tittelboom, “Assessment of pore structure characteristics and tortuosity of 3D printed concrete using mercury intrusion porosimetry and X-ray tomography,” 2023, doi: 10.1016/j.cemconcomp.2023.105104.
[151] A. Cuesta, A. Morales-Cantero, A. G. De la Torre, and M. A. G. Aranda, “Recent Advances in C-S-H Nucleation Seeding for Improving Cement Performances,” *Materials*, vol. 16, no. 4, p. 1462, Feb. 2023, doi: 10.3390/MA16041462.
[152] D. Wang, C. Shi, N. Farzadnia, Z. Shi, H. Jia, and Z. Ou, “A review on use of limestone powder in cement-based materials: Mechanism, hydration and microstructures,” *Constr Build Mater*, vol. 181, pp. 659–672, Aug. 2018, doi: 10.1016/J.CONBUILDMAT.2018.06.075.
[153] A. M. Joseph, R. Snellings, P. Van den Heede, S. Matthys, and N. De Belie, “The Use of Municipal Solid Waste Incineration Ash in Various Building Materials: A Belgian Point of View,” *Materials*, vol. 11, no. 1, p. 141, Jan. 2018, doi: 10.3390/MA11010141.
[154] H. Kinoshita *et al.*, “Corrosion of aluminium metal in OPC- and CAC-based cement matrices,” *Cem Concr Res*, vol. 50, pp. 11–18, Aug. 2013, doi: 10.1016/J.CEMCONRES.2013.03.016.
[155] L. Zhang, X. Qian, T. Lin, S. Ruan, D. Yan, and K. Qian, “Is early drying shrinkage still determined by the mesopore content? A case study of cement paste with minerals,” *Journal of Building Engineering*, vol. 50, p. 104187, Jun. 2022, doi: 10.1016/J.JOBE.2022.104187.
[156] W. Zhang, X. Duan, F. Su, J. Zhu, and Y. Hama, “Drying shrinkage inhibition effect and mechanism of polyol shrinkagex reducing admixture on the metakaolin-based geopolymer,” *Journal of Materials Research and Technology*, vol. 28, pp. 2021–2032, Jan. 2024, doi: 10.1016/J.JMRT.2023.12.094.
[157] J. L. Poole, K. A. Riding, K. J. Folliard, M. C. G. Juenger, and A. K. Schindler, “Methods for Calculating Activation Energy for Portland Cement,” *ACI Mater J*, vol. 104, no. 1.
[158] R. H. Bogue, “Calculation of the Compounds in Portland Cement,” *Industrial and Engineering Chemistry - Analytical Edition*, vol. 1, no. 4, pp. 192–197, Oct. 2002, doi: 10.1021/AC50068A006.
[159] “Standard Test Methods for Measuring the Reactivity of Supplementary Cementitious Materials by Isothermal Calorimetry and Bound Water Measurements,” Jun. 2020, doi: 10.1520/C1897-20.
[160] S. Blotevogel *et al.*, “Ability of the R3 test to evaluate differences in early age reactivity of 16 industrial ground granulated blast furnace slags (GGBS),” *Cem Concr Res*, vol. 130, p. 105998, Apr. 2020, doi: 10.1016/J.CEMCONRES.2020.105998.
[161] P. de Azevedo Basto, V. Estolano de Lima, and A. de Melo Neto, “Capability of R3 test to evaluate pozzolanicity of ground raw and calcined sugarcane bagasse ashes,” *Mater Today Proc*, Apr. 2023, doi: 10.1016/J.MATPR.2023.04.048.
[162] W. Lerch and R. H. Bogue, “HEAT OF HYDRATION OF PORTLAND CEMENT PASTES,” *Part of Bureau of Standards Journal of Research*, vol. 12, 1934.
[163] B. Yang, Y. Liu, and X. Y. Wang, “A Hydration Model to Evaluate the Properties of Cement–Quartz Powder Hybrid Concrete,” *Materials*, vol. 17, no. 11, p. 2769, Jun. 2024, doi: 10.3390/MA17112769/S1.

[164] “Cement and Concrete Chemistry”, doi: 10.1007/978-94-007-7945-7.
[165] “Reactivity tests for supplementary cementitious materials: RILEM TC 267-TRM phase 1”, doi: 10.1617/s11527-018-1269-x.
[166] M. Zajac, P. Durdzinski, C. Stabler, J. Skocek, D. Nied, and M. Ben Haha, “Influence of calcium and magnesium carbonates on hydration kinetics, hydrate assemblage and microstructural development of metakaolin containing composite cements,” *Cem Concr Res*, vol. 106, pp. 91–102, Apr. 2018, doi: 10.1016/J.CEMCONRES.2018.01.008.
[167] J. Skibsted and R. Snellings, “Reactivity of supplementary cementitious materials (SCMs) in cement blends,” *Cem Concr Res*, vol. 124, p. 105799, Oct. 2019, doi: 10.1016/J.CEMCONRES.2019.105799.
[168] Z. Pan and C. Y. Zhao, “Dehydration/hydration of MgO/H2O chemical thermal storage system,” *Energy*, vol. 82, pp. 611–618, Mar. 2015, doi: 10.1016/J.ENERGY.2015.01.070.
[169] Y. A. Criado, M. Alonso, and J. C. Abanades, “Kinetics of the CaO/Ca(OH)2 hydration/dehydration reaction for thermochemical energy storage applications,” *Ind Eng Chem Res*, vol. 53, no. 32, pp. 12594–12601, Aug. 2014, doi: 10.1021/IE404246P.
[170] M. I. Malek, C. C. Wu, S. D. Walck, and M. L. Pantoya, “Hydration of alumina (Al2O3) toward advancing aluminum particles for energy generation applications,” *Colloids Surf A Physicochem Eng Asp*, vol. 652, p. 129740, Nov. 2022, doi: 10.1016/J.COLSURFA.2022.129740.